CALIFORNIA STATE POLYTECHNIC UNIVERSITY, POMONA
THESIS ELECTRONIC SIGNATURE PAGE

Submitted: Term Spring Year 2021

Bronco ID: 012187162

Email Address: aalkaabi@cpp.edu

THESIS INFORMATION

THESIS TITLE NEW GEOCHRONOLOGY AND STRATIGRAPHIC INTERPRETATIONS OF THE MID-TERTIARY SOLEDAD

AUTHOR Abdulla Al-Kaabi

PROGRAM Geology, M.S.

SIGNATURES

Bryan P Murray
Committee Chair Name

Thesis Committee Chair
Position

Geological Sciences Department
Department

Organization

DocuSigned by:
20873EBAB5874F6...
Signature

5/26/2021

bpmurray@cpp.edu
Email

Jonathan A. Nourse
Committee Member 2 Name

Chair & Professor
Position

Geological Sciences Department
Department

Organization

DocuSigned by: Jonathan A. Nourse
562E96F6E80E44B...
Signature

5/26/2021

janourse@cpp.edu
Email

Nicholas J Van Buer
Committee Member 3 Name

Assistant Professor
Position

Geological Sciences Department
Department

Organization

DocuSigned by:
ED2E989A7B2A47B...
Signature

5/26/2021

njvanbuer@cpp.edu
Email

Upload Thesis Attachment:

Revised August 2020,
Graduate Studies Office

NEW GEOCHRONOLOGY AND STRATIGRAPHIC INTERPRETATIONS OF THE MID-TERTIARY SOLEDAD ROJO FORMATION IN THE LOWER COLORADO RIVER EXTENSIONAL CORRIDOR, WESTERN PALO VERDE MOUNTAINS, SE CALIFORNIA

A Thesis

Presented to the

Faculty of

California State Polytechnic University, Pomona

In Partial Fulfillment

Of the Requirements for the Degree

Master of Science

In

Geological Sciences

By

Abdulla Al-Kaabi

2021

SIGNATURE PAGE

THESIS: NEW GEOCHRONOLOGY AND STRATIGRAPHIC INTERPRETATIONS OF THE MID-TERTIARY SOLEDAD ROJO FORMATION IN THE LOWER COLORADO RIVER EXTENSIONAL CORRIDOR, WESTERN PALO VERDE MOUNTAINS, SE CALIFORNIA

AUTHOR: Abdulla M. Al-Kaabi

DATE SUBMITTED: Spring 2021

Department of Geological Sciences

Dr. Bryan Murray
Thesis Committee Chair
Geological Sciences
____

Dr. Jonathan Nourse
Geological Sciences
____

Dr. Nicholas Van Buer
Geological Sciences
____

ACKNOWLEDGEMENTS

The help of those who were right by my side was invaluable to the thesis project completion. Therefore, I would like to take this opportunity and devote this section for these people who gave me all the support I needed especially during my hard times recently.

I would like to start with my sponsor. This study was made possible by grant QRLP9-G-4440053 from Qatar National Research Fund (a member of Qatar Foundation). They were always supported and helped however they could.

Thank you to my advisor, Dr. Bryan Murray, for all the knowledge and experience I got from you in sedimentology. Your patience and guidance helped boosting my research skills and interests in geology. Thank you for always being there whenever I had a question, or I am stuck and unable to proceed with my project. I would never make it without you.

Thank you to all the Geological Sciences department of Cal Poly Pomona faculty and staff. I would like here to mention Dr. Jonathan Nourse for accepting me into the program and being my advisor for my first few terms and thank you again to act as a co-advisor in this project. I would like also to thank Dr. Nicholas Van Buer for his outstanding teaching methods and dedication. You have inspired me more to be an instructor just like you in the future.

Thank you to my family for always being there for me. Thank you, mother, for always encouraging me to do my best as well as believing in me. You are the most supportive person I know. Thank you to my father, for giving me the opportunity to continue my studies and by greatly helping me whenever I needed help. Thank you, my brothers and sisters for believing in me.

Finally, I would like to thank my best friends Mohammed Aljassim, Mohammed Alajmi, Abdulla Aljamani, Abdulaziz Alsumaiti, and Mohammed Alkaabi for all the support I got from you. Thank you for always pushing me to exceed my limits sometimes and to go above and beyond in every aspect of my life.

Thank you All!

ABSTRACT

This study presents new detrital zircon geochronology and stratigraphic interpretations from the Soledad Rojo formation, an informally named moderately east-dipping section of previously undated red beds located in the Lower Colorado River Extensional Corridor of southeast California. Stratigraphic relationships suggest that the Soledad Rojo formation represents an alluvial fan/braided fluvial system deposited in a syndepositional half-graben basin that developed during regional mid-Tertiary extension in the southern Basin and Range province. This basin is bounded on the east by an inferred north-trending normal fault that uplifts mid-late Oligocene volcanic rocks of the Palo Verde Mountains in the footwall. To the west, the Soledad Rojo formation is deposited conformably above the Tuff of Black Hills (22-27 Ma), which extends further outside of the research area.

This study subdivides the Soledad Rojo formation into three stratigraphic subunits: 1) a lower alluvial unit (Tsrl), consisting primarily of trough cross-bedded, brick red coarse-grained lithic arkose interbedded with subangular-subrounded cobble conglomerate; 2) a middle fluvial unit (Tsrm) of clast-supported, rounded-subrounded cobble-boulder conglomerate interbedded with brick red lithic arkose similar to lower unit; and 3) an upper alluvial unit (Tsru) of interbedded light gray to buff conglomeratic lithic arkose and subangular-subrounded pebble-cobble conglomerate. Silicic and mafic volcanic rocks (Tbh, Tsrv) underlie and are intercalated with the Soledad Rojo formation red beds, and a younger dacitic intrusion (Td) with an age around 20.5 Ma that crosscuts the basin deposits in the northern part of the study area. Detrital zircon geochronology suggests that the maximum depositional age of the Soledad Rojo formation is ca. 24.5 Ma, and the

sediments were derived from late Cretaceous (ca. 75 Ma), late Jurassic (ca. 153 Ma.), and Proterozoic (ca. 1.2 and 1.7 Ga) sources, potentially from late Mesozoic to Proterozoic metaplutonic basement rocks exposed in the region adjacent to the basin.

TABLE OF CONTENTS

List of Tables

List of Figures

CHAPTER 1- INTRODUCTION

The western Palo Verde Mountains, the research area that is the focus of this study, is located in the Colorado Desert of southeastern California within the southern Basin and Range province (Figure 1). The purpose of this study is to examine the Soledad Rojo formation, an undated sequence of red beds found on the western side of the northern Palo Verde Mountains marked by the black box (Figure 2), to develop a better understanding of the history of Basin and Range extensional deformation in this research area. Previous workers hypothesized that the Soledad Rojo formation was either derived from the ancestral Colorado River or was a continuation of the Tolbard Fanglomerate found in the Midway Mountains to the south of the study area (Figure 2). In order to fully understand the nature and the geology of the research area, several questions had to be answered: (1) what are the sedimentary facies and basin structure found within the study area?; (2) what is the provenance of the Soledad Rojo formation?; (3) what is the age of the Soledad Rojo formation?; and (4) what is the validity of previous interpretations and correlations between the Soledad Rojo formation and any other formations? To address these questions, this study presents new geologic mapping, stratigraphic column measurements, detrital zircon dating, and thin section modal point-counting analyses to show that the Soledad Rojo formation was deposited in a late Oligocene to early Miocene-age (ca. 23 Ma) alluvial fan/braided fluvial system likely derived from nearby Mesozoic-Proterozoic metaplutonic basement and Tertiary volcanic sources.

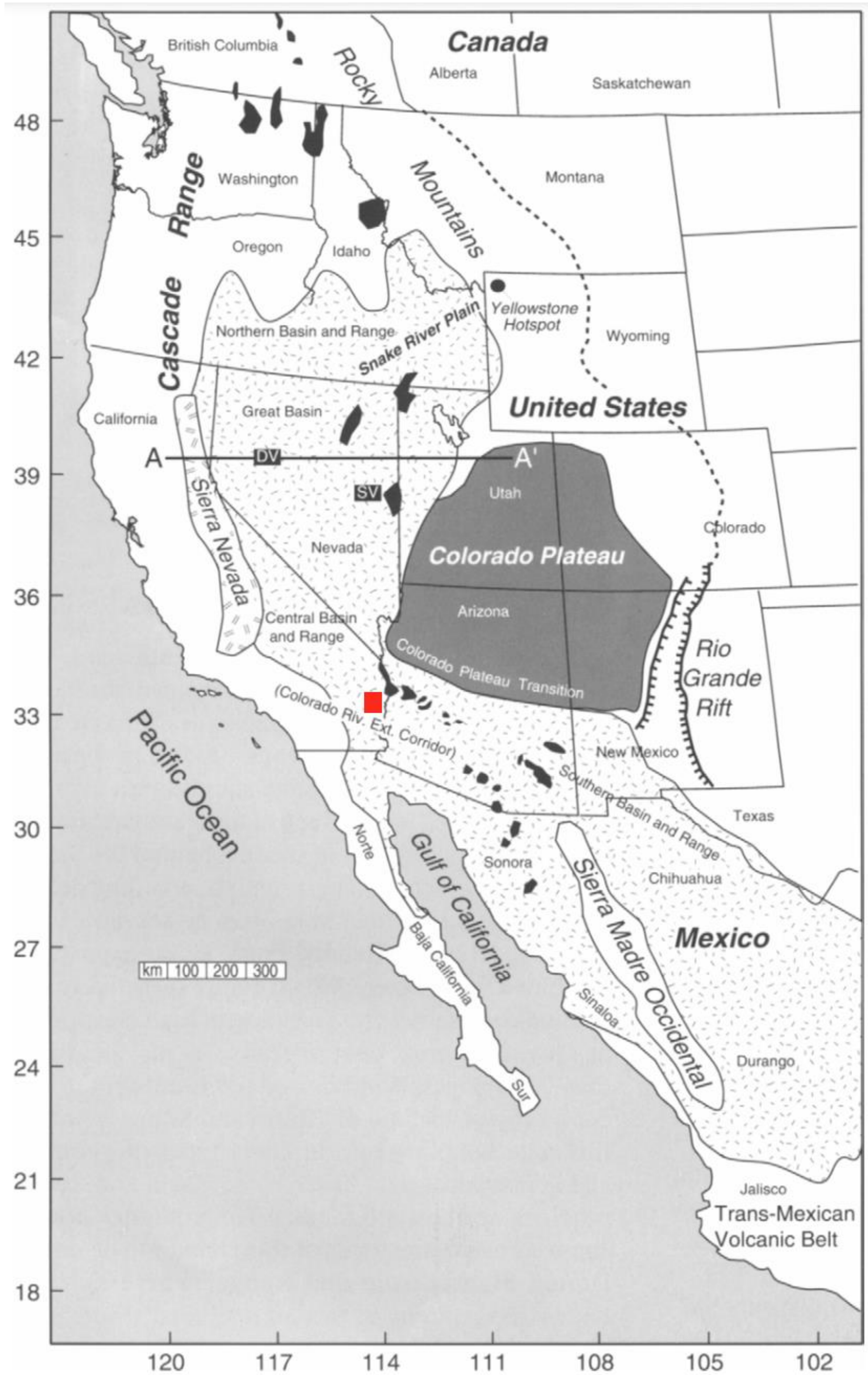

Figure 1: Map and location of the Basin and Range Province (stippled pattern), extending from northern Mexico to the northwestern part of USA. Red box represents the approximate location of the research area (Figure 2). Black areas represent the location of metamorphic core complexes. Dashed line represents the inferred eastern boundary of the Laramide thrust faults (from Parsons, 2006).

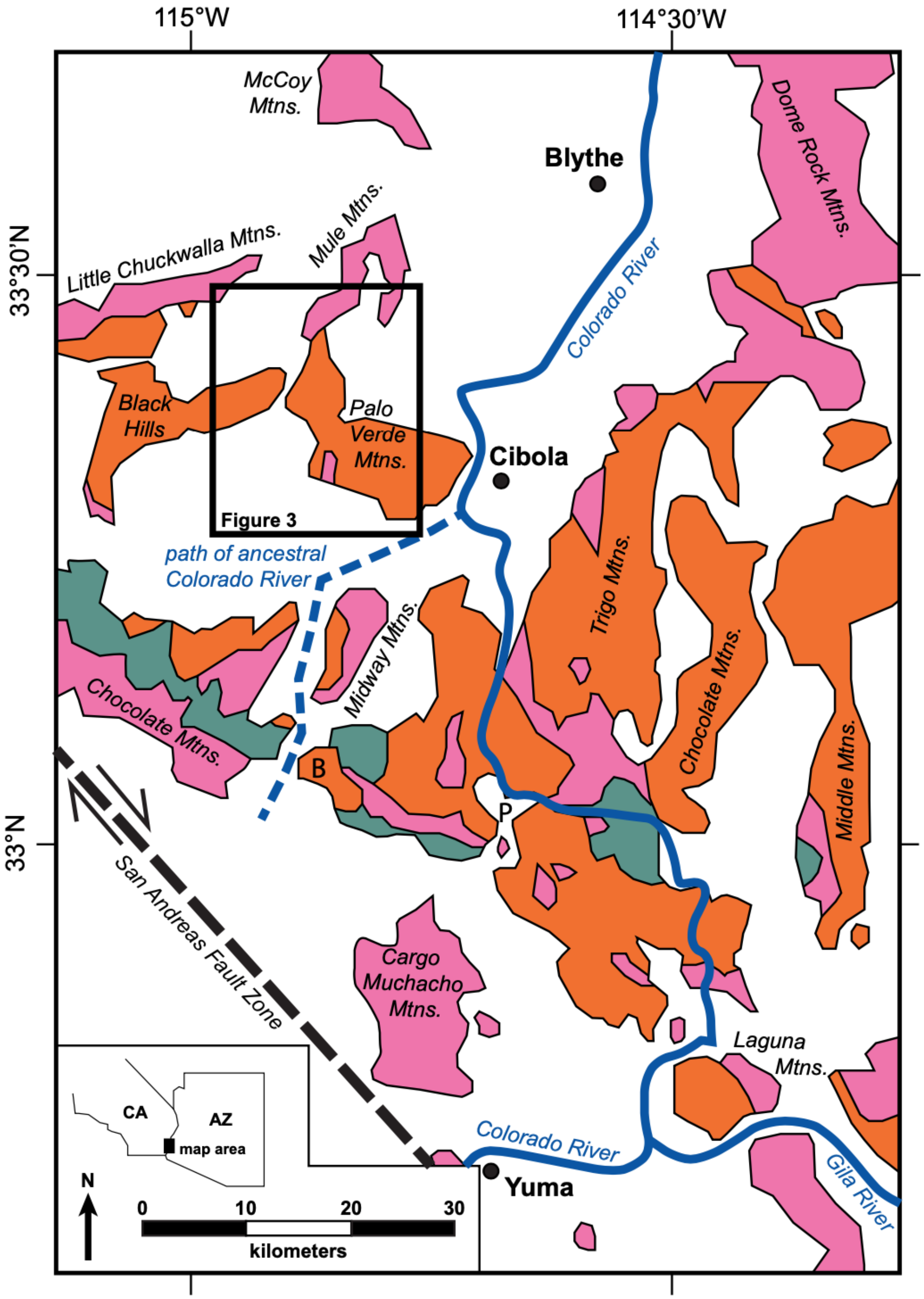

Holocene - late Miocene sedimentary deposits

Oligo-Miocene (ca. 32-18 Ma) volcanic & sedimentary deposits - includes minor Tertiary granites

Orocopia schist (Mesozoic) - includes Mesozoic & Tertiary granitic rocks in western Chocolate Mtns.

Metaigneous & metasedimentary rocks (Mesozoic-Proterozoic)

Figure 2 (previous page): Regional geologic map of southeastern California & southwestern Arizona, showing the distribution of early Neogene volcanic and sedimentary deposits (orange) and potential basement sediment source rocks, including Precambrian-Mesozoic metaigneous and metasedimentary rocks (pink) and the Orocopia schist (green). B and P stands for the locations of Black Mountain and Picacho State Park, respectively. The proposed path of the ancestral Colorado River is indicated by blue dashed line south of the Palo Verde Mountains (Modified from Sherrod and Tosdal, 1991). The location of the study area is indicated by the black box (Figure 3); the Tolbard Fanglomerate, which is tentatively correlated to the Soledad Rojo formation, outcrops in the Midway mountains approximately 13 km to the south.

1.1 GEOLOGIC SETTING

The Basin and Range province is a region of highly extended, arid topography found within the western Cordillera in North America. It lies over much of the western United States, extending from southern Oregon-Idaho in the north to most of northern Mexico south to the Trans-Mexican Volcanic Belt (Figure 1). In the north, the Basin and Range covers most of the area between the Rocky Mountains and the Cascade Ranges. In the middle, it is bounded by the Colorado Plateau on the east and the Sierra Nevada batholith to the west. In the south, it surrounds northern Mexico's Sierra Madre Occidental Range. The Basin and Range terrain is dominated by parallel mountain ranges that are regularly spaced with extensional hanging wall basins between them (Eaton 1982, Parsons 2006). The extensional structure of the Basin and Range is the result of a long history of tectonic activity that influenced the different areas of the western Cordillera (e.g., Conde, 1982), including numerous cycles of deformation—particularly extension, compression, and transform—that resulted in the formation of the province.

1.1.1 TECTONICS OF THE SOUTHERN BASIN AND RANGE PROVINCE

Various forms of crustal deformation occurred during the Cenozoic Era in western North America that significantly defined the geologic development of the southern Basin and Range province in the vicinity of the study area, including transform deformation in the western continental margin from the mid-Cenozoic to Quaternary period, which followed a period of widespread crustal extension in the Basin and Range province that involved the development of metamorphic core complexes in highly extended areas and high-angle normal block faulting in less extended regions (e.g., Wernicke,1992; Axen et al., 1993; Parsons, 2006). During the mid- to late-Cenozoic, east-northeast-directed crustal extension occurred in most areas of central and northern Mexico and the southwestern United States, with the region of extension found west of the extent of Laramide deformation (Figure 1; Parsons 2006) The east-northeast-directed extension in the southern Basin and Range is estimated to have started around 30 million years ago (Parsons, 2006). The age of initial extension in the southern Basin and Range province exhibits a southeast to northwest migratory trend of younger deformational ages, with early stages of extension occurring during the late Oligocene in the southern regions of Arizona, California, and Mexico's Chihuahua, Oaxaca, and Durango. Large-scale crustal extension happened in different regions of northern Mexico and southwestern United States during the early Miocene, culminating in the formation of metamorphic core complexes at the southern margins of Colorado Plateau and the area along the Colorado River located between Arizona and California. (Figure 1; Henry and Aranda-Gomez, 1992; Parsons, 2006).

1.1.2 VOLCANISM IN THE SOUTHERN BASIN AND RANGE REGION

Western North America has had a lengthy history of magmatism since the mid-Mesozoic era. Plutonic and volcanic activity heightened during the Cretaceous period due to subduction of the Farallon plate beneath North America, resulting in the formation of a chain of batholiths extending from British Columbia to northwestern Mexico (e.g., Hildebrand and Whalen, 2017 and references therein). During the late Cretaceous to Eocene, flat-slab subduction resulted in the shutoff of arc-magmatism in the western United States (Laramide magmatic gap), coupled with an eastward migration of subduction-related volcanism in northern Mexico and southern Arizona, south of the Laramide magmatic gap (Ferrari et al., 2007 and references therein). The Laramide magmatic gap continued until ca. 40 Ma, when removal of the Farallon plate from the base of the North American plate resulted in a westward sweep of magmatism in the southwestern United States and northern Mexico (Ferrari et al., 2007 and references therein). Basaltic and bimodal volcanism prevailed in this region and was often accompanied by core complex extension, with the relative timing of these events occurring in the Colorado River region during the late Oligocene to early Miocene (Parsons, 2006, Ferrari et al., 2007).

In the southern Basin and Range, extension in the Colorado River Trough has been reported to be linked with basaltic volcanism that occurred during the Miocene epoch (e.g., Bradshaw et al., 1993). The geochemical composition of basalts found in this region have suggested origination of magma from the subcontinental lithospheric mantle. Following the main extensional event in the Basin and Range province, geochemical compositions of volcanic rocks changed, suggesting that magma was derived from both lithospheric and asthenospheric sources, likely due to lithospheric extension triggered magmatism in the southern Basin and Range during the Miocene (e.g., Bradshaw et al., 1993).

1.1.3 METAMORPHIC CORE COMPLEXES

In the southern Basin and Range province, rapid extension of the crust approximately 13 to 14 million years ago resulted in the development of metamorphic core complexes that are characteristic of the region. This age estimate was based on basin development thermochronology and the age of coeval volcanic rocks (e.g., John and Foster, 1993). In general, metamorphic core complexes in the southern Basin and Range are variably composed of mylonitic crystalline rocks, Miocene granitoids, and Proterozoic metamorphic basement rocks, including the Estrella Gneiss (e.g., Singleton et al., 2019).

Many metamorphic core complexes found in the southern Basin and Range region are proximal and roughly contemporaneous with volcanism and plutonism. In the Colorado River extensional corridor of the southern Basin and Range, volcanic rock ages are estimated to range from 21 to 26 million years ago (Foster and John, 1999).

The core complexes of the Sonoran Desert have been reported to be characterized by fabric development and thermal activity during the Mesozoic Era and Tertiary Period, with multiple episodes of ductile deformation identified in many of these core complexes. The core complexes are embedded with Tertiary plutonic rocks. Plutonic rocks in the Buckskin Mountains are dated at 21.7 million years ago. Tonalites in Whipple Mountains are approximately 24 to 26 million years old. Extension-associated plutons in the Chemehuevi Mountains are 21 to 19 million years old, 19 million years old plutons are recorded in Sacramento Mountains and the youngest at 18 million years old are in Dead and Newberry Mountains (Foster and John, 1999). Volcanic strata and granite are mixed in brittle structures and mylonitic fabrics. Some of mylonitic deformation granite bodies are of Miocene age. Processes in these geologic strata are estimated to have formed 18 to 25 million years ago (Nourse et al., 1994).

1.2 RESEARCH AREA AND SURROUNDINGS

1.2.1 GEOLOGIC SETTING

The research area is located on the western side of the Palo Verde Mountains, east of the Black Hills (Figures 2 and 3). It is surrounded by many tectonically active areas that contributed toward the current geology of the Palo Verde Mountains area. Around late Eocene to early Oligocene, episodes of faulting occurred in the Chocolate Mountains and the surrounding area (Sherrod and Tosdal, 1991). Following a period of relative tectonic quiescence from 22 to 33 Ma, the area from Palo Verde Mountains to the Trigo Peaks (Figure 2) underwent a major episode of extensional deformation and tilting. By around 13 Ma, thick alluvial fans filled many grabens and half-grabens among tilted fault blocks throughout the area (Sherrod and Tosdal, 1991).

1.2.2 REGIONAL ROCK UNITS

The following section is a brief overview of the major tectonic regimes and related rock units found in the vicinity of the research area that may have been a sediment sources for the Soledad Rojo formation, or represent post-Soledad Rojo depositional and geologic events. In addition, a potential source of Mesozoic- and Proterozoic-age sediments to the Soledad Rojo formation could have been from the San Gabriel Mountains, since this region was likely located to the south of the research area during deposition if ~300 km of right-lateral slip is removed from the San Andreas fault system (e.g., Nourse, 2002).

1.2.2.1 Precambrian to Paleozoic metamorphic and plutonic basement rocks

The most dominant pre-Tertiary rocks in the vicinity of the study area are plutonic and metaplutonic rocks of Mesozoic and Proterozoic age, with lesser metavolcanic and metasedimentary rocks of Jurassic age. The upper plates of Late Cretaceous thrust faults in the region are formed from these rocks. During early Tertiary time, these rocks underwent a period of rapid tectonic unroofing along low-angle normal faults (Haxel and Dillon, 1978; Haxel et al., 1985 Tosdal, 1990) and are now overlain nonconformably by Eocene to lower Miocene sedimentary and volcanic rocks (Sherrod and Tosdal, 1991).

The oldest rocks in the region of the study area are found in the southern Mule mountains and are assigned mostly to the Pinal Schist (Figures 2 and 3). The Pinal Schist consists mostly of fine-grained quartz-muscovite schist that are imperfectly foliated (Hayes and Landis, 1965). It is older than Paleozoic-age as it is intruded by a Precambrian hornblende-quartz diorite and younger rock units including the Cambrian Bolsa Quartzite are in contact with the Pinal Schist in the Mule Mountains (Gilluly, 1956; Hayes and Landis, 1965). The Cambrian Bolsa Quartzite consists mainly of evenly bedded, very resistant, siliceous sandstone with rounded to subrounded grains. Quartz grains make up most of the formation (around 80 to 90 percent); feldspar grains make up between 5 to 15 percent and the remainder 5 percent consist of traces of schist, quartzite, and opaque lithic fragments (Hayes and Landis, 1965). Another well-exposed formation found in the southern part of the Mule Mountains are the Middle-Late Cambrian Abrigo Limestone, which is subdivided into four lithologic units: a basal shaly unit, a ribbed limestone unit, a sandy unit, and the Copper Queen Limestone unit (Hayes and Landis, 1965). In addition, other Paleozoic-age formations found within the Mule Mountains are the Devonian Martin Limestone, the Mississippian Escabrosa Limestone, and the Pennsylvanian-Permian Naco Limestone (Hayes and Landis, 1965).

Additional Proterozoic-age rocks in the region that may have contributed sediment to the Soledad Rojo formation are found in the San Gabriel, Chocolate, and Little Chuckwalla Mountains. In San Gabriel Mountains, the oldest rocks are the quartzofeldspathic gneiss of Paleoproterozoic-age (around 1.7 Ga), which are intruded by gneissose granitic rocks of Paleoproterozoic-age (around 1.67 Ga) and a Mesoproterozoic-age (around 1.2 Ga) anorthosite-syenite-gabbro complex (Silver, 1971; Ehlig, 1981; Hoyt, 2012). In the Chocolate Mountains, the oldest rock found is an augen gneiss with U-Pb age of 1.7 Ga (Dillon, 1976; Hoyt, 2012). Anorthosite and syenite have an age of around 1.2 Ga in the Chocolate Mountains region, which look similar to the rocks found in the San Gabriel Mountains region (Silver, 1971; Hoyt, 2012). In the Little Chuckwalla Mountains, the oldest rock units are the augen gneiss dated to Paleoproterozoic-age (around 1.65 to 1.68 Ga) and a Mesoproterozoic-age (around 1.4 Ga) granite that most was metamorphosed to augen gneiss (Hamilton, 1982).

1.2.2.2 Mesozoic rocks

Within the Chocolate and Trigo Mountains, the structurally lowest lithotectonic unit within the metamorphic basement complex is the Orocopia schist (Figure 2), which is comprised of metamorphosed oceanic sedimentary and volcanic rocks of tentative Jurassic age (e.g., Haxel et al., 1985, 1987; Ricketts et al., 2011). The protolith of the Orocopia schist is suggested to have been metamorphosed during the Late Cretaceous due to underplating of the oceanic sediments underneath North American plate during subduction of the Farallon plate (Jacobson, 1990). The Orocopia schist is a quartzofeldspathic rock that contains metamorphic minerals of an amphibolite-grade. These minerals include quartz, oligoclase, albite, phengitic muscovite, and biotite (Jacobson et al., 2002; Ricketts et al., 2011).

Compared to the Pelona and Rand schists, the Orocopia schist has a higher proportion of Precambrian to Mesozoic detrital zircon grains (Chapman, 2016). Orocopia schist exposures along the Chocolate Mountains fault from east of middle Mountains to Chocolate Mountains (Figure 2) is juxtaposed with Mesozoic and Proterozoic gneiss and granitic rocks (Haxel et al., 2002; Chapman, 2016). In the Trigo and southern Chocolate Mountains, exposures of the Orocopia schist contain several 100-1000 m-thick metamorphosed gabbro and diorite lenses (Dillion 1976; Haxel et al., 2002, Chapman, 2016). U-Pb detrital zircon geochronology shows that the Orocopia schist within the vicinity of the research area have a maximum depositional age between 67.1 and 84.5 Ma (Barth et al., 2003; Grove et al., 2003, 2008; Jacobson et al., 2011; Chapman et al., 2013; Chapman et al., 2016; Dumitru et al., 2016; Chapman, 2016).

In Chocolate Mountains, the unit overlaying the Orocopia schist is a Jurassic-age mylonitic orthogneiss. Rocks within this unit are characterized by alternating bands of mafic and felsic materials (Ricketts et al., 2011). The unit overlying this orthogneiss is the Winterhaven Formation, which consists of metasedimentary and metavolcanic rocks. The metavolcanic rocks comprise the lower subunit of the Winterhaven Formation, with metamorphosed aphanitic to porphyritic andesitic to basaltic flows (Haxel et al., 1985; Sutton, 2010; Ricketts et al., 2011). The upper subunit of the Winterhaven Formation are metasedimentary rocks that consists of argillite, metamorphosed feldspathic and quartz arenite, and pebble conglomerate (Sainsbury 2010; Sutton 2010; Ricketts et al., 2011).

Mesozoic plutonic rocks within the Mule Mountains are enclosed on the west by a covered northeast-striking high-angle fault, with the Coon Hollow fault separating the Mesozoic plutonic rocks within the southernmost Mule Mountains from Tertiary volcanic rocks to the south that are thin or absent to the north of the Coon Hollow fault (Figure 3) (Sherrod and Tosdal, 1991). The Jurassic Juniper Flat Granite, like the Cambrian Bolsa Quartzite, is in contact with the Pinal Schist (Hayes and Landis, 1965). Potassium-argon ages of biotite samples from the Juniper Flat Granite are around 163 Ma and rubidium-strontium ages of biotite samples are around 177 Ma, which indicate an Early Jurassic-age (Creasey and Kistler, 1962). Younger Mesozoic rock units in the Mule Mountains include the Early Cretaceous Bisbee Group formations that unconformably overlain the Juniper Flat Granite (Gilluly, 1956; Hayes and Landis, 1964), which is subdivided into the Glance Conglomerate, Mural Limestone, Morita Formation, and Cintura Formation (Ransome, 1904; Hayes and Landis, 1964).

A small amount of Mesozoic metaplutonic rocks are observed in the eastern Palo Verde Mountains region, which are intruded by the Quechan volcanic rocks (described below). However, these Mesozoic rocks terminate to the northwest against the Flat Tops fault, which is an inferred fault based on the opposed dip directions of stratigraphic units on each side (Figure 3) (Sherrod and Tosdal, 1991).

1.2.2.3 Oligocene-Miocene: Volcanic and Sedimentary deposits

An arkosic sandstone and sedimentary breccia unit ("Prevolcanic Sedimentary unit" of Sherrod and Tosdal, 1991) that nonconformably overlies pre-Tertiary crystalline rocks in the Chocolate Mountains' upper plate is considered the oldest Tertiary rock unit in the region surrounding the study area. These rocks generally thin and appear finer grained to the northwest, north, and northeast from the Chocolate and southern Trigo Mountains (Figure 2), with coarse sedimentary breccias being abundant within the southern part of the Chocolate and Trigo Mountains (Sherrod and Tosdal, 1991). This sedimentary unit is inferred to be early Oligocene-as, as younger volcanism was well-established in the region by around 28 Ma (Sherrod and Tosdal, 1991).

The early stages of middle Tertiary volcanism (pre- 33Ma) are identified by a series of well-bedded volcanic litharenite and tuff overlying the pre-volcanic sedimentary rocks within the Chocolate Mountains region (Sherrod and Tosdal, 1991). This volcaniclastic strata is considered to represent reworked ash material erupted from distal explosive volcanic eruptions outside of the study area that was overlain by the locally erupted Quechan volcanic rocks around 33 Ma (Sherrod and Tosdal, 1991).

Several mafic to silicic volcanic rock units were locally erupted in the vicinity of the study area during the mid-Cenozoic. The Quechan volcanic rocks are the oldest Tertiary volcanic deposits, which were erupted in the Oligocene period (Crow,1978; Sherrod and Tosdal, 1991). The Quechan volcanic rocks consist of a series of lava flows and subordinate volcaniclastic strata that are exposed in the Palo Verde Mountains and Black Hills (Figure 3; Sherrod and Tosdal, 1991). A lower unit of lava flows that is lithologically similar to the Quechan volcanic rocks the and the tuff of black hills is assigned to the regional silicic tuff sequence. This unit is the oldest subunit of the silicic tuff sequence and shown in Figure 3 as dacite and rhyodacite unit (Sherrod and Tosdal,1991). Conformably overlying the Quechan volcanic rocks is a silicic tuff sequence composed mainly of rhyodacitic and rhyolitic pyroclastic flows. The silicic tuff sequence consists of at least four silicic pyroclastic deposits, including the tuff of Felipe Pass, tuff of Black Hills, tuff of Ten Ewe Mountain, and the ignimbrite of Ferguson Wash (Sherrod and Tosdal, 1991). Calderas identified in the Kofa Mountains (Figure 2) are the inferred eruptive source of at least two ash flow tuffs: the tuff of Felipe Pass and the tuff of Ten Ewe Mountain (Grubensky and Bagby, 1990; Sherrod et al., 1990; Sherrod and Tosdal, 1991; Grubensky et al., 1993). Tuff of Ten Ewe Mountain is widespread in Kofa and northern Castle Dome Mountains and possibly in Yuma Proving Ground, while the tuff of Felipe Pass is mostly discontinuously in the Lower Colorado River region from Little Chuckwalla Mountains to eastern Kofa Mountains (Figure 2) (Sherrod and Tosdal,1991). Ages for the silicic tuff sequence ranges from 23-27 Ma (Sherrod and Tosdal, 1991; Needy, 2009).

A smaller fraction of the volcanic rocks in the vicinity of the study area are considered to be younger than the silicic tuff sequence within the lower Colorado River region. The silicic tuff sequence is overlain by a Miocene dacite in the eastern Palo Verde Mountains (Sherrod and Tosdal,1991), by a younger (22 Ma) caldera-filling rhyodacite lava flows and domes in the Kofa Mountains (Bagby et al., 1987; Sherrod and Tosdal, 1991), by a bimodal assemblage of rhyolite and basalt that could be as young as 17 Ma in New Water and eastern Kofa Mountains (Sherrod et al., 1990; Sherrod and Tosdal, 1991), and by a few scattered silicic lavas in the Picacho State Park area (Crowe, 1978; Sherrod and Tosdal, 1991) (Figure 2). The youngest volcanic rocks in the research area vicinity are found as basalt lavas within Black Mountain, with ages as young as 9.6 ± 1.8 Ma (Eberly and Stanley, 1978; Sherrod and Tosdal, 1991).

Postvolcanic Miocene sedimentary rocks consist of arkosic conglomerate and sandstone that are reddish in color and is interbedded in the research area vicinity with the locally derived fanglomerate. This unit are characterized by micaceous sandy matrix and rounded clasts that are mostly of metaplutonic origin. These rocks are well exposed in the Palo Verde Mountains (including the Soledad Rojo formation) and are probably braidplain deposits of alluvial fans (Sherrod and Tosdal, 1991). The name “Tolbard Fanglomerate” was given to this formation in Midway Mountains and was tentatively correlated to the superficially similar Soledad Rojo formation (Berg et al., 1982; Jorgenson et al., 1982; Sherrod and Tosdal, 1991). However, the Tolbard Fanglomerate lacks a lot of the key characteristics of the Soledad Rojo formation, suggesting that these two units are not correlative (described below in the Discussion section)

Postdating the postvolcanic Miocene sedimentary rock sequence are distally derived arkosic sedimentary rocks and locally derived fanglomerate. These deposits are located in basins between the mountain ranges within our study area and its surroundings. The deposits are mostly poorly sorted conglomeratic sandstone and sedimentary breccia that accumulated as large alluvial fans in grabens and half grabens. This unit is given the name of conglomerate of Bear Canyon (Crowe, 1978; Sherrod and Tosdal, 1991) and has a wide age range between 9.45 and23 Ma (Ricketts et al., 2011).

1.2.2.4 Late Miocene to Holocene sedimentary deposits

Following deposition of the Quechan Volcanics and coeval sedimentary units, the late Miocene to Pliocene Bouse Formation and post-Bouse alluvium was deposited in the study area region (Figures 2 and 3). The Bouse Formation formed as a result of lacustrine and/or marine deposits that invaded the Palo Verde Valley during the development of the proto-Colorado River/Gulf of California system around 5 Ma, which resulted in the deposition of siltstone, limestone, and sandstone (Metzger, 1968; Smith, 1970; Sherrod and Tosdal, 1991).

In the region around the study area, the Bouse Formation is not visible except on the eroded flanks of the eastern Palo Verde Mountains close to the Colorado River (Figure 3; Sherrod and Tosdal, 1991). In Palo Verde Valley, the Bouse Formation is buried at a depth of 40m to 90m with the top of the formation at an elevation of ~25m to -15m relative to the sea level (Scarborough, 1985; Sherrod and Tosdal, 1991). This depth and elevation is variable within the region, as the top of the Bouse Formation at Blythe has an elevation of -72m (Sherrod and Tosdal, 1991).

The deposition and subsequent erosion of the Bouse Formation is thought to have preceded the formation of the Colorado River. Dillon (1976) assert that the river was formed as a result of the erosion of Bouse embayments and Quaternary faulting changed the course of the Colorado River from its ancestral route (see Figure 2) to its present course between the Trigo and Chocolate Mountains (Sherrod and Tosdal, 1991; Johnson and Miller, 1980). Post-Bouse Formation deposition in the Palo Verde Mountains, Black Hills, and Mule Mountains region consisted of wide alluvial fans that border these topographic features (Sherrod and Tosdal, 1991).

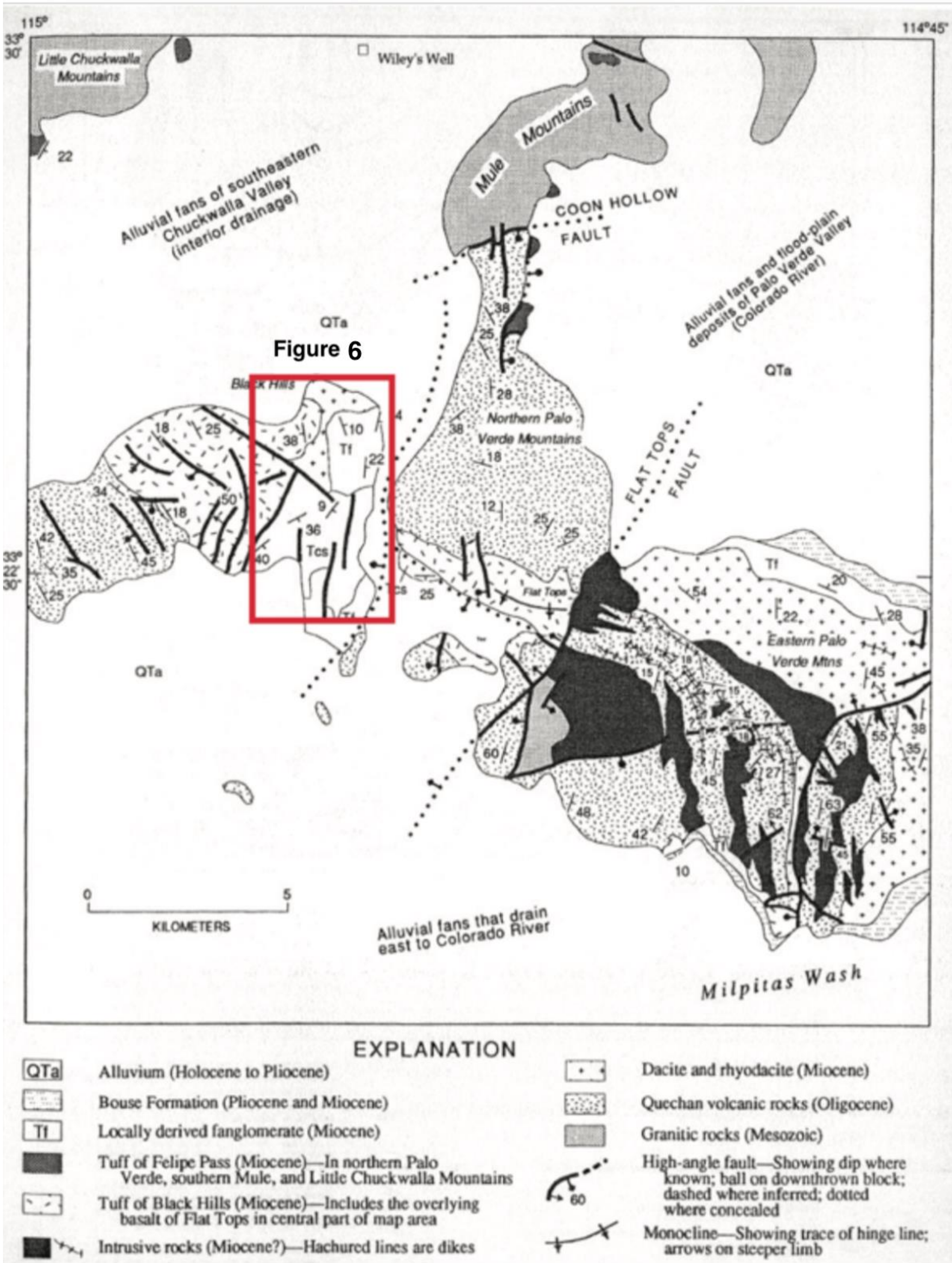

Figure 3: Simplified geologic map of the Palo Verde Mountains & Black Hills. The red box shows the location of Figure 6, which represents the research area (from Sherrod and Tosdal, 1991).

1.2. 3 REGIONAL SEISMIC PROFILES

In the western region of the Palo Verde Mountains and the Black hills, series of northwest normal faults that are dipping in the northeast were observed (Sherrod and Tosdal, 1991). Seismic reflection profiles of the southeastern California region show the combined impacts of structural deformation imposed on the Palo Verdes Mountains region as a result of the combination of the thrust faulting during the Mesozoic period followed by crustal extension during the mid-Cenozoic that resulted in detachment faulting in some parts of the region, and movements along transform faults during the Miocene period to present, which all resulted in the extensional geologic and topographic features that can be easily observed in the region today (e.g., Morris, 1993).

The analysis of seismic reflection data from the Milpitas Wash basin, located immediately south of the study area (Figure 3), interprets that the upper crust is made up of a series of fault blocks that tilt from medium to high angle normal faults and that there are two other sub-basins that underlie the topography (Figure 4**)**. Since the seismic reflection profiles were shot on a west to east alignment, the dips shown on the interpreted cross-section are apparent dips of the faults in the Milpitas Wash topographic basin. Furthermore, the faults also extend deeper into the crust in which they appear to sole into zones of strong reflectivity, interpreted as a low-angle detachment fault (décollement) or some form of extensional fabric that likely developed during the Miocene period of Tertiary extension (Morris, 1993).

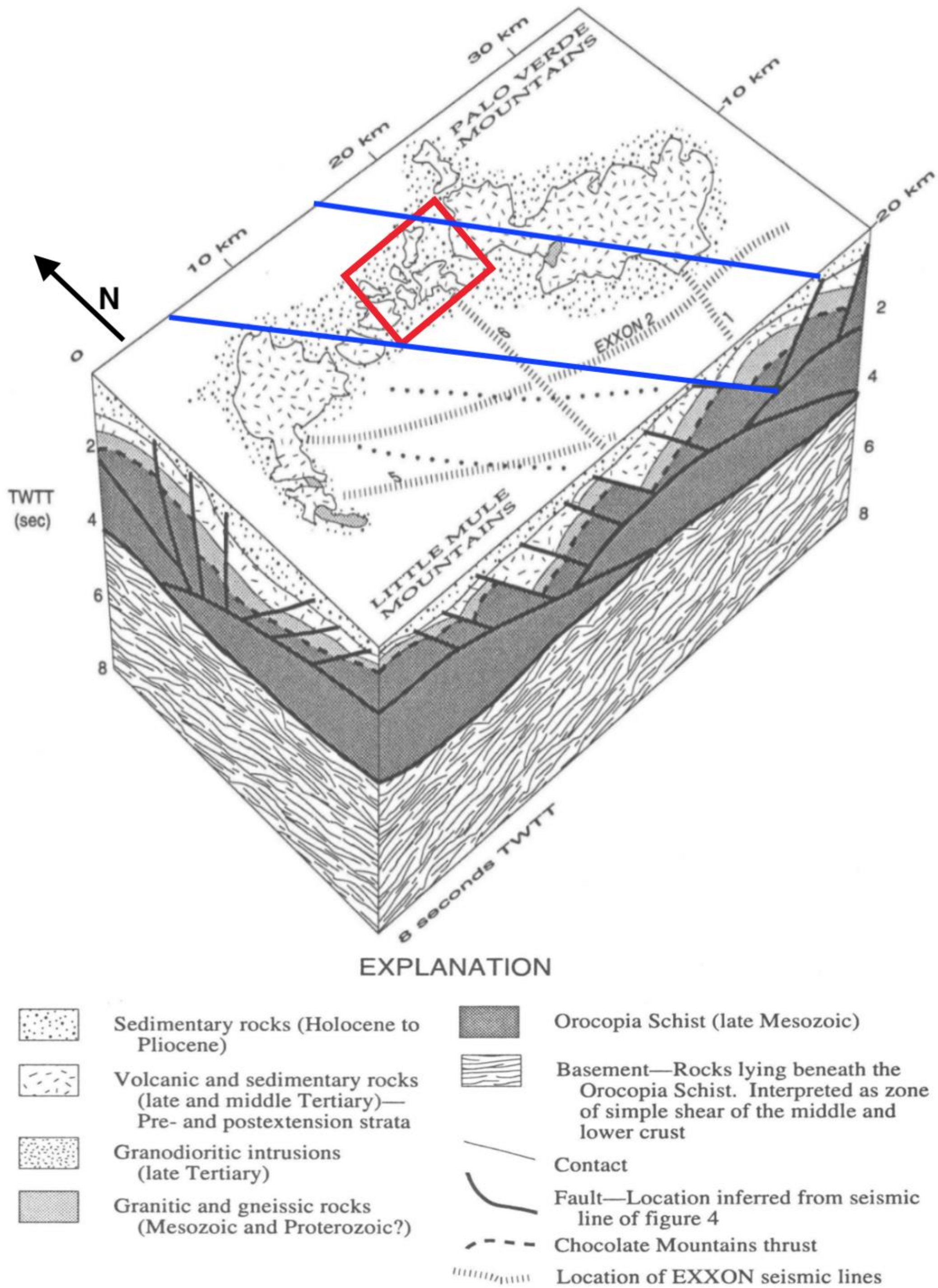

Figure 4: Isometric diagram showing the upper crust in the vicinity of the research area based on reprocessed seismic profiles and surface geology (from Morris, 1993). The long side of the diagram represents crustal structure interpreted from seismic line 2, while the short side represents line 6 (Morris, 1993). A key Tertiary structural feature in this diagram are the high-angle faults that are associated with half graben tilt blocks. Red box represents the research area shown in Figure 6. Blue lines show the inferred faults continuation that might be the study basin boundaries.

1.3 SOLEDAD ROJO FORMATION: WHAT IS ALREADY KNOWN

The Soledad Rojo formation, an informal name given by Elliott and Marshall (2012), is a moderately east-dipping, well indurated gravelly red bed stratigraphic unit exposed on the western side of the northern Palo Verde Mountains of southeastern California (Figure 3). This formation consists primarily of conglomerates that are orange to light red-colored with clasts composed mainly of volcanic rocks and granitic-metamorphic basement rocks. In addition, Elliot and Marshall (2012) identify the noteworthy presence of quartz arenite clasts in the Soledad Rojo formation and suggest that these clasts are far traveled. Paleocurrent directions in the Soledad Rojo formation indicated by conglomerate clast imbrications is on average east-southeasterly directed with ±30 degrees error (Elliott and Marshall, 2012). The Soledad Rojo formation is tentatively correlated to the Tolbard Fanglomerate formation (e.g., Elliot and Marshall, 2012), which is located in the Midway Mountains area south of the study area (Figure 2). The Tolbard Fanglomerate is made up of reddish brown and well indurated alluvial fan deposits of similar appearance to the Soledad Rojo formation (Elliott and Marshall, 2012 and references therein). Further elaboration on these potential formation correlations will be described below in the Discussion section.

CHAPTER 2 – METHODS

2.1 FIELD TRIPS

The first field trip to the study area was in December 2016 over a weekend with Dr. Murray. During this trip, reconnaissance mapping was conducted to get a general idea of the nature of the rocks within the study area. Rock descriptions, preliminary geologic mapping, and several strike and dips measurements were taken, and we decided to move forward with this area for our research.

The second field trip to the study area was part of the GSC 491L Field Module class I took with Dr. Murray in the Spring of 2017, with field work conducted over the course of six days. During this field trip, an initial geologic map for the research area was developed with different subdivisions for the Soledad Rojo formation. Detailed sedimentological descriptions of the rock units observed within the study area were recorded. A Jacob's staff in combination with a Brunton compass inclinometer was used to measure a stratigraphic section in the northern part of the study area near Tadpole Tanks. The total measured stratigraphic section thickness was around 44 meters, covering the lower to middle part of the Soledad Rojo formation. This spot was chosen because it was within a wash area with excellent vertical rock exposure that allowed for more accurate data collection by making it easier to recognize the different sedimentary subunits within the Soledad Rojo formation as well as noticing all the structural features such as faults in three-dimensional view. In addition, some samples were collected along the stratigraphic section for point-counting analyses to identify potential textural and compositional changes. By the end of this trip, a better understanding of the research area was developed, and a more accurate geologic map was made with more details and structural features.

The third and fourth field trips to the study area were in the Spring of 2018 to collect additional samples for laboratory analyses. Most of these samples were collected in the Tadpole Tanks wash where the stratigraphic column was measured. A sample was collected from each stratigraphic subunit within this measured section, as well as from other various locations within the research area, to be used for thin section point counting and detrital zircon U-Pb ICP-MS dating purposes. The samples' locations were chosen based on the mapping and stratigraphic data collected from the first two field trips that suggested a slight difference in sedimentary textures and clast compositions between different subunits of the Soledad Rojo formation that was worth checking with additional lab analysis. In addition, new areas were visited during these latter field trips to expand the original geologic map and to observe if there are any other formations found in the study area or if additional stratigraphic changes are identifiable within the Soledad Rojo formation. The final geologic map of the study area is covering an area around 21 km^2, originally mapped at a scale of 1:12,000 using a topographic base map and aerial photographs.

2.2 SEDIMENT PROVENANCE METHODS

2.2.1 THIN SECTION POINT-COUNTING ANALYSIS

Several rock samples selected from various locations within the research area were used to make thin sections for point-counting analysis. They were chosen based on their differences in grain characteristics and distance from other samples. From the measured stratigraphic column, a sample from each subunit was used for thin section analysis to document any upsection sedimentological changes in the Soledad Rojo formation.

In order to create a thin section, the sample is first cut with a rock saw into a chip that has approximately a 2 cm width by 4 cm length and a thickness of around 1.5 cm. It has to be slightly smaller in size compared to a thin section. The sample should be cut perpendicular to any depositional fabrics present in the rock. After cutting the rock chip, it was thoroughly cleaned and labeled on the side not to be glued to the slide glass. The finished rock chips were sent to Precimat thin section laboratory to complete the thin section preparation process.

The first step in thin section preparation is to glue the rock chip to the glass slide and ensure there is a constant thickness. Corners and other parts that are not level are ground using a grinding wheel. Water is poured into the spinning wheel and around the plastic bucket for the purpose of washing the grit away. To prepare the glass slide, it should be frosted or roughed so that epoxy can bind well. To successfully cut the slap, it should be attached to clamp that is parallel to the blade. The frosted side of the slide is attached to the chip that is grounded. Constant thickness of epoxy should be maintained across the section. As the rock chip is now attached to the glass slide, the next step is to cut most of it off from the slide, ensuring that a thin chip is left attached to the slide. The rock that remains attached to the slide must be a further ground to ensure that the slide is of the correct thickness (~30 µm), being careful not to grind away the entire sample.

Once the thin sections were ready, a point count analysis using the petrographic lab microscope at California State Polytechnic University, Pomona. Four hundred (400) counts per sample were identified to study each sample's composition. Framework grains that are either minerals, rock fragments, or other constituents were counted (Table 1). If the microscope crosshairs fell on the matrix, cement, or pore space, the point was skipped and the thin section was advanced to the next grain to be counted. These data were used and in other cases recalculated as shown in Table 1 to generate a quartz-feldspar-lithics, monocrystalline quartz-feldspar-total lithics, and quartz-potassium feldspar-plagioclase. The raw data results of the point counting are shown in Table 2 in the results section. A total of 12 samples were analyzed in the lab, and are displayed on QFL, QmFLt, and QKP diagrams.

Symbol	Grain categories	Recalculated parameters
Qm	Monocrystalline quartz	Q = Qm + Qp
Qp	Polycrystalline quartz	
K	Potassium feldspar	F = K + P
P	Plagioclase feldspar	
Lv	Volcanic lithic fragments	L = Lv + Lm + Ls Lt = L + Qp
Lm	Metamorphic lithic fragments	
Ls	Sedimentary lithic fragments	
Hem	Hematite	
Cal	Calcite	
Bt	Biotite	
Opq	Opaque	
Ol	Olivine	
Gls	Shredded glass	

Table 1: Grain-type symbols and categories, with the recalculated parameters used to generate the normalized compositional tables and ternary diagrams (Tables 2 and 3; Figure 17).

2.2.2 DETRITAL ZIRCON U-Pb GEOCHRONOLOGY

Four sandstone samples from the Soledad Rojo formation were selected for detrital zircon U-Pb LA ICP-MS geochronology. Mineral separations for these analyses were conducted at California State Polytechnic University, Pomona (Cal Poly Pomona). The separation process starts by thoroughly cleaning the workstation to make sure that no contamination from previous rocks used in the lab will occur. Then, the samples were carefully washed with water to remove any dirt on them that might affect our results. The samples are then dried using an air blow gun and left on paper tissue to dry. Once dry, each sample was broken apart to smaller fragments by crushing it on a metal plate using a sledgehammer (Figure 5A). After that, all of the broken pieces were collected and placed in individual sample bags (Figure 5B). The next step of the process is to use the rock grinder to further crush the rock fragments into a fine powder. First, the rock grinding machine was thoroughly cleaned, and the grinding plates were prepared to the proper spacing (Figure-5C). The broken pieces of the sample were then poured into the grinding machine (Figure-5D) and the finer particles were collected. Cleaning of the whole workstation and the equipment used was done after completing each sample. Following grinding, each sample was placed in four different containers that contained a 10% acetic acid solution used to dissolve any carbonate grains or cement (Figure 5E); this process was repeated until no more fizzing or reactions occurred, then the samples were rinsed with water (Figure 5F). Finally, each sample was further separated using the Gemini water table technique to segregate and collect the higher density minerals (including zircon) from the lower density material (Figure 5G).


A
B
C
D
E
F
G
HDX

Figure 5 (previous page): The procedure to start mineral separation process that was done at California State Polytechnic University, Pomona. The process started by cleaning the workstation and the samples that will be used to avoid sample contamination. Once the samples are dry, using a sledgehammer, each sample was broken apart to smaller fragments by crushing it on a metal plate (Figure 5A). After that, all the broken pieces were collected and placed in individual sample bags (Figure 5B). Then, the rock grinder was used to further crush the rock fragments into a fine powder (Figure 5C). The broken pieces of the sample were then poured into the grinding machine and the finer particles were collected (Figure 5D). Following grinding, each sample was placed in four different containers that contained a 10% acetic acid solution used to dissolve any carbonate grains or cement (Figure 5E); this process was repeated until no more fizzing or reactions occurred, then the samples were rinsed with water (Figure 5F). Finally, each sample was further separated using the Gemini water table technique to segregate and collect the higher density minerals (including zircon) from the lower density material (Figure 5G).

After completing preliminary mineral separations at Cal Poly Pomona, the high-density mineral separates were sent to Chemostrat Ltd labs (Houston, TX) to complete the mineral separation process, hand-pick and mount the zircons, and conduct detrital zircon U-Pb geochronology. Some of the preliminary separation steps were repeated by Chemostrat to minimize error in the process, including "sieving the samples to retain the 40µm to 250µm grain size fractions, washing these fractions in an ultrasonic bath and subsequently treating with a 10% acetic acid solution in order to dissolve any carbonate grains / cements that may still be present. High-density grains were separated from lower density material by using a sodium heteroploytungstate solution (LST Fastfloat - 2.89 g/cm^3) combined with the funnel separation technique described by Mange & Maurer (1992). After further separation using a Frantz magnetic separator (at a current of 1.8 amperes), the heavy mineral separates were mounted in resin pucks that were then polished to approximately half their depth. Zircon grains were mapped by scanning electron microscope (SEM) to generate target coordinates for laser ablation. U-Pb ages for the detrital zircons were obtained by employing laser ablation inductively coupled plasma mass spectrometry (LA-ICP-MS) using a Thermo Scientific iCAP Q ICP-MS. A laser diameter of 25 microns was used for all analyses. Mass and instrument bias were monitored constantly and accounted for by using sample-standard bracketing with the 91500 zircons as the primary standard and the Plešovice zircon (Sláma et al., 2008) as a secondary standard. Raw data were processed using Iolite software (Paton et al. 2011). To ensure that final dataset contains U-Pb ages from zircons only, all data were screened using 178Hf counts. Hf is incorporated into zircon crystal lattice and is therefore abundant at the percent level in zircon (e.g., Belousova et al., 2002). All zircon analyses were displayed on concordia diagrams (Ludwig, 2008) to check the data for any major peculiarities and for geologically significant discordia arrays. The single analysis concordia age was calculated for each analysis and these ages were used for plotting and interpreting the data. This age has the advantage of being more precise than both the $^{206}Pb/^{207}Pb$ ages and the $^{206}Pb/^{238}U$ ages (Zimmermann et al., 2017) and therefore removes the need to switch between isotope systems at a given age (typically 1.0 Ga). The data were filtered using a threshold of >0.001 for the probability of concordance, a statistic which is calculated simultaneously to the concordia age. Accepted data from each sample were then plotted on histograms (25 Ma bin width) and kernel density estimation (KDE; 20 Ma bandwidth) plots (Vermeesch, 2012).” (Chemostrat Ltd Lab, 2019). See Appendix A for detailed results of each U-Pb analysis and Appendix B for Concordia diagrams.

CHAPTER3 – RESULTS

3.1 FIELD WORK DATA ANALYSIS

This study divides the Soledad Rojo formation into three stratigraphic subunits (Figures 6, 7, and 8): 1) a lower alluvial unit (Tsrl), consisting primarily of trough cross bedded brick red coarse-grained lithic arkose interbedded with subangular-subrounded cobble conglomerate; 2) a middle fluvial unit (Tsrm) of clast-supported, rounded-subrounded cobble-boulder conglomerate interbedded with brick red lithic arkose similar to lower unit; and 3) an upper alluvial unit (Tsru) of interbedded light gray-buff conglomeratic lithic arkose and subangular-subrounded pebble-cobble conglomerate Silicic and mafic volcanic rocks (Tbh, Tsrv) underlie and are intercalated with the Soledad Rojo formation red beds, and a younger dacitic intrusion (Td) crosscuts the basin deposits in the northern part of the study area (Figures 6 and 7). Descriptions of the map units found in the study area are provided in further detail below.

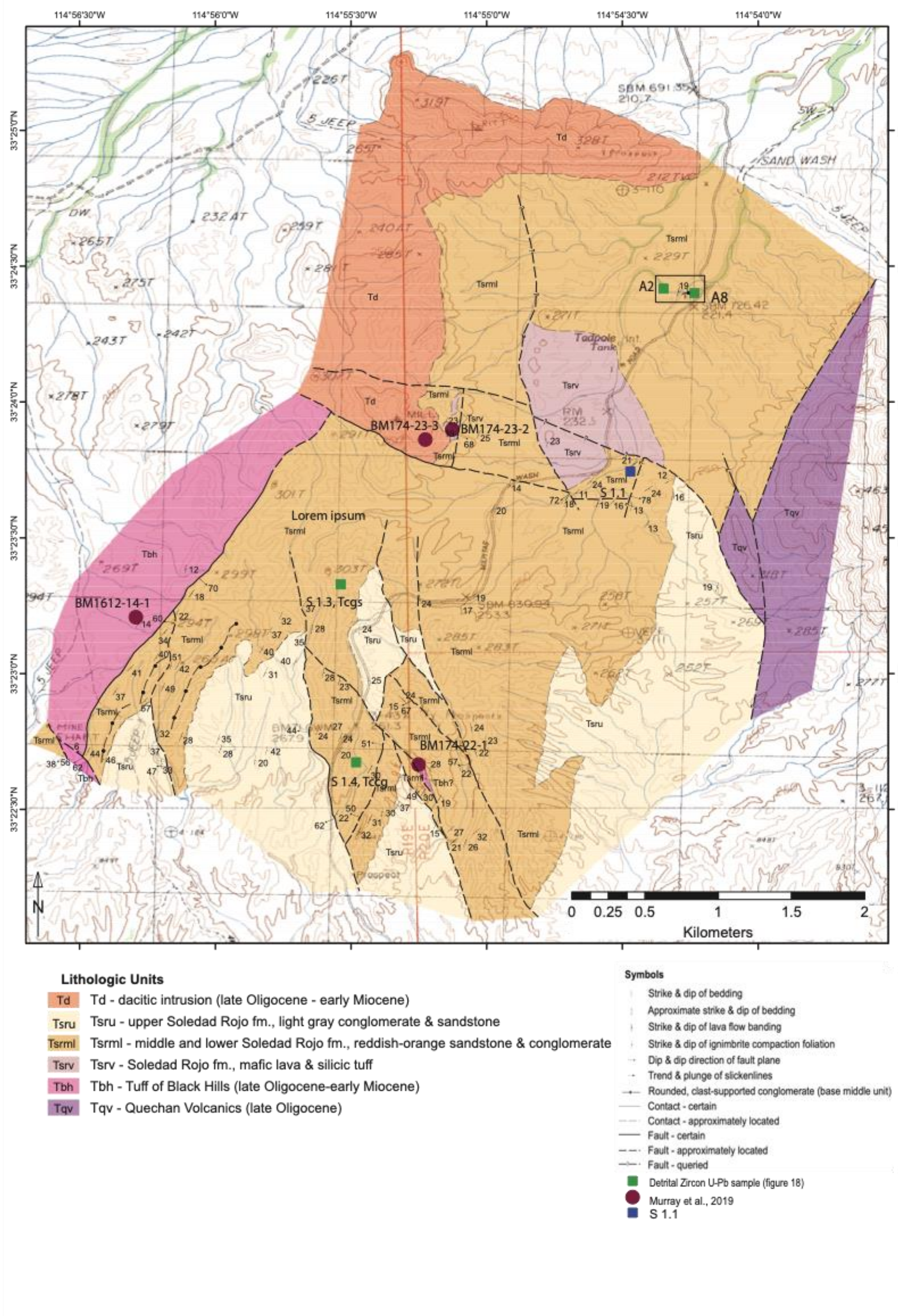

114°56'30"W
114°56'0"W
114°55'30"W
114°55'0"W
114°54'30"W
114°54'0"W
33°25'0"N
33°24'30"N
33°24'0"N
33°23'30"N
33°23'0"N
33°22'30"N
Td
Tsrml
Tsrv
Tsru
Tbh
Tqv
A2
A8
Tadpole Tank
BM174-23-3
BM174-23-2
S 1.1
Lorem ipsum
BM1612-14-1
S 1.3, Tcgs
S 1.4, Tccg
BM174-22-1
Tbh?
SAND WASH
N
0 0.25 0.5 1 1.5 2
Kilometers
Lithologic Units
Td - dacitic intrusion (late Oligocene - early Miocene)
Tsru - upper Soledad Rojo fm., light gray conglomerate & sandstone
Tsrml - middle and lower Soledad Rojo fm., reddish-orange sandstone & conglomerate
Tsrv - Soledad Rojo fm., mafic lava & silicic tuff
Tbh - Tuff of Black Hills (late Oligocene-early Miocene)
Tqv - Quechan Volcanics (late Oligocene)
Symbols
Strike & dip of bedding
Approximate strike & dip of bedding
Strike & dip of lava flow banding
Strike & dip of ignimbrite compaction foliation
Dip & dip direction of fault plane
Trend & plunge of slickenlines
Rounded, clast-supported conglomerate (base middle unit)
Contact - certain
Contact - approximately located
Fault - certain
Fault - approximately located
Fault - queried
Detrital Zircon U-Pb sample (figure 18)
Murray et al., 2019
S 1.1

Figure 6 (previous page): Geologic map of the Soledad Rojo formation basin in the western Palo Verde Mountains/Black hills. The Soledad Rojo formation is gently to moderately dipping towards the east and is offset by several north-northwest striking, west dipping normal-oblique faults. The basin is bounded on the east by a poorly exposed northeast striking, northwest dipping normal fault, with the Quechan Volcanics (Tqv) in the footwall (Sherrod and Tosdal, 1991, and references therein). The west side of the basin is bounded by a northeast striking, southeast dipping normal fault with the Tuff of the Black Hills in the footwall (Murray et. al., 2019). The location of the Tadpole Tank measured section (Figure 8) is indicated by a black box. Locations for detrital zircon samples analyzed for this study (Figure 18) are indicated by green squares. Red circles indicate the locations of $^{40}Ar/^{39}Ar$ samples from Murray et al. (2019).

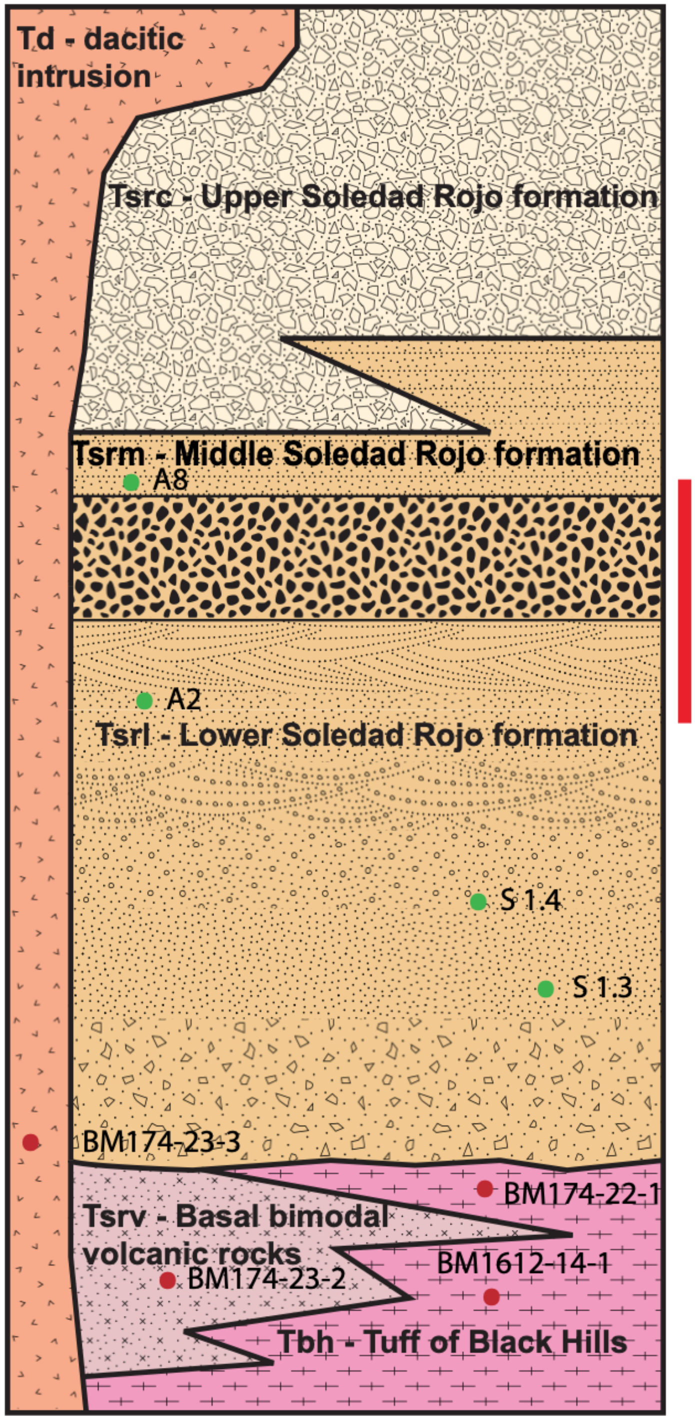

Figure 7: Generalized stratigraphic column depicting the depositional relationships of the Soledad Rojo formation (see text for detailed descriptions of the rock units). The depositional relationships between Tsrv and Tbh are uncertain due to limited exposure. The red bar roughly corresponds to the stratigraphic position of the Tadpole Tank measured section (Figure 8). Red dots represent the location of samples that were dated using $^{40}Ar/^{39}Ar$ geochronology (Murray et al., 2019), and green dots represent the location of samples that were dated using U-Pb geochronology.

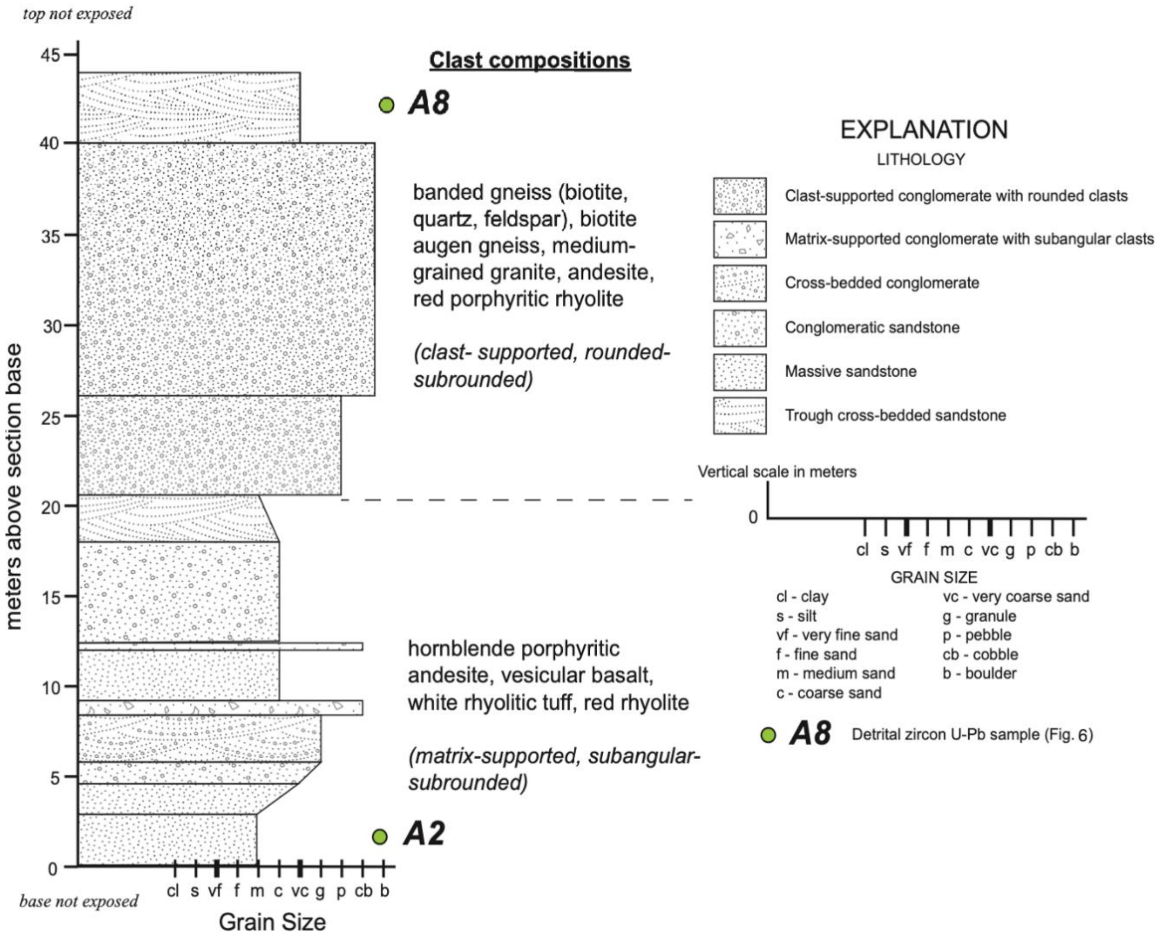

Figure 8: Measured stratigraphic section of the lower to middle Soledad Rojo formation near Tadpole Tank (Figure 6). Dashed line indicates the boundary between the lower and middle units, with rounded to subrounded clast-supported cobble to boulder conglomerate of middle unit above (marker bed in Figure 6) and subangular-subrounded sandstone & matrix supported conglomerates of the lower unit below. Stratigraphic location of detrital zircon U-Pb samples in Figures 6 and 18 is indicated.

3.1.1 Stratigraphic Units of the Soledad Rojo formation

3.1.1.1 Tbh: Tuff of Black Hills

The Tuff of Black Hills is part of the silicic tuff and pyroclastic flow sequence that is widespread across the research area and its surroundings, including the Black Hills, Palo Verde Mountains, Chocolate Mountains, Trigo Mountains among others (Figures 2 & 3). Figure 9 shows a panoramic photograph looking northeast at the western margin of the

Soledad Rojo basin, and the hill near the center of the photograph consists of the Tuff of Black Hills (Figure 6; BM1612-14-1), The Tuff of Black Hills is the welded ignimbrite unit observed in a few localities within the research area (Figure 6), consisting of a light red to orange groundmass with dark gray flame that become white pumice fragment upsection. It contains 5-10% phenocrysts of biotite, sanidine, and quartz, with reddish to gray silicic volcanic rock fragments that are up to 1 cm-diameter (Figure 10). Reported ages for the Tuff of Black Hills range between 22-27 Ma, and this unit is possibly correlated to the ignimbrite of Ferguson Wash that was likely erupted close to Picacho State Park (Figure 2; Sherrod and Tosdal, 1991).

Figure 9: Panoramic photograph looking northeast at the western margin of the Soledad Rojo basin. The hill near the center of the photograph consists of the Tuff of Black Hills (Figure 6; BM1612-14-1), a resistant welded ignimbrite dipping ~15° SE that overlies white tuffaceous volcaniclastic rocks in the low-lying area to the west. East of this central hill is the basin-bounding SE-dipping normal fault (white dashed line), with ~40° SE-dipping lower-middle Soledad Rojo formation sedimentary rocks in the hanging wall.

Figure 10: The tuff of the Black Hills (welded ignimbrite) has a light red to orange groundmass with dark gray flame that become white pumice fragment upsection. It also contains 5-10% phenocrysts of biotite, sanidine, and quartz, with reddish to gray silicic volcanic rock fragments that are up to 1 cm-diameter. (A) shows a fresh sample (B) shows a weathered sample of the Tuff of the Black Hills taken from location labeled as BM174-22-1 in Figure 6. ages for the Tuff of Black Hills range between 22-27 Ma, and this unit is possibly correlated to the ignimbrite of Ferguson Wash that was likely erupted close to Picacho State Park (Figure 2; Sherrod and Tosdal, 1991).

3.1.1.2 Tsrv: Basal bimodal volcanic rocks

Bimodal (mafic/silicic) volcanic rocks are locally underlying and interbedded with the Soledad Rojo formation. This rock unit consists of gray, vesicular, flow-banded basaltic lava with 10-15 % olivine and plagioclase phenocrysts, as well as tan rhyodacitic nonwelded tuff with 5% phenocrysts of biotite, quartz, and plagioclase and trace gray volcanic lithic fragments (Figures 6, 7, and 11). A sample of this nonwelded tuff (BM174-23-2; Figure 6) was dated by $^{40}Ar/^{39}Ar$ geochronology, indicating a ca. 22.5 Ma age of this unit (Murray et al., 2019). Interbedded with the bimodal volcanic rocks are volcaniclastic granule to pebble conglomerates that are poorly sorted, light brown in color, clast-supported, and contain mostly angular to subangular volcanic rock fragments (Figure 11). The lithofacies assemblage of this unit suggests that these conglomerates are the results of fluvial or debris flow deposition in this area.

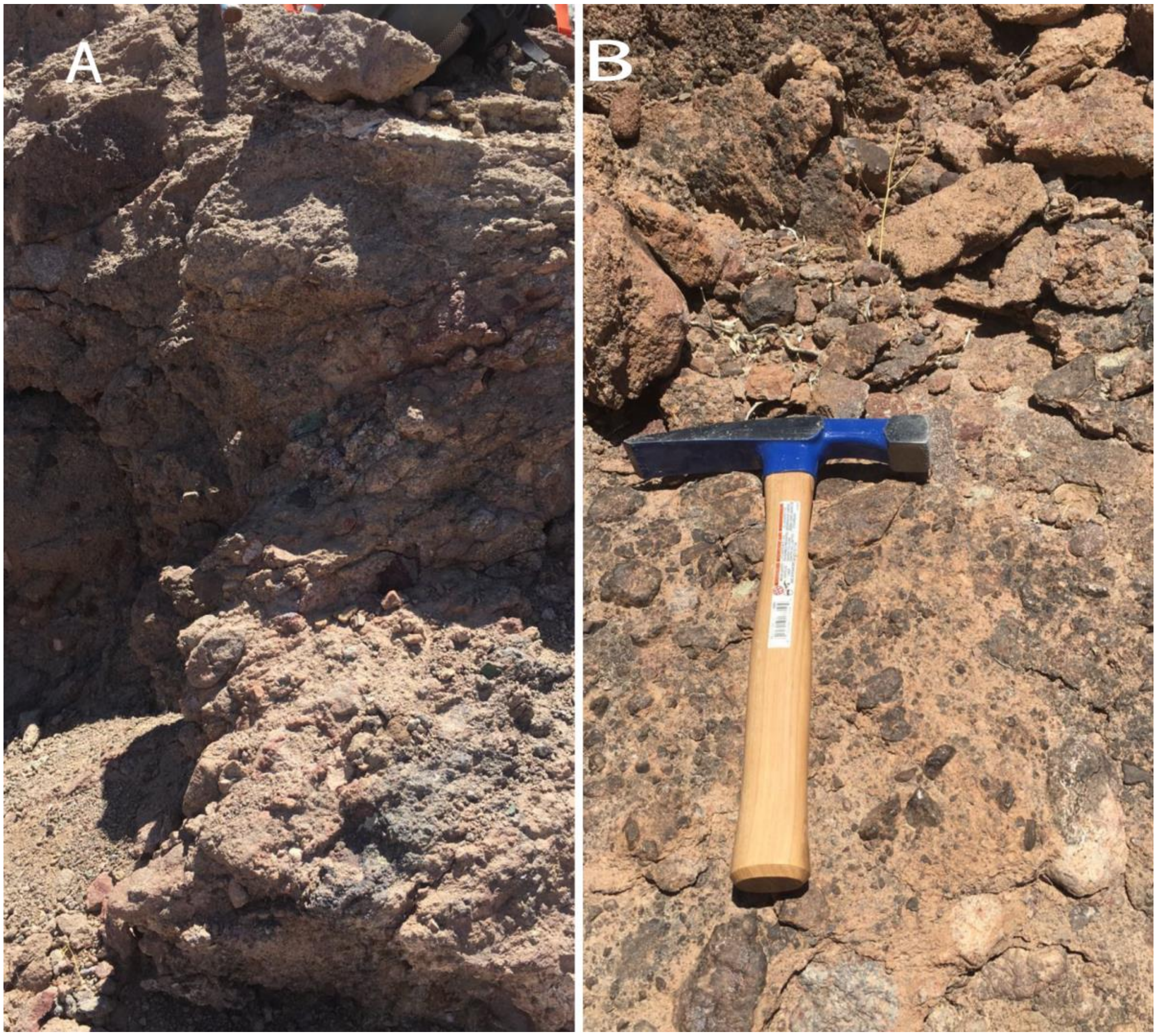

Figure 11: This figure shows the basal bimodal (mafic/silicic) volcanic rocks (Tsrv) that are locally underlying and interbedded with the Soledad Rojo formation consisting of gray, vesicular, flow-banded basaltic lava with 10-15 % olivine and plagioclase phenocrysts, as well as tan rhyodacitic nonwelded tuff with 5% phenocrysts of biotite, quartz, and plagioclase and trace gray volcanic lithic fragments (shown in Figure 11A). Interbedded with the bimodal volcanic rocks, are volcaniclastic granule to pebble conglomerates (shown in Figure 11B) that are poorly sorted, light brown in color, clast-supported, and contain mostly angular to subangular volcanic rock fragment. These conglomerates are the results of fluvial or debris flow deposition in this area.

3.1.1.3 Tsrl: Lower Soledad Rojo formation

The rocks of the lower unit of the Soledad Rojo formation are characterized by red, medium- to coarse-grained lithic arkose sandstones and conglomeratic sandstones (Figures 6, 7, and 8). These deposits are moderately sorted and subangular to subrounded, with trough cross-bedding, horizontal lamination, channel scours, and thin granule to pebble conglomerate lenses. Red matrix-supported conglomerates are interbedded with the sandstones that have grain sizes ranging from pebble to small boulder and are poorly sorted with subangular to subrounded (locally angular) clasts derived from mafic-silicic volcanics and metamorphic/plutonic basement rocks (Figure 12). The lithofacies assemblage of the lower Soledad Rojo formation suggests that it resulted from braided fluvial deposition characterized by gravely rivers with numerous subsidiary channels deposited through lateral accretion of gravel bars (e.g., Miall, 1985)

Figure 12: These pictures represent the lower subunit (Tsrl) of the Soledad Rojo formation. Photos 12A and 12B are from the Tadpole Tank wash stratigraphic section (Figures 6 and 8), while Photo 12C is from another location within the research area. (A) shows deposits that are moderately sorted and subangular to subrounded, with trough cross-bedding, horizontal lamination, channel scours, and thin granule to pebble conglomerate lenses. (B) shows an alternating layer of coarse sandstone and pebble-cobble clast supported conglomerate with subrounded to rounded clasts. (C) red trough cross-bedded sandstone with interbedded pebble to cobble conglomerate lenses. Clasts are generally subangular with metamorphic, plutonic, & mafic-silicic volcanic compositions. This unit resulted from braided fluvial deposition characterized by gravely rivers with numerous subsidiary channels deposited through lateral accretion of gravel bars.

3.1.1.4 Tsrm: Middle Soledad Rojo formation

The middle unit of the Soledad Rojo formation primarily consists of red, clast-supported, cobble-boulder conglomerates with rounded to subrounded, imbricated metamorphic, plutonic, and mafic-silicic volcanic clasts, interbedded with medium to coarse grained sandstone lenses (Figures 6, 7, 8, and 13). The sedimentary structures and lithofacies found within the middle Soledad Rojo formation suggest that these rocks are the result of braided fluvial deposition typified by numerous subsidiary channels with gravelly longitudinal bars and bedforms that developed through lateral accretion that is common in the bar complexes (e.g., Miall, 1985).

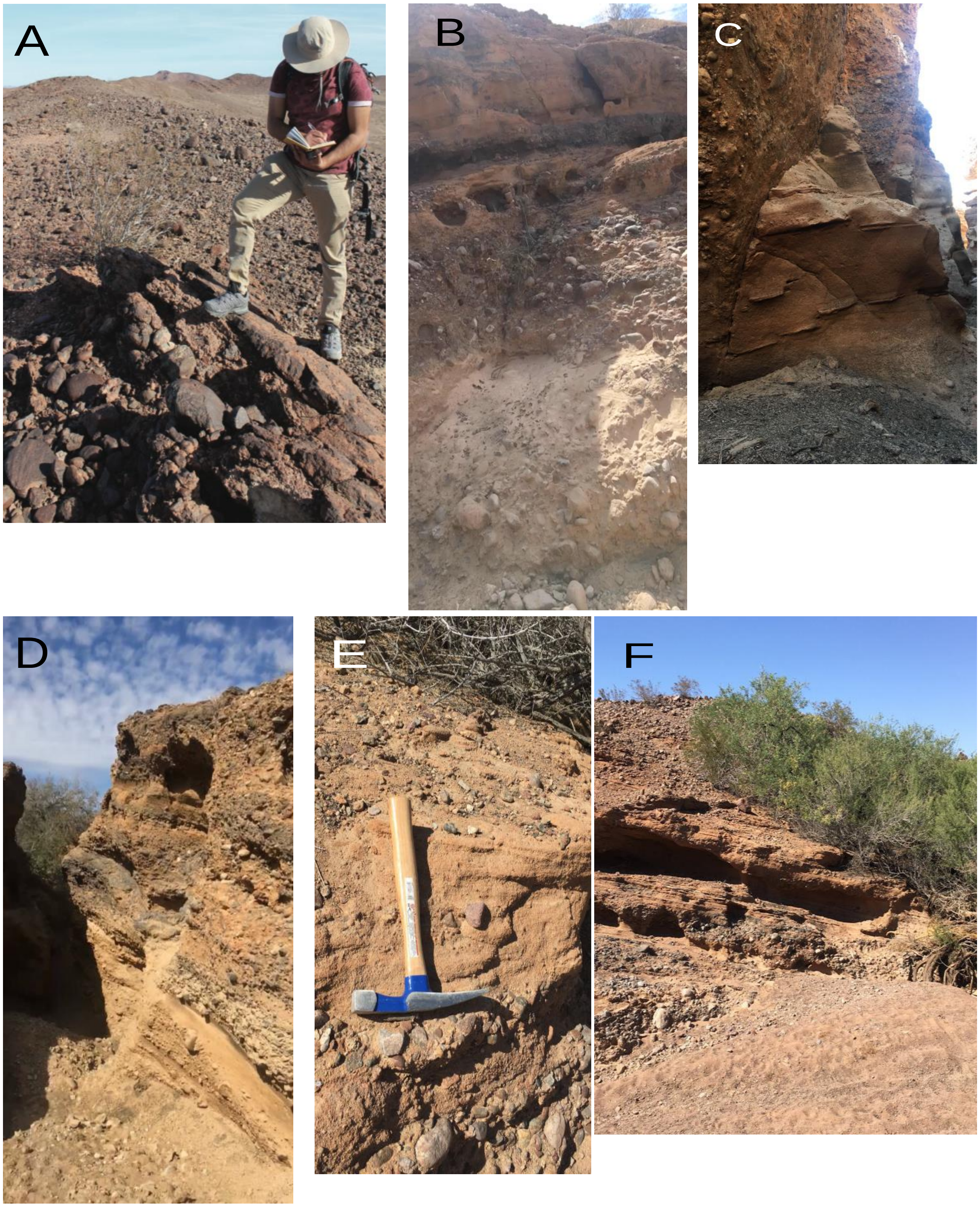
A
B
C
D
E
F

Figure 13 (previous page): These pictures are from the middle subunit (Tsrm) of the Soledad Rojo formation. All of the pictures are from the Tadpole Tank measured section (Figures 6 and 8) except (A), which is from another location within the research area. (A, B, and C) shows a clast-supported cobble-boulder conglomerate with rounded metamorphic, plutonic, and trace volcanic clasts (marker bed in Figure 6), interbedded with rough red cross-bedded sandstone. (B and C) shows the upper part of the Tadpole Tank wash stratigraphic column between 26-40 m (Figure 8). (D, E, and F) represents the upper portion of the Tadpole Tank wash stratigraphic column (Figure 8) showing the most top unit of a red very coarse trough cross-bedded sandstone. these rocks are the result of braided fluvial deposition typified by numerous subsidiary channels with gravelly longitudinal bars and bedforms.

3.1.1.5 Tsru: upper Soledad Rojo formation

The rocks of the upper unit of the Soledad Rojo formation are primarily light gray matrix-supported pebble-cobble conglomerates. These deposits are poorly sorted with subangular-subrounded clasts of metamorphic/plutonic basement and mafic-silicic volcanic rocks (Figures 6, 7, and 14). Interbedded with these pebble-cobble conglomerates are light gray, medium-to very coarse-grained arkosic sandstones, conglomeratic sandstones, and thin granule conglomerate lenses that are moderately to poorly sorted with subangular-subrounded grains. The lithofacies assemblage of the upper Soledad Rojo formation suggests deposition as debris flow and braided fluvial deposits, possibly in a proximal to medial streamflow-dominated alluvial fan system or outwash braid plain (e.g., Miall, 1985; Blair and McPherson, 1994,).

Figure 14: These pictures show the upper subunit (Tsru) of the Soledad Rojo formation. (A) is a light gray clast-supported polymictic cobble conglomerate with subangular-subrounded imbricated clasts. (B) shows a close-up of the same outcrop in (A), showing the metamorphic, plutonic, and mafic-silicic volcanic clast compositions with a light gray silty-sandy matrix. These rocks are the result of debris flow and braided fluvial deposits, possibly in a proximal to medial streamflow-dominated alluvial fan system or outwash braid plain.

3.1.1.6 Td: "Mill" dacitic intrusions

The youngest unit in the study area is the "Mill" dacite that crosscuts the Soledad Rojo formation deposits in the northern part of the study area (Figures 6, 7, and 15). This volcanic unit is light red with an aphanitic groundmass, 5-20% biotite and plagioclase phenocrysts, and small (<1cm) gray volcanic xenoliths. A sample collected from this unit for $^{40}Ar/^{39}Ar$ dating of sanidine and biotite (BM174-23-3; Figure 6) indicate an average age of ca. 20.5 Ma for this dacitic intrusion (Murray et al., 2019). The "Mill" dacitic intrusion is possibly correlated to similar intrusive units present in the Eastern Palo Verde Mountains that crosscut Mesozoic metaplutonic basement rocks and the Quechan volcanic rocks (Sherrod and Tosdal, 1991).

Figure 15: This figure shows the dacite intrusion unit, which is the youngest unit in the study area and is located at its northern part. (A) shows a photo taken from the MILPITAS WASH ROAD (Figure 6) facing northeast toward the dacitic intrusion unit marked as MILL in Figure 6. It has an estimated height of around 354 m. (B) shows the (Tsrv) subunit of the Soledad Rojo formation being cut-crossed by the dacitic intrusion. The Tsrv unit sits on top of the dacite unit. (C) shows a fresh rock with visible plagioclase phenocrysts that was just cut for lab analysis purposes. It is noticeable the difference in color due to weathering.

3.1.2 BASIN STRUCTURE AND GROWTH STRATA

The Soledad Rojo formation is gently to moderately dipping (~20-45^{o}) towards the east and is offset by several north-northwest striking, west dipping normal-oblique faults. The basin is bounded on the east by a poorly exposed northeast striking, northwest dipping normal fault, with the late Oligocene-Miocene (ca. 18-26 Ma) Quechan Volcanics (Tqv) in the footwall (Sherrod and Tosdal, 1991, and references therein). The west side of the basin is bounded by a northeast striking, southeast dipping normal fault with the late Oligocene (ca. 24 Ma) Tuff of the Black Hills in the footwall (Murray et. al., 2019). At one locality within the southern part of the map area, the Soledad Rojo formation is deposited unconformably upon a welded ignimbrite interpreted as the Tuff of the Black hills. An east-west trending fault that cut all of the study area units (Figure 6) extending from the oldest unit (Quechan Volcanics) on the east to the youngest unit (dacitic intrusion).

The regional seismic reflection profile (Figure 4) shows data from the Milpitas Wash basin that is located immediately south of the study area (Figure 3). The isometric diagram shows interprets that the upper crust is made up of a series of fault blocks that tilt from medium to high angle normal faults (Figure 3). Since the seismic reflection profiles were shot on a west to east alignment, the dips shown on the interpreted cross-section are apparent dips of the faults in the Milpitas Wash topographic basin. Furthermore, faults also extend deeper into the crust in which they appear to sole into zones of strong reflectivity, interpreted as a low-angle detachment fault (décollement) or some form of extensional fabric that likely developed during the Miocene period of Tertiary extension (Morris, 1993). Similar structural features including growth strata shown in Figure 16 were observed in the research area which is not far from the seismic profiles. This suggest a synextensional deposition of the Soledad Rojo formation. Several high-angle faults resulted from half-graben tilt were found within the basin.

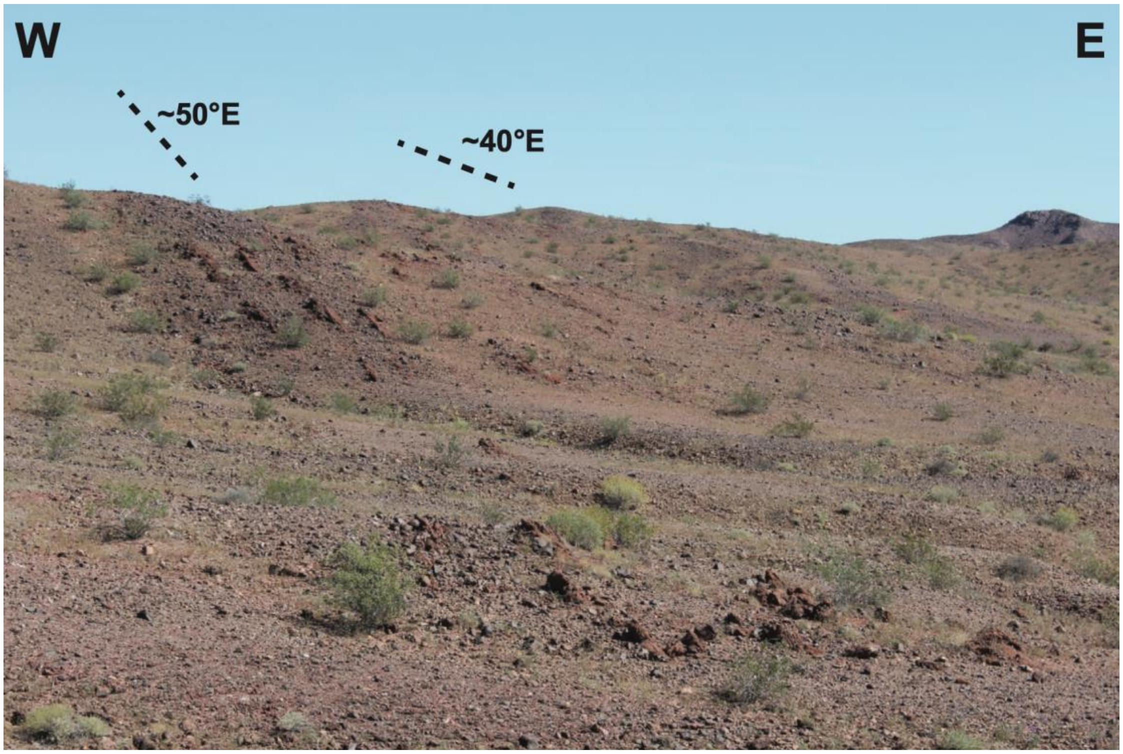

Figure 16: Evidence of possible growth strata (fanning bedding dips) in the lower subunit of the Soledad Rojo formation near the western margin of the basin, suggesting synextensional deposition. The darker red sandstone on the left dips ~ 50º east, which is overlapped by a lighter red sandstone dipping ~40º east near center of photograph.

3.2 SANDSTONE THIN SECTION POINT-COUNTING ANALYSES

Point-counting analyses for 11 sandstone thin sections provide the basis for the following compositional and provenance interpretations of the Soledad Rojo formation (Tables 2 and 3; Figure 17). Plagioclase feldspars are the most common constituent in the Soledad Rojo formation sandstones (Figure 17), with both of the Carlsbad (simple) and albite (multiple) twinnings observed. Microcline is also an abundant potassium feldspar, identified by its extinguished cross-hatched twinning. Quartz is moderately abundant in the formation in both monocrystalline and polycrystalline forms. For most samples, monocrystalline quartz grains exhibit straight extinction, however, there are some grains with wavy and undulatory extinction (e.g., Basu, 1985). Most of the polycrystalline quartz have more than four subdomains that goes extinct as in different parts of the grain with rotation. Volcanic lithic fragments are widely present within the Soledad Rojo formation and they come second to feldspars as far as their abundance. Basic volcanic rock fragments are the most common, consisting mainly of microlitic plagioclase and lathwork feldspars and very small opaque minerals (Adams et al., 2017; MacKenzie et al., 2017).

Several accessory minerals are present in the Soledad Rojo formation sandstones. Trace olivine was observed, characterized by its high birefringence and high relief. Biotite is a common mica found in most samples within the Soledad Rojo formation. Another mineral found in moderation is calcite. Calcite is the main component of marbles and is found in many metamorphic and igneous rocks; in the Soledad Rojo formation, calcite is observed as lithic fragments and as cement. Opaque minerals are relatively abundant and are not transparent to light making it difficult to distinguish the mineral type, but these grains are likely a type of iron-magnesium oxide (Adams et al., 2017; MacKenzie et al., 2017).

Table 2: This table shows the results of the point-counting analysis done on all the 11 samples of the Soledad Rojo Formation. A total of 400-point count per sample was done. Samples from A1-A8 were collected from the lower to middle Soledad Rojo formation from the Tadpole Tank section marked by a black box in Figure 6. Samples S1.1-S1.4 were collected from separate locations within the study area. These data were used to generate the QFL, QmFLt, QKP, LmLvLs ternary diagrams (Figure 17).

	Stratigraphic	Location		Minerals										Recalculated Parameters			
Sample	**Unit**	**Northig**	**Easting**	**Qm**	**Qp**	**P**	**K**	**Lv**	**Opq**	**Hem**	**Cal**	**Bt**	**Ol**	**Q**	**F**	**L**	**Lt**
A1	**Tsrl**	3698315	694779	5	35	253	55	0	18	7	12	5	10	40	308	5	5
A2	**Tsrl**	3698319	694777	16	26	171	35	65	35	13	23	6	10	42	206	81	81
A3	**Tsrl**	3698320	694789	14	19	236	47	23	9	28	19	5	0	33	283	37	37
A4	**Tsrl**	3698339	694807	10	19	247	29	39	10	29	15	2	0	29	276	49	49
A5	**Tsrl**	3698337	694834	3	10	252	36	15	14	30	20	9	11	13	288	18	18
A6	**Tsrm**	3698344	694860	4	15	210	18	92	18	23	13	4	3	19	228	96	96
A7	**Tsrm**	3698348	694861	4	10	237	23	104	3	11	0	6	2	14	260	108	108
A8	**Tsrm**	3968342	694919	1	10	223	63	54	13	12	6	12	6	11	286	55	55
S1.1	**Tsrl**	3697130	694595	4	15	91	21	221	32	10	0	5	1	19	112	225	225
S1.3	**Tsrm**	3696165	692975	47	15	123	62	119	10	1	19	4	0	62	185	166	166
S1.4	**Tsrm**	3695069	693068	86	37	118	89	31	3	18	12	6	0	123	207	117	117

The average composition Soledad Rojo formation sandstones are arkose to lithic arkose (e.g., Dott, 1964), with a high percentage of feldspar, less abundance of lithic fragments, and limited quartz (average Q-F-L % = 10.4-69.8-19.8; Table 3, and Figure 17 QFL ternary). Feldspar is the most common mineral within Soledad Rojo formation sandstones, with plagioclase in greater abundance than potassium feldspar (average Q-K-P%= 13-16-71; Table 3, and Figure 17 QKP ternary). Feldspars are abundant in comparison to the presence of monocrystalline quartz and the total lithic fragments (average Qm-F-Lt%= 5-70-25; Table 3, and Figure 17 QmFLt ternary).

	Stratigraphic	Location		Q-F-L %			Qm-F-Lt %			Q-K-P %			Lm-Lv-Ls %		
Sample	Unit	Northig	Easting	Q	F	L	Qm	F	Lt	Q	K	P	Lm	Lv	Ls
A1	Tsrl	3698315	694779	11.3	87.3	1.4	1.6	96.9	1.6	11.5	15.8	72.7	100.0	0.0	0.0
A2	Tsrl	3698319	694777	12.8	62.6	24.6	5.3	68.0	26.7	16.9	14.1	69.0	19.8	80.2	0.0
A3	Tsrl	3698320	694789	9.3	80.2	10.5	4.2	84.7	11.1	10.4	14.9	74.7	37.8	62.2	0.0
A4	Tsrl	3698339	694807	8.2	78.0	13.8	3.0	82.4	14.6	9.5	9.5	81.0	20.4	79.6	0.0
A5	Tsrl	3698337	694834	4.1	90.3	5.6	1.0	93.2	5.8	4.3	12.0	83.7	16.7	83.3	0.0
A6	Tsrm	3698344	694860	5.5	66.5	28.0	1.2	69.5	29.3	7.7	7.3	85.0	4.2	95.8	0.0
A7	Tsrm	3698348	694861	3.7	68.1	28.3	1.1	69.9	29.0	5.1	8.4	86.5	3.7	96.3	0.0
A8	Tsrm	3968342	694919	3.1	81.3	15.6	0.3	83.6	16.1	3.7	21.2	75.1	1.8	98.2	0.0
S1.1	Tsrl	3697130	694595	5.3	31.5	63.2	1.2	32.8	66.0	14.5	16.0	69.5	1.8	98.2	0.0
S1.3	Tsrm	3696165	692975	15.0	44.8	40.2	11.8	46.5	41.7	25.1	25.1	49.8	28.3	71.7	0.0
S1.4	Tsrm	3695069	693068	27.5	46.3	26.2	21.0	50.5	28.5	37.3	27.0	35.8	73.5	26.5	0.0

Table 3: This table shows the sample's stratigraphic unit, location, and recalculated parameters that was taken from the thin section point-counting analysis raw data shown in Table 2. These data were used to generate the QFL, QmFLt, QKP, and LmLvLs ternary diagrams.

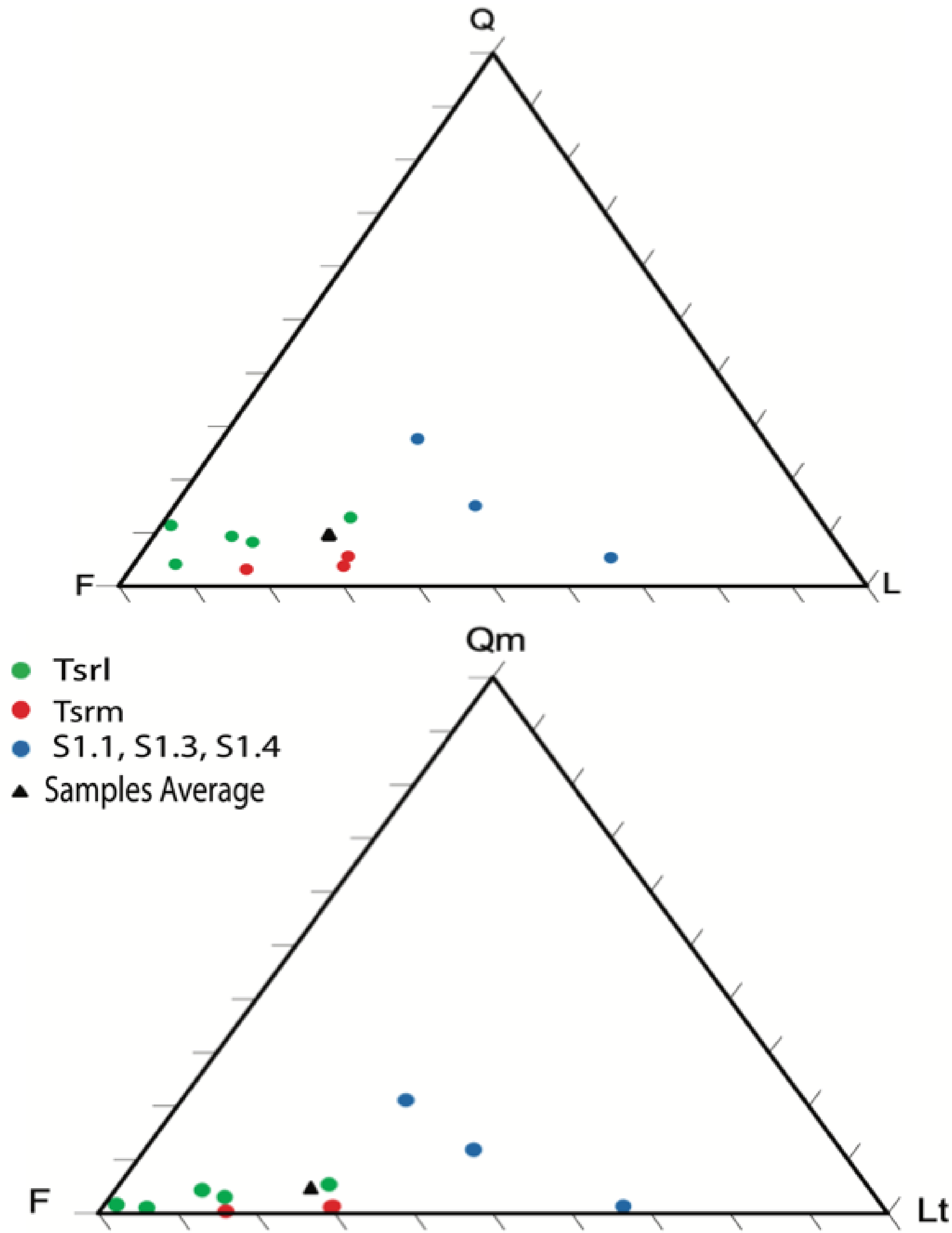
Q
F
L
Qm
Tsrl
Tsrm
S1.1, S1.3, S1.4
Samples Average
F
Lt

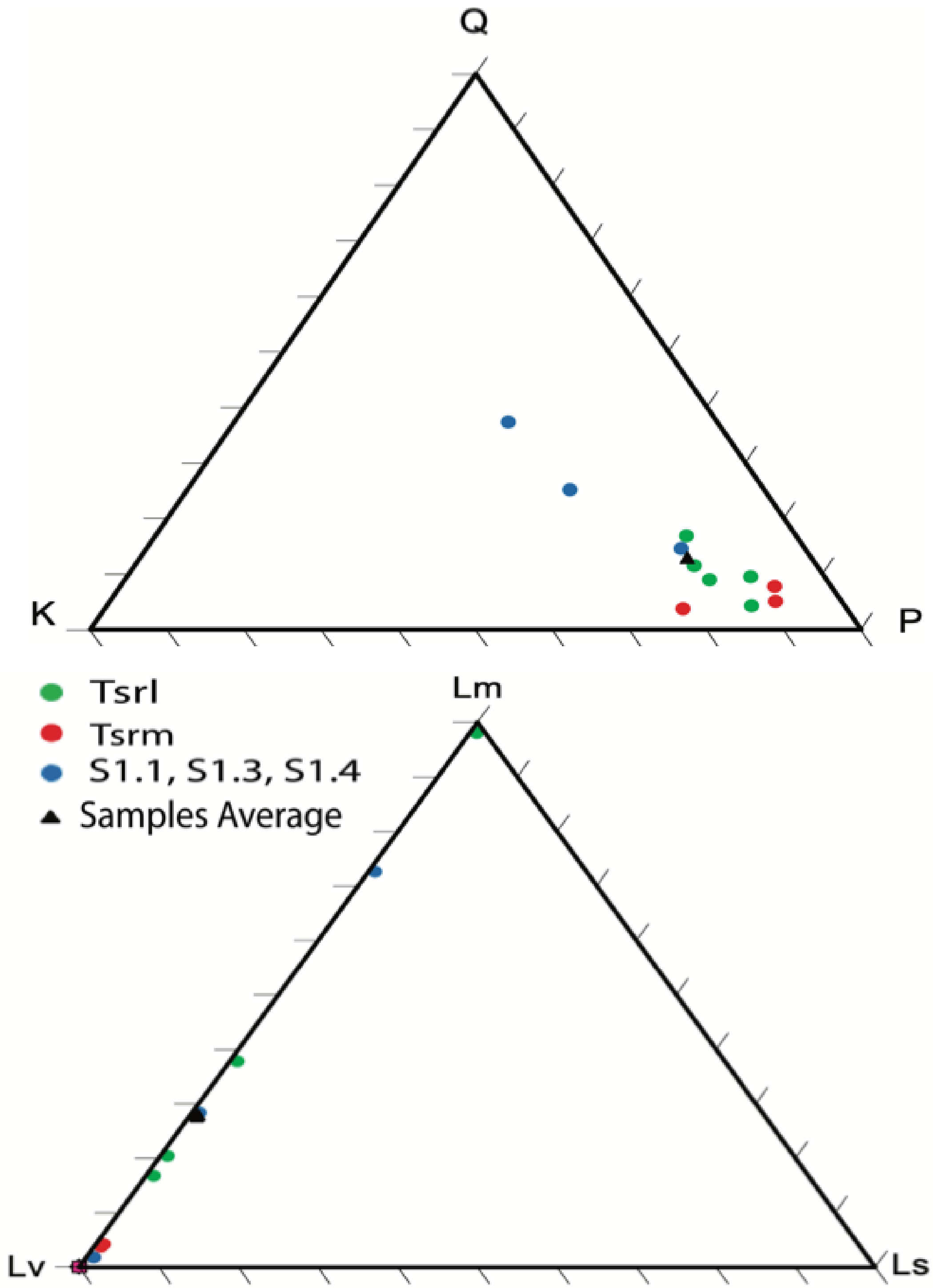
Q
K
P
Tsrl
Tsrm
S1.1, S1.3, S1.4
Samples Average
Lm
Lv
Ls

Figure 17 (previous two pages): Ternary diagrams showing the results of the thin section point-counting analyses. QFL: quartz-feldspar-lithic fragments, QmFLt: monocrystalline quartz-feldspar-total lithic fragments, QKP: quartz-potassium feldspar-plagioclase, and LmLvLs: metamorphic lithic fragments-volcanic lithic fragments-sedimentary lithic fragments. Lower (Tsrl), middle (Tsrm), and S1.1-S1.4 samples of the Soledad Rojo formation are represented by green, red, blue circles, respectively. The average composition of all analyzed samples is shown with a black triangle symbol. See Table 1 for point counting parameters and Tables 2 and 3 for results of point-counting analyses.

3.3 DETRITAL ZIRCON U-Pb DATING RESULTS

Relative probability density curves, and histograms for the four sandstone samples collected from the Soledad Rojo formation for detrital zircon U-Pb analysis are shown in Figure 18. Samples A8 and A2 were collected from the middle and lower units, respectively, of the formation from the Tadpole Tank measured section in the northern part of the basin (Figures 6 and 8). Samples Tcgs and Tccg were also collected from the middle and lower units, respectively, of the formation in the southern part of the basin (Figure 6). Relative probability density curves help determine the maximum deposition age of the Soledad Rojo formation and other major age peaks in the sediment source of the Soledad Rojo formation. Raw data and Concordia diagrams were made by Chemostrat Ltd Lab (2018) and are shown in Appendices A and B, respectively.

The results of the detrital zircon dating show five groups of different age within the Soledad Rojo formation (Figure 18). Several age peaks are found within the samples, indicating derivation from late Oligocene (ca. 25 Ma), late Cretaceous (ca. 75 Ma), late Jurassic (ca. 153 Ma), and Proterozoic (ca. 1.2 Ga and ca. 1.7 Ga) sources. However, there are slight differences between the samples collected from the two different units of the formation: samples from the lower unit (A2 and Tccg) indicate an additional early to late Cretaceous source (ca. 88 and ca. 112 Ma), while samples from the middle unit (A8 and Tcgs) indicate a separate Neoproterozoic source. However, given the limited number of zircon grains from each of these two age groups (Figure 18), the differences between the lower and middle units could just be an artifact of undercoverage sampling bias rather than a difference in sediment sources.

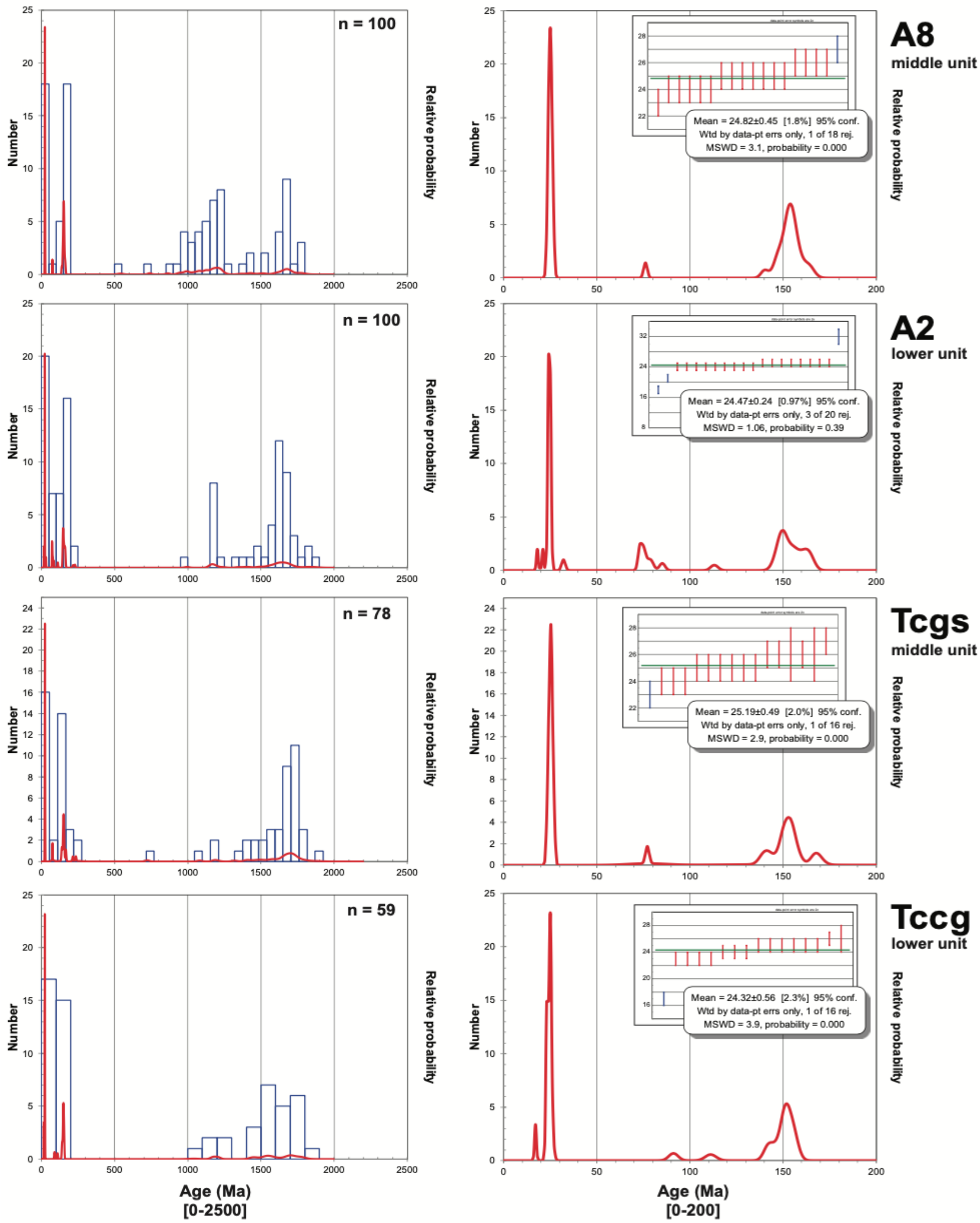

Figure 18 (previous page): Relative probability density curves and histograms for four detrital zircon U-Pb samples collected from the Soledad Rojo formation (see Figures 6 and 8 for sample locations). The graphs in the left column show the age distribution from 0-2500 Ma; the right column shows the same data from 0-200 Ma to highlight the Mesozoic-Cenozoic age peaks. Inset on the right column are weighted average plots of the youngest zircon population for each sample to indicate the maximum depositional age, which is ca. 24.5 Ma for all samples. Raw data and Concordia diagrams made by Chemostrat Ltd Lab (2018) are shown in Appendices A and B, respectively.

CHAPTER 4 – INTERPRETATION AND DISCUSSION

The isometric diagram of the regional seismic profiles (Figure 4) gives an idea of the nature of the study area faults that formed as a result of the regional extension during the mid-Tertiary period. Several medium to high angle normal faults are present in the study area basin, which is likely an asymmetric graben or half-graben basin with most slip on the eastern basin bounding fault. The faults that mark the basin boundaries are most probably the ones marked in blue in Figure 4, where a change in fault dip directions is indicated in the seismic profile. Sedimentary facies within the Soledad Rojo formation suggests that the formation is an alluvial fan/braided fluvial system deposits. So, the Soledad Rojo formation represents a synextensional alluvial fan/braided fluvial system deposited in a half-graben or asymmetric graben basin that developed during regional mid-Tertiary extension. Growth strata shown in Figure 16 supports this hypothesis as well.

The average composition of sandstones from the Soledad Rojo formation show that the Qm-F-Lt percentages plot within the feldspar-dominated “basement uplift” tectonic provenance setting of Dickinson (1985), which is caused when fault-bounded basement uplifts along rift shoulders or transform ruptures uplift metaplutonic rocks to the surface. This tectonic setting determined by sandstone composition is consistent with presence of uplifted metaplutonic basement rocks in the region near the study area, with the quartzofeldspathic sediments derived from these rocks transported and deposited in the Soledad Rojo formation basin. It should be noted, however, that the sedimentary facies associated with the Soledad Rojo formation suggest a first to second order sand sampling (e.g., alluvial fans and braided fluvial system sourced from individual rock types and/or mountain ranges), which is not ideal for tectonic provenance determinations using the

Dickinson ternary diagram classifications that work best for third order sampling (big rivers and their deltas, marine environments) (Ingersoll et al.,1993).

QKP ternary diagram (Figure 17) shows that more than 70 percent of the feldspars within the Soledad Rojo formation are plagioclase feldspars. Most of the plagioclase feldspars show no sign of zoning, suggesting that most of them are from metamorphic sources (Helmold, 1985). Also, most of the plagioclase feldspar grains are untwinned rather than twinned, suggesting the abundance of more metamorphic-derived plagioclase feldspars than volcanic/plutonic plagioclase feldspars; however, it’s possible the untwinned grains could be a result of breakage of twinnings during sediment transport (Helmold, 1985). The abundance of plagioclase also suggests an uplifted basement provenance (Helmold, 1985). Most of the potassium feldspars show cross-hatch twinning, indicative of microcline, which is typically derived from metamorphic and plutonic sources (Helmold, 1985).,

The abundance of plagioclase and trace olivine supports our interpretations that the Soledad Rojo formation is likely derived, in part, from local basaltic volcanic and metamorphic rocks surrounding the study area. Most of the igneous rock fragments within the Soledad Rojo formation look relatively fresh, suggesting that they had little transport after they were eroded from the original source. Olivine is usually found within basic and ultrabasic igneous rocks and has a relatively low weathering stability (Adams et al., 2017; MacKenzie et al., 2017), suggesting that the source of these fragments could be from the adjacent volcanic-dominated mountains in the region. Based on this study, the sources of sediment to the Soledad Rojo formation is likely a combination derived from the Mesozoic plutonic rocks within Mule Mountains, Mesozoic metaplutonic and the Quechan volcanic rocks found within the Palo Verde Mountains and Black Hills, mid-Tertiary volcanic rocks within Chocolate Mountains, and the silicic tuff sequence (tuff of Felipe Pass, tuff of Black Hills, tuff of ten Ewe Mountain, and the ignimbrite of Ferguson Wash) that are spread almost across the whole region of the study area vicinity including: Kofa, Castle Dome, and Little Chuckwalla Mountains (Figures 2 and 3).

Detrital zircon dating suggest that Soledad Rojo formation sediments were potentially derived from late Mesozoic and Proterozoic metaplutonic basement rocks exposed in the region adjacent to the basin. The results of the detrital zircon dating show four groups of different age within the Soledad Rojo formation. They were deposited during the late Cretaceous (ca. 75 Ma), late Jurassic (ca. 153 Ma), and Proterozoic (ca. 1.2 Ga and ca. 1.7 Ga). The Proterozoic detritus could have been sourced from the augen gneiss (1.7 Ga) found in Chocolate and Little Chuckwalla Mountains; anorthosite and syenite in Chocolate Mountains region have an age of 1.2 Ga; and the Pinal Schist in Mule Mountains which is dated to pre-Paleozoic (Dillon, 1976; Hamilton, 1982; Silver, 1989; Hoyt, 2012). The late Jurassic detritus could have been sourced from the Mesozoic gneiss and granitic rocks found within Palo Verde, Mule, Chocolate, Trigo, and Castle Dome Mountains (Haxel et al., 2002; Chapman, 2016). The late Cretaceous detritus could have been sourced source could be from the Orocopia schist found within the study area region like Chocolate, Trigo, and Castle Dome Mountains. They have a maximum depositional age between 67.1 and 84.5 Ma (Barth et al., 2003; Grove et al., 2003, 2008; Jacobson et al., 2011; Chapman et al., 2013; Chapman et al., 2016; Dumitru et al., 2016; Chapman, 2016).

The Soledad Rojo formation was tentatively correlated to the Tolbard Fanglomerate of the Midway Mountains (Figure 2) by previous authors, as they share similarities in terms of rock description and composition (e.g., Elliott and Marshall, 2012). For example, the Tolbard Fanglomerate is a reddish brown, well indurated alluvial deposit interbedded with debris flows. Both rock units contain clasts of andesite, gneiss, dacite, and metasedimentary rocks. Similar to the Soledad Rojo formation, the Tolbard Fanglomerate also contains coarse to very coarse arkosic sandstones. However, the age of the Tolbard Fanglomerate is suggested to be in the Miocene epoch, while our detrital zircon data shows a maximum deposition age of 24-25 Ma for the Soledad Rojo formation, within the late Oligocene epoch. In addition, these formations are separated by distance of around 18 miles (Jorgensen et al., 1982). The difference in age and the large distance between the Soledad Rojo formation and Tolbard Fanglomerate strongly suggests that they are not correlative stratigraphic units.

Elliott and Marshall (2012) interpreted that the Soledad Rojo formation is an extension of the Colorado River Delta deposits. The Colorado River Delta can be shown to contain detrital zircons sourced from at least five distinct drainage basins: the Green, Grand, San Juan, Little Colorado, and Gila river systems. A comparison of the detrital zircon age data proves that the Soledad Rojo formation has a different source than the Colorado River Delta deposits. The difference in the age peaks supports the idea that the sediment sources are distinct (Figure 19). There are several age peaks within the Colorado River Delta deposits that are absent in the Soledad Rojo formation marked by purple lines. These Age peaks differences around 100 Ma, 200 Ma, 300 Ma, 400 Ma, 600 Ma, 1.1 Ga, 1.43 Ga, and 1.81 Ga. Only few age peaks in the Colorado River Delta deposits matches some age peaks in the Soledad Rojo formation marked by green lines in Figure 19. This could mean that they share few similar sources, but that does not mean they are the same formation (Kimbrough et al., 2010).

Figure 19: This figure compare the age peaks of the Soledad Rojo formation (Green lines) and the Colorado River deposits (Purple lines). Modified after (Kimbrough et al., 2010).

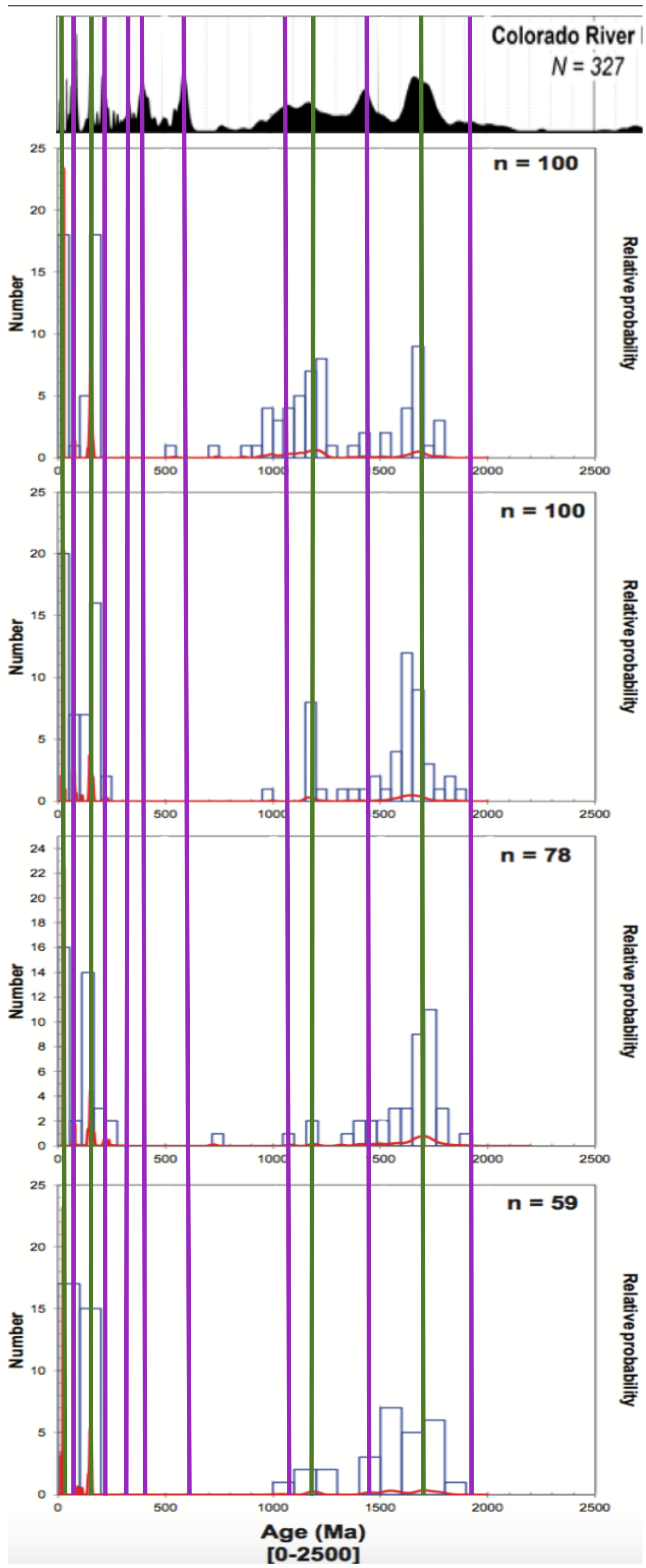

Although the detrital zircon ages and sedimentary lithofacies of the Soledad Rojo formation suggest a local metaplutonic sediment source, an alternative hypothesis is that the detrital zircon sediments came from metaplutonic rocks found in the San Gabriel Mountains region. The palinspastic reconstruction model of the eastern and central San Gabriel Mountains along the San Andreas fault system shows a 160 km restoration of right-lateral tectonic movement (Nourse, 2002). The middle Miocene palinspastic reconstruction of the San Gabriel Mountains along the San Andreas fault system is shown in Figure 20, showing that the rocks of the San Gabriel Mountains that are currently located ~300 km west of the study area were found just south of the Soledad Rojo basin/Chocolate Mountain during the time of basin deposition (Nourse, 2002). This model shows that rocks from different ages from the San Gabriel Mountains could fit the Soledad Rojo formation's detrial zircon age groups. The Proterozoic age group could be the granite augen gneiss and/or the banded gneiss (mapped as San Gabriel-type PC-Mz basement); the late Jurassic age group could be the Pelona/Orocopia schist (mapped as Pelona / Orocopia / Chocolate Mountains schist); the late Cretaceous could be quartz diorite, tonalite, granodiorite, and granite (mapped as Cretaceous Peninsular ranges batholith and wall-rocks); and the late Oligocene age group could be the Telegraph Peak granite or Mountains Meadows dacite (Mapped Late Oligocene Telegraph Peak Granite / Mountains Meadows Dacite) (Figure 20; Nourse, 2002). The palinspastic reconstruction of the San Gabriel Mountains along the San Andreas fault system provides a valid alternative explanation for the source of Mesozoic-Proterozoic-age sediments and how they reached the research region; the sediments of Soledad Rojo were possibly derived in part from the San Gabriel Mountains and transported to the basin as a result of a braided fluvial system before the sediment source was shifted to its current location due to right-lateral transform plate tectonic movements.

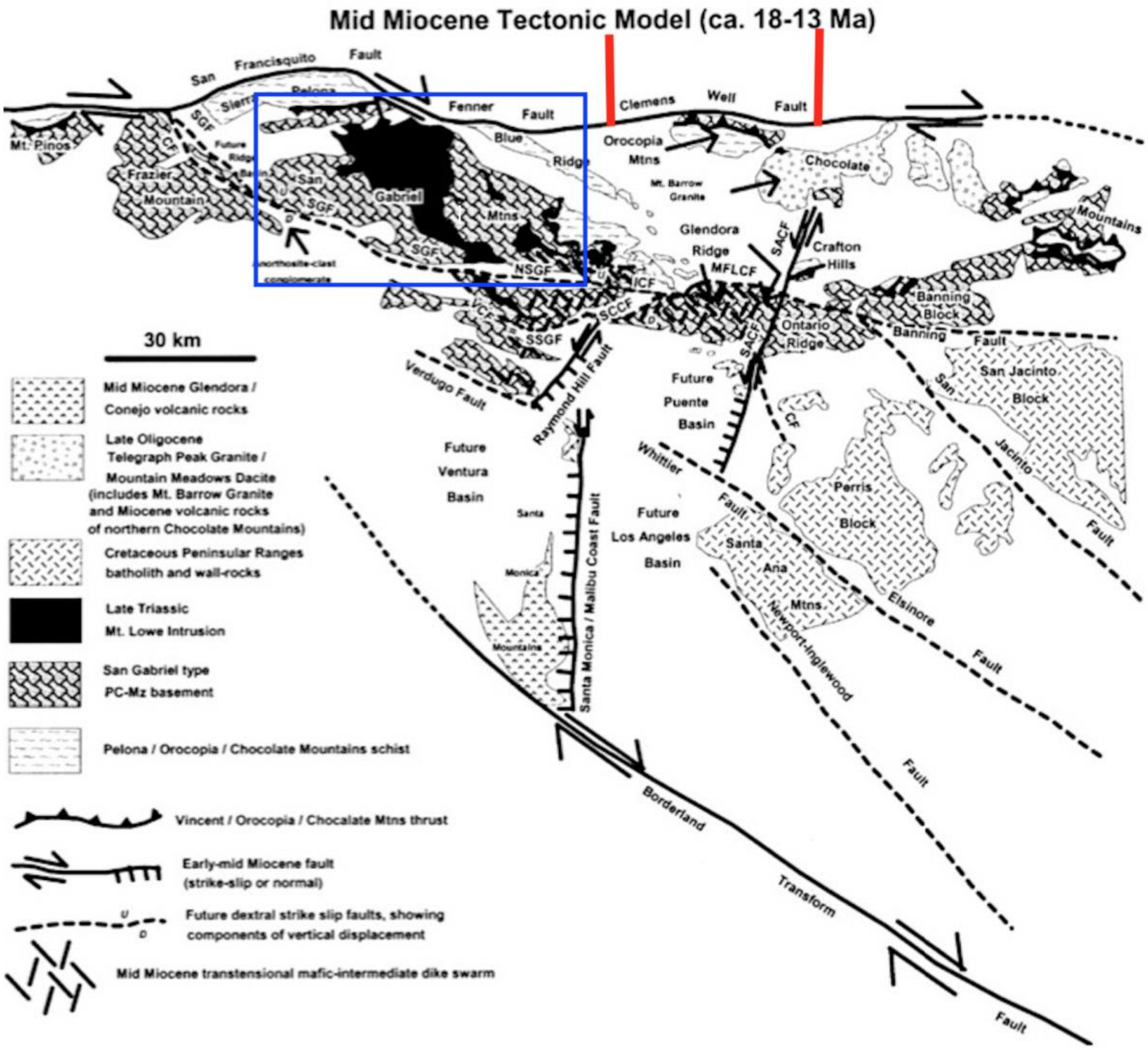

Figure 20: Paleogeography of Southern California (middle Miocene) presenting the Frazier and San Gabriel Mountains restored to be near to the Chocolate and Orocopia Mountains. The location of the San Gabriel Mountains is marked by the blue box. Range of possible deposition location of the Soledad Rojo formation is marked by the red lines. Fault Abbreviations: CF—Canton fault, NSGF—north branch San Gabriel fault, SSGF—south branch San Gabriel fault, VCF—Vasquez Creek fault (Nourse, 2002).

CHAPTER 5 – CONCLUSIONS AND FUTURE WORK

5.1 CONCLUSIONS

The Soledad Rojo formation represents a synextensional alluvial fan/braided fluvial system deposited in an asymmetric graben or half-graben basin that developed during regional mid-Tertiary extension. Point counting results show an abundance of plagioclase and trace olivine which supports our interpretations that the Soledad Rojo formation is likely derived from local basaltic volcanic and metamorphic rocks. The results of the detrital zircon dating show five groups of different age within the Soledad Rojo formation: the late Cretaceous (ca. 75 Ma), late Jurassic (ca. 153 Ma), and Proterozoic (ca. 1.2 Ga and ca. 1.7 Ga). This suggests that Soledad Rojo formation sediments were potentially derived from late Mesozoic and Proterozoic metaplutonic basement rocks exposed in the region adjacent to the basin. The Soledad Rojo formation was correlated to the Tolbard Fanglomerate of the Midway Mountains; however, this claim is unlikely because the Miocene age of the Tolbard Fanglomerate is younger than our detrital zircon data that suggests a late Oligocene maximum deposition age for the Soledad Rojo formation. The Soledad Rojo formation was also suggested to be an extension of the Colorado River Delta deposits; however, there are several age peaks within the Colorado River Delta deposits that are absent in the Soledad Rojo formation, which suggest that they are not the same formation. An alternative hypothesis is that the detrital zircon sediments came from San Gabriel Mountains region. The palinspastic reconstruction model provides a valid alternative explanation on the source of the Mesozoic-Proterozoic derived sediments in the Soledad Rojo formation.

5.2 FUTURE WORK

There is an opportunity in the future for more work to further study the Soledad Rojo formation. Expanding the geologic map would help in developing a better idea on how the formation is changing across the region. More samples would be found and will definitely add a lot of information to this research. Another thing that would be really helpful is probably generating more seismic profiles to better understand the structural geology of the region as it would accurately define the faults' location. It would really be helpful if these profiles are joint with the exiting profiles found in Morris (1993) paper. More dating is also preferable to see if any new potential source is found as well as confirming the current maximum depositional age of 24-25 Ma. It would also result in having a more complete spectrum of detrital age. Additional lab analysis on the newly collected samples including thin-section point counting would also help to monitor any changes in composition away from the current research location.

References

Adams, A. E., MacKenzie, W. S., & Guilford, C. (2017). *Atlas of Sedimentary Rocks Under the Microscope*. Routledge.

Axen, G. J., Taylor, W. J., & Bartley, J. M. (1993). Space-time patterns and tectonic controls of tertiary extension and magmatism in the Great basin of the western United States. *Geological Society of America Bulletin, 105*(1), 56-76. doi:10.1130/0016-7606(1993)1052.3.co;2

Bagby, W., Haxel, G., Smith, D., Koch, R., Grubensky, M., Sherrod, D., & Pickthorn, L. (1987). Mineral resource assessment of the Kofa National Wildlife Refuge, Arizona. *Open-File Report*. doi:10.3133/ofr87609

Barth, A. P., Wooden, J. L., Grove, M., Jacobson, C. E., & Pedrick, J. N. (2003). U-Pb zircon geochronology of rocks in the Salinas Valley region of California: A reevaluation of the Crustal structure and origin of the Salinan block. *Geology, 31*(6), 517. doi:10.1130/0091-7613(2003)0312.0.co;2

Belousova, E., Griffin, W., O'Reilly, S. Y., & Fisher, N. (2002). Igneous zircon: Trace element composition as an indicator of source rock type. *Contributions to Mineralogy and Petrology, 143*(5), 602-622. doi:10.1007/s00410-002-0364-7

Berg, L., Leveille, G., and Geis, P., 1982, Mid-Tertiary detachment faulting and manganese mineralization in the Midway Mountains, Imperial County, California: in Anderson-Hamilton volume, Mesozoic-Cenozoic Tectonic Evolution of the

Colorado River Region, California, Arizona, and Nevada: Eric Frost and Donna Martin (eds.), p. 298- 311.

Blair, T., & McPherson, J. (1994). Alluvial fans and their natural distinction from Rivers based ON Morphology, Hydraulic Processes, SEDIMENTARY processes, AND Facies Assemblages. *SEPM Journal of Sedimentary Research, Vol. 64A.* doi:10.1306/d4267dde-2b26-11d7-8648000102c1865d

Bradley, C. M., & Colonder, D. (2020). The Sonoran Desert. In the Encyclopedia of the World's Biomes (pp.110-125). Elsevier. https://doi.org/10.1016/b978-0-12-409548-9.11939-6

Bradshaw, T., Hawkesworth, C., & Gallagher, K. (1993). Basaltic volcanism in the Southern Basin and Range: No role for a mantle plume. *Earth and Planetary Science Letters, 116*(1-4), 45-62. doi:10.1016/0012-821x(93)90044-a

Carl E. Jacobson, Marty Grove, Matthew M. Stamp, Ana Vucic, Felix R. Oyarzabal, Gordon B. Haxel, Richard M. Tosdal, David R. Sherrod, 2002. "Exhumation history of the Orocopia Schist and related rocks in the Gavilan Hills area of southeasternmost California", Contributions to Crustal Evolution of the Southwestern United States, pp.129-154

Chapman, A. D. (2016). The Pelona–Orocopia–Rand and related schists of southern California: A review of the best-known archive of shallow subduction on the planet. *International Geology Review, 59*(5-6), 664-701. doi:10.1080/00206814.2016.1230836

Chapman, A. D., Jacobson, C. E., Ernst, W., Grove, M., Dumitru, T., Hourigan, J., & Ducea, M. N. (2016). Assembling the WORLD'S type shallow Subduction complex: Detrital ZIRCON geochronologic constraints on the origin of the Nacimiento block, central California Coast Ranges. *Geosphere, 12*(2), 533-557. doi:10.1130/ges01257.1

Chapman, A. D., Saleeby, J. B., & Eiler, J. (2013). Slab flattening trigger for isotopic disturbance and MAGMATIC flare-up in the SOUTHERNMOST Sierra Nevada BATHOLITH, CALIFORNIA. *Geology, 41*(9), 1007-1010. doi:10.1130/g34445.1

Cockerell, T. D. (1945). The Colorado desert of California: Its origin and Biota. *Transactions of the Kansas Academy of Science (1903-), 48*(1), 1. doi:10.2307/3625030

Conde, C. K. (1982). Plate tectonics & CRUSTAL EVOLUTION. *New York, Pergamon Press*. doi:10.1016/c2013-0-00713-x

Crossey, L., Karlstrom, K., Crow, R., House, P., Pearthree, P. (2016). Travertines of THE Bouse Formation. Retrieved April 8, 2021, from https://pages.uoregon.edu/rdorsey/Downloads/CrosseyEtal2016DS.pdf

CROWE, B. M. (1978). Cenozoic volcanic geology and PROBABLE age of inception of basin-range faulting in the Southeasternmost Chocolate Mountains, California. *Geological Society of America Bulletin, 89*(2), 251. doi:10.1130/0016-7606(1978)892.0.co;2

Dickinson, W. R. (1985). Interpreting provenance relations FROM Detrital modes of sandstones. *Provenance of Arenites*, 333-361. doi:10.1007/978-94-017-2809-6_15

Dickinson, W. R., & Wernicke, B. P. (1997). Reconciliation of San Andreas slip discrepancy by a combination of INTERIOR Basin and range extension and transrotation near the coast. *Geology*, *25*(7), 663. doi:10.1130/0091-7613(1997)0252.3.co;2

Dillon, J.T., 1976, Geology of the Chocolate and Cargo Muchacho Mountains, southeasternmost California [Ph.D. Dissertation]: University of California, Santa Barbara, 380p.

Dumitru, T. A., Elder, W. P., Hourigan, J. K., Chapman, A. D., Graham, S. A., & Wakabayashi, J. (2016). Four Cordilleran Paleorivers that Connected Sevier thrust zones in Idaho to Depocenters in California, Washington, WYOMING, and, indirectly, Alaska. *Geology*, *44*(1), 75-78. doi:10.1130/g37286.1

Eaton, G. P. (1982). The basin and range Province: Origin and Tectonic significance. *Annual Review of Earth and Planetary Sciences, 10*(1), 409-440. doi:10.1146/annurev.ea.10.050182.002205

Eberly, L. D., & Stanley, T. B. (1978). Cenozoic stratigraphy and geologic history of southwestern Arizona. *Geological Society of America Bulletin, 89*(6), 921. doi:10.1130/0016-7606(1978)892.0.co;2

Ehlig, P.L., 1981, Origin and tectonic history of the basement terrane of the San Gabriel Mountains, central Transverse Ranges, in Ernst, W.F., ed., The Geotectonic Development of California (Rubey Volume I): Englewood Cliffs, New Jersey, Prentice- Hall, p. 253-283.

Elliott, W. J., & Marshall, M. (2012) In search of Colorado River "B" gravel Northeastern Imperial County, California. *Picacho and the Cargo Muchachos: Gold, Guns, and Geology of Eastern Imperial County, California*. Editor: Todd A. Wirths. San Diego Association of Geologists.

Ferrari, L., Valencia-Moreno, M., & Bryan, S. (2007). Magmatism and tectonics of the Sierra Madre Occidental and its relation with the evolution of the western margin of North America. *Geology of México: Celebrating the Centenary of the Geological Society of México*. doi:10.1130/2007.2422(01)

Foster, D. A., & John, B. E. (1999). Quantifying tectonic exhumation in an extensional orogen with thermochronology: Examples from the southern basin and range province. *Geological Society, London, Special Publications, 154*(1), 343-364. doi:10.1144/gsl.sp.1999.154.01.16

Frost, E. G., Fattahipour, M. J., & Robinson, K. L. (1996). NEOGENE detachment AND Strike-slip faulting in The SALTON TROUGH region and their geometric and GENETIC INTERRELATIONSHIPS. *Field Conference Guide, AAPG National Convention, San Diego, California*. doi:10.32375/1996-gb73.13

Gardner, K. (2020, February 27). University of OREGON Libraries. Retrieved April 08, 2021, from https://scholarsbank.uoregon.edu/xmlui/handle/1794/25251

Gilluly, J. (1956). General geology of central Cochise COUNTY, Arizona, with sections on age and correlation. *Geol. Survey Prof. Paper 281*. doi:10.3133/pp281

Grove, M., Bebout, G., Jacobson, C., Barth, A., Kimbrough, D., King, R., . . . Gehrels, G. (2008). The Catalina Schist: Evidence for middle Cretaceous SUBDUCTION erosion of southwestern North America. *Special Paper 436: Formation and Applications of the Sedimentary Record in Arc Collision Zones*, 335-361. doi:10.1130/2008.2436(15)

Grove, M., Jacobson, C. E., Barth, A. P., & Vucic, A. (2003). Temporal and spatial trends of Late Cretaceous-early Tertiary UNDERPLATING Pelona and related Schist beneath southern California and southwestern Arizona. *Tectonic Evolution of Northwestern Mexico and the Southwestern USA*. doi:10.1130/0-8137-2374-4.381

Grubensky, M. J., & Bagby, W. C. (1990). Miocene CALC-ALKALINE magmatism, calderas, and crustal extension in the Kofa and Castle Dome MOUNTAINS, southwestern Arizona. *Journal of Geophysical Research, 95*(B12), 19989. doi:10.1029/jb095ib12p19989

Grubensky, M., Haxel, G., & Koch, R. (1993). Geologic map of the Castle Dome Mountains, southwestern Arizona. *USGS Numbered Series*. doi:10.3133/i2138

Hamilton, W.B., 1982, Structural evolution of the Big Maria Mountains, northeastern Riverside County, southeastern California, in Frost, E.G., and Martin, D.L., eds., Mesozoic-Cenozoic tectonic evolution of the Colorado River region, California, Arizona, and Nevada - Anderson-Hamilton Volume: San Diego, Cordilleran Publishers, p. 1-27.

Han, L., Hole, J. A., Stock, J. M., Fuis, G. S., Kell, A., Driscoll, N. W., . . . Lázaro-Mancilla, O. (2016). Continental rupture and the creation of new crust in the Salton trough rift, Southern California and northern Mexico: Results from the SALTON seismic Imaging Project. *Journal of Geophysical Research: Solid Earth, 121*(10), 7469-7489. doi:10.1002/2016jb013139

Haxel, G. B., Jacobson, C. E., Richard, S. M., Tosdal, R. M., & Grubensky, M. J. (2002). The Orocopia SCHIST in southwest Arizona: Early Tertiary OCEANIC rocks trapped or transported far inland. *Contributions to Crustal Evolution of the Southwestern United States*. doi:10.1130/0-8137-2365-5.99

Haxel, G., Dillon, J., & Tosdal, R. (1985). Tectonic setting and lithology of the Winterhaven Formation; a New Mesozoic stratigraphic unit in southeasternmost California and southwestern Arizona. *U.S. Geological Survey Bulletin*. doi:10.3133/b1599

Haxel, G.B., and Dillon, J.T., 1978, The Pelona-Orocopia Schist and Vincent-Chocolate Mountain thrust system, southern California, in Howell, D.G., and McDougall, K.A., eds., Mesozoic Paleogeography of the western United States - Pacific Coast

Paleogeography Symposium 2, Los Angeles, Calif., 1978: Society of Economic Paleontologists and Mineralogists, Pacific Section, Los Angeles, Calif., p. 453-469.

Hayes, P., & Landis, E. (1965). Paleozoic stratigraphy of the southern part of the Mule mountains, Arizona. *Contribution to General Geology*. doi:10.3133/b1201f

Helmold, K. P. (1985). Provenance of feldspathic SANDSTONES — the effect of Diagenesis on Provenance Interpretations: A review. *Provenance of Arenites,* 139-163. doi:10.1007/978-94-017-2809-6_7

Henry, C. D., & Aranda-Gomez, J. J. (1992). The real southern Basin and RANGE: Mid-to late Cenozoic extension in Mexico. *Geology, 20*(8), 701. doi:10.1130/0091-7613(1992)0202.3.co;2

Hildebrand, R. S., & Whalen, J. B. (n.d.). The tectonic setting and origin of Cretaceous Batholiths within the North AMERICAN CORDILLERA: The case for Slab Failure MAGMATISM and its significance for Crustal growth. *The Tectonic Setting and Origin of Cretaceous Batholiths within the North American Cordillera The Case for Slab Failure Magmatism and Its Significance for Crustal Growth*. doi:10.1130/2017.2532

Hoyt, J. (2012). Provenance and Detrital-Zircon Studies of the Mint Canyon Formation and its Correlation to the Caliente Formation, Southern California. *UCLA*. ProQuest ID: Hoyt_ucla_0031N_10371. Merritt ID: ark:/13030/m56h4jxn. Retrieved from https://escholarship.org/uc/item/9480574s

Ingersoll, R. V., & Rumelhart, P. E. (1999). Three-stage evolution of the Los Angeles basin, southern California. *Geology*, *27*(7), 593. doi:10.1130/0091-7613(1999)0272.3.co;2

Ingersoll, R. V., Kretchmer, A. G., & Valles, P. K. (1993). The effect of sampling scale on actualistic sandstone petrofacies. *Sedimentology*, *40*(5), 937-953. doi:10.1111/j.1365-3091.1993.tb01370.x

Jacobson, C. E. (1990). The40Ar/39Ar Geochronology of THE Pelona schist and related rocks, southern California. *Journal of Geophysical Research*, *95*(B1), 509. doi:10.1029/jb095ib01p00509

Jacobson, C. E., Grove, M., Pedrick, J. N., Barth, A. P., Marsaglia, K. M., Gehrels, G. E., & Nourse, J. A. (2011). Late Cretaceous-early CENOZOIC tectonic evolution of the southern CALIFORNIA margin inferred from provenance of trench and FOREARC SEDIMENTS. *Geological Society of America Bulletin*, *123*(3-4), 485-506. doi:10.1130/b30238.1

John, B. E., & Foster, D. A. (1993). Structural and thermal constraints on the initiation angle of detachment faulting in the southern basin and range: The Chemehuevi mountains case study. *Geological Society of America Bulletin*, *105*(8), 1091-1108. doi:10.1130/0016-7606(1993)1052.3.co;2

Johnson, C., and Miller, D.G., 1980, Late Cenozoic alluvial history of the lower Colorado River, in Fife, D.L., and Brown, A.R., eds., Geology and mineral wealth of the

California desert - Dibblee Volume: South Coast Geological Society (Santa Ana, Calif.), p. 441-446.

Jorgensen, M., Natenstedt, C., Trumbly, P. (1982). Possible Relationship Between Miocene Crustal Extension/ Detachment Faulting in The Midway and Western Palo Verde Mountains, Imperial County, California. Department of Geological Sciences, San Diego State University.

Kimbrough, D., Grove, M., Gehrels, G., Mahoney, B., Dorsey, R., Howard, K., House, K., Peartree, P., Flessa, K. (2010). Detrital Zircon Record of Colorado River Integration into the Salton Tough. U.S. *Geological Survey*. 168-174.

Landforms of the Basin and range Province: Defined for SOIL SURVEY. (n.d.). Retrieved April 08, 2021, from https://www.resolutionmineeis.us/documents/peterson-1981

Ludwag, K. (2000). User's manual FOR isoplot/ex: A geochronological toolkit for Microsoft Excel. Retrieved April 8, 2021, from https://www.researchgate.net/publication/245539605_Users_manual_for_IsoplotEx_a_geochronological_toolkit_for_Microsoft_Excel

MacKenzie, W. S., Adams, A. E., & Brodie, K. H. (2017). *Rocks and minerals in thin section*. Boca Raton: CRC Press.

Macleod, E. A. (n.d.). USING LIDAR to map the geology and morphology of ALLUVIAL FANS: SALTON Sea AREA, CALIFORNIA. doi:10.37099/mtu.dc.etdr/355

Mange, M. A., & Maurer, H. F. W. (1992). Heavy minerals in colour (pp. 147). London: Chapman and Hall. 39-133. doi:10.1007/978-94-011-2308-2_7

Metzger, D., 1968. The Bouse Formation (Pliocene) of the Parker-Blythe-Cibola area, Arizona and California, IN Geological Survey Research 1968: U.S. Geological Survey Professional Paper, 600-d, p. D126-D136.

Miall, A. D. (1985). Architectural-element analysis: A new method of facies analysis applied to fluvial deposits. *Recognition of Fluvial Depositional Systems and Their Resource Potential,* 33-81. doi:10.2110/scn.85.19.0033

Morris, Rebecca S., 1993, Tertiary Basin Structure Revealed in Seismic Reflection Profiles from Milpitas Wash, Southeastern Calif.: USGS Bulletin 2053, p. 217- 221.

Murray, B., House, B., Al-Kaabi, A., Hames, W. (2019). New Geochronology and Stratigraphic Interpretations of the Mid-Tertiary Soledad Rojo Formation in the Lower Colorado River Extensional Corridor, Western Palo Verde Mountains, SE California. *The Geological Society of America.* Vol. 51, No. 4, doi: 10.1130/abs/2019CD-329212

Needy, S., 2009. Tracking the Evolution of Mid Cenozoic Silicic Magma Systems in the Southern Chocolate Mountains Region, California Using Zircon Geochemistry and Quartz and Zircon Geothermometry [M.S. thesis]. Retrieved from: http://hdl.handle.net/1805/1953

Nourse, J. A. (2002). Middle Miocene reconstruction of the central and eastern San GABRIEL MOUNTAINS, southern California, with implications for evolution of the San Gabriel fault and Los Angeles basin. *Contributions to Crustal Evolution of the Southwestern United States*. doi:10.1130/0-8137-2365-5.161

Nourse, J. A., Anderson, T. H., & Silver, L. T. (1994). Tertiary metamorphic CORE complexes in Sonora, northwestern Mexico. *Tectonics*, *13*(5), 1161-1182. doi:10.1029/93tc03324

Parsons, T. (2006). Chapter 7 The Basin and Range Province. In Continental Rifts: Evolution, Structure, Tectonics. Elsevier. https://doi.org/10.1016/s0419-0254(06)80015-7

Paton, C., Hellstrom, J., Paul, B., Woodhead, J., & Hergt, J. (2011). Iolite: Freeware for the visualisation and processing of mass spectrometric data. *Journal of Analytical Atomic Spectrometry, 26*(12), 2508. doi:10.1039/c1ja10172b

Powell, R. E. (1993). Chapter 1: Balanced Palinspastic reconstruction of pre-late Cenozoic paleogeology, southern California: Geologic and Kinematic constraints on evolution of the San Andreas fault system. *Geological Society of America Memoirs*, 1-106. doi:10.1130/mem178-p1

Putirka, K., & Platt, B. (2012). Basin and range volcanism as a passive response to extensional tectonics. *Geosphere, 8*(6), 1274-1285. doi:10.1130/ges00803.1

Ransome, F. L. (1903). Geology of the GLOBE copper District, Arizona. *Professional Paper*. doi:10.3133/pp12

Ricketts, J. W., Girty, G. H., Sainsbury, J. S., Muela, K. K., Sutton, L. A., Biggs, M. A., & Voyles, E. M. (2011). Episodic growth of the Chocolate mountains ANTICLINORIUM recorded by the Neogene Bear canyon CONGLOMERATE, Southeastern California, U.S.A. *Journal of Sedimentary Research, 81*(12), 859-873. doi:10.2110/jsr.2011.66

Sainsbury, J., 2010. Timing of extension, NS shortening, and conjugate strike-slip faulting in the evolution of the Chocolate Mountains anticlinorium: Evidence from the Gavilan Hills, SE California [unpublished MS thesis]: San Diego State University, San Diego, California, 42 p.

San Diego Association of Geologists, San Diego, CA, United States, p. 183-

Scarborough, R.B., 1985, Geologic cross sections of western Arizona Basin and Range, with accompanying geologic maps and other information. Arizona Geological Survey Open File Report, OFR-85-02, 27 map sheet, variable scale, 9 p.

Schell, B., & Wilson, K. (1982). Regional Neotectonic analysis of the Sonoran DESERT, Arizona and California. *Open-File Report*. doi:10.3133/ofr8257

Sherrod, D. R., & Tosdal, R. M. (1991). Geologic setting and Tertiary structural evolution of southwestern Arizona and southeastern California. *Journal of Geophysical Research, 96*(B7), 12407. doi:10.1029/90jb02688

Sherrod, D., Koch, R., & Grubensky, M. (1990). Geologic map of the Vicksburg QUADRANGLE, La Paz County, Arizona. *U.S. Geol. Surv., Quadr. Map* (Gq-1684). doi:10.3133/gq1684

Silver, L.T., 1971, Problems of crystalline rocks of the Transverse Ranges: Geological Society of America Abstracts with Programs, v. 3, p. 193– 194.

Singleton, J. S., Seymour, N. M., Reynolds, S. J., Vomocil, T., & Wong, M. S. (2019). Distributed Neogene faulting across the Western to central Arizona METAMORPHIC core complex belt: Synextensional constriction and superposition of THE PACIFIC–NORTH America plate boundary on the southern Basin and range. *Geosphere, 15*(4), 1409-1435. doi:10.1130/ges02036.1

Sláma, J., Košler, J., Condon, D. J., Crowley, J. L., Gerdes, A., Hanchar, J. M., . . . Whitehouse, M. J. (2008). Plešovice zircon — a new natural reference material for U–pb and HF isotopic microanalysis. *Chemical Geology, 249*(1-2), 1-35. doi:10.1016/j.chemgeo.2007.11.005

SMITH, P. B. (1970). New evidence for a PLIOCENE marine embayment along the Lower Colorado River Area, California and Arizona. *Geological Society of America Bulletin, 81*(5), 1411. doi:10.1130/0016-7606(1970)81[1411:nefapm]2.0.co;2

SUTTON, L.A., 2010, The Copper Basin fault, a newly recognized reverse fault in the lower Colorado River region, SE California: implications for Miocene–Pliocene N–S shortening within the Eastern California Shear Zone [unpublished M.S. thesis]: San Diego State University, San Diego, 42 p.

Tosdal, R. M. (1990). Constraints on the tectonics of the Mule MOUNTAINS Thrust System, southeast California and southwest Arizona. *Journal of Geophysical Research, 95*(B12), 20025. doi:10.1029/jb095ib12p20025

Vermeesch, P., (2012), On the visualisation of detrital age distributions. Chemical Geology, doi: 10.1016/j.chemgeo.2012.04.021.

Vermeesch, P., 2018, IsoplotR: a free and open toolbox for geochronology. Geoscience Frontiers, v.9, p.1479-1493, doi:10.1016/j.gsf.2018.04.001.

Wernicke, B. (n.d.). Cenozoic extensional tectonics of the U.S. CORDILLERA. *The Cordilleran Orogen,* 553-17. doi:10.1130/dnag-gna-g3.553

Wright, H.M., Mangan, M.T. et al. (2013). New insight into the timing of volcanism at Salton Buttes, California from 40Ar/39Ar dating and paleomagnetism. IAVCEI 2013 Scientific Assembly. Retrieved from http://www.kazan.or.jp/iavcei2013/iavcei_hp/PDF/3W_3B-P9.pdf

Zimmermann, S., et al., Maximising data and precision from detrital zircon U-Pb analysis by LA-ICPMS: The use of core-rim ages and the single-analysis Concordia age, Sedimentary Geology (2017), https://doi.org/10.1016/j.sedgeo.2017.12.020

APPENDIX A – Detrital zircon U-Pb ICP-MS analyses

Table A-1: Raw data used for the Concordia diagrams and the relative probability density curves.

		Ratios for Wetherill concordia plot					Ages not corrected for common Pb, Ma						207-corrected ages, Ma		Northing	Easting
Sample	Analysis No.	207Pb/235U	± 1 σ %	206Pb/238U	± 1 σ %	Rho	207Pb/206Pb	± 2 σ, Ma	206Pb/238U	± 2 σ, Ma	207Pb/235U	± 2 σ, Ma	206Pb/238U	± 2 σ, Ma		
A8	P18 098 18 2462 89	0.0237	4.2194	0.0036	1.8071	0.2695	40	160	23	1	24	2	23	1	3698342	694919
A8	P18 098 18 2462 57	0.0247	4.8583	0.0037	1.7492	0.1173	20	170	24	1	25	2	24	1	3698342	694919
A8	P18 098 18 2462 19	0.0308	2.9221	0.0038	1.7002	0.2983	440	120	25	1	31	2	24	1	3698342	694919
A8	P18 098 18 2462 61	0.0304	5.2632	0.0038	1.8229	0.1722	320	190	25	1	30	3	24	1	3698342	694919
A8	P18 098 18 2462 91	0.0264	5.1136	0.0038	1.7065	0.2422	40	180	25	1	26	3	24	1	3698342	694919
A8	P18 098 18 2462 68	0.0242	7.8512	0.0038	1.9737	0.1120	-190	270	24	1	24	4	24	1	3698342	694919
A8	P18 098 18 2462 62	0.0294	5.6122	0.0039	1.8032	0.1256	240	210	25	1	29	3	25	1	3698342	694919
A8	P18 098 18 2462 98	0.0230	6.3043	0.0038	1.9582	-0.1430	-190	210	25	1	23	3	25	1	3698342	694919
A8	P18 098 18 2462 39	0.0240	4.7917	0.0038	2.0833	0.1644	-50	170	25	1	24	2	25	1	3698342	694919
A8	P18 098 18 2462 9	0.0227	3.3040	0.0038	1.5625	0.1638	-150	120	25	1	23	2	25	1	3698342	694919
A8	P18 098 18 2462 71	0.0258	3.8760	0.0039	2.0619	0.1569	80	150	25	1	26	2	25	1	3698342	694919
A8	P18 098 18 2462 52	0.0261	5.1724	0.0039	1.7894	0.0870	40	190	25	1	26	3	25	1	3698342	694919
A8	P18 098 18 2462 8	0.0394	5.3299	0.0040	1.8564	0.4105	820	230	26	1	39	4	25	1	3698342	694919
A8	P18 098 18 2462 75	0.0273	5.1282	0.0040	1.7579	0.1886	70	190	26	1	27	3	26	1	3698342	694919
A8	P18 098 18 2462 81	0.0250	8.6000	0.0040	2.2556	-0.1077	-160	300	26	1	25	4	26	1	3698342	694919
A8	P18 098 18 2462 90	0.0262	3.8168	0.0040	1.7487	0.0003	-10	130	26	1	26	2	26	1	3698342	694919
A8	P18 098 18 2462 40	0.0221	12.6697	0.0041	2.0885	0.1237	-660	370	26	1	22	6	26	1	3698342	694919
A8	P18 098 18 2462 55	0.0453	10.3753	0.0044	2.2831	0.4259	530	380	28	1	44	9	27	1	3698342	694919
A8	P18 098 18 2462 60	0.0837	2.7479	0.0120	1.6304	0.3521	191	95	77	3	81	4	76	2	3698342	694919
A8	P18 098 18 2462 77	0.1550	1.9355	0.0220	1.5668	0.4755	224	61	140	4	146	5	140	4	3698342	694919
A8	P18 098 18 2462 35	0.4020	3.9801	0.0252	1.9841	0.5659	1800	110	160	7	338	22	147	6	3698342	694919
A8	P18 098 18 2462 38	0.1890	2.3810	0.0234	1.5605	0.2944	548	86	149	5	175	8	147	5	3698342	694919
A8	P18 098 18 2462 87	0.1541	2.4335	0.0231	1.7718	0.3707	93	81	147	5	145	7	148	5	3698342	694919
A8	P18 098 18 2462 22	0.1606	1.9925	0.0232	1.6358	0.5115	204	60	148	5	151	6	148	5	3698342	694919
A8	P18 098 18 2462 93	0.1631	2.1766	0.0237	1.4749	0.2033	168	76	151	4	154	6	151	4	3698342	694919
A8	P18 098 18 2462 73	0.1642	2.1924	0.0240	1.6062	0.4085	159	71	153	5	155	6	153	5	3698342	694919
A8	P18 098 18 2462 20	0.1668	3.2974	0.0240	2.0400	0.1886	200	120	153	6	156	10	153	6	3698342	694919
A8	P18 098 18 2462 32	0.2121	2.2631	0.0244	1.4760	0.2160	682	77	155	5	195	8	153	4	3698342	694919
A8	P18 098 18 2462 88	0.1570	5.7325	0.0239	2.0903	0.0472	0	200	152	6	146	15	153	6	3698342	694919

A8	P18 098 18 2462 33	0.1587	1.9849	0.0240	1.6250	0.2418	93	67	153	5	149	6	153	5	3698342	694919
A8	P18 098 18 2462 72	0.1693	2.8352	0.0242	1.8833	0.1184	220	120	154	6	158	8	153	6	3698342	694919
A8	P18 098 18 2462 27	0.1616	1.8874	0.0241	1.5975	0.4934	128	54	154	5	152	5	154	5	3698342	694919
A8	P18 098 18 2462 28	0.1670	5.6886	0.0243	1.7526	-0.0714	50	210	154	5	155	17	154	5	3698342	694919
A8	P18 098 18 2462 31	0.1640	3.3537	0.0243	1.6069	0.3809	100	130	155	5	153	10	154	5	3698342	694919
A8	P18 098 18 2462 56	0.1643	1.9172	0.0243	1.5239	0.4898	151	56	155	5	154	6	155	5	3698342	694919
A8	P18 098 18 2462 21	0.1684	2.3456	0.0245	1.6360	0.2893	169	81	156	5	158	7	156	5	3698342	694919
A8	P18 098 18 2462 41	0.1812	2.5386	0.0247	1.6586	0.2629	328	96	157	5	169	8	156	5	3698342	694919
A8	P18 098 18 2462 13	0.1711	2.2501	0.0247	1.5985	0.3521	188	75	157	5	160	7	157	5	3698342	694919
A8	P18 098 18 2462 23	0.1710	3.2164	0.0249	1.9053	0.3543	200	130	159	6	160	10	158	6	3698342	694919
A8	P18 098 18 2462 10	0.1726	2.6651	0.0252	1.5495	0.3588	152	92	160	5	161	8	160	5	3698342	694919
A8	P18 098 18 2462 54	0.1970	5.3299	0.0260	1.7898	0.2526	210	190	165	6	178	17	164	6	3698342	694919
A8	P18 098 18 2462 76	0.1763	1.7584	0.0258	1.5673	0.2664	159	45	164	5	165	5	164	5	3698342	694919
A8	P18 098 18 2462 46	1.0670	4.4986	0.0902	3.3814	0.8447	1188	77	554	36	704	45	541	36	3698342	694919
A8	P18 098 18 2462 99	1.4350	2.1603	0.1250	1.7600	0.4028	1254	68	759	25	901	26	741	25	3698342	694919
A8	P18 098 18 2462 18	1.5910	1.7599	0.1458	1.5775	0.4414	1163	43	877	26	964	22	865	27	3698342	694919
A8	P18 098 18 2462 45	1.8620	1.8528	0.1597	1.7220	0.5028	1300	42	954	31	1063	24	938	31	3698342	694919
A8	P18 098 18 2462 43	1.7530	1.7114	0.1618	1.6069	0.7247	1165	37	966	29	1025	22	957	30	3698342	694919
A8	P18 098 18 2462 30	1.7600	3.6932	0.1752	1.9121	0.1212	980	140	1040	37	1029	46	1041	39	3698342	694919
A8	P18 098 18 2462 4	1.8960	2.3734	0.1670	1.6766	0.2947	1207	79	995	31	1072	31	983	32	3698342	694919
A8	P18 098 18 2462 50	2.1850	1.5789	0.2121	1.6737	0.5336	1070	44	1239	38	1175	22	1250	41	3698342	694919
A8	P18 098 18 2462 59	1.9300	3.1088	0.1803	1.9689	0.3880	1110	100	1068	39	1085	40	1065	41	3698342	694919
A8	P18 098 18 2462 48	2.0250	1.5309	0.1904	1.6282	0.6488	1133	38	1125	34	1124	22	1122	35	3698342	694919
A8	P18 098 18 2462 78	2.1940	2.0966	0.2012	1.6650	0.3068	1156	72	1181	36	1178	31	1182	38	3698342	694919
A8	P18 098 18 2462 96	2.1920	1.6423	0.2006	1.4955	0.5522	1164	40	1178	32	1176	23	1179	34	3698342	694919
A8	P18 098 18 2462 7	2.2920	1.7234	0.2085	1.4628	0.4382	1165	45	1222	34	1206	24	1224	35	3698342	694919
A8	P18 098 18 2462 85	2.0090	1.8666	0.1842	1.7372	0.5979	1166	48	1088	35	1116	26	1085	37	3698342	694919
A8	P18 098 18 2462 100	2.2490	1.8008	0.2054	1.6796	0.5358	1178	50	1203	37	1198	27	1205	39	3698342	694919
A8	P18 098 18 2462 5	2.2250	2.0225	0.1988	1.5342	0.2025	1179	68	1168	33	1182	28	1166	35	3698342	694919
A8	P18 098 18 2462 2	2.3280	1.8041	0.2094	1.4804	0.4018	1182	50	1225	33	1219	25	1227	35	3698342	694919
A8	P18 098 18 2462 37	2.1550	1.7865	0.1970	1.5990	0.5662	1184	49	1158	34	1165	24	1156	36	3698342	694919
A8	P18 098 18 2462 70	2.2610	1.7028	0.2046	1.6618	0.6313	1184	42	1199	36	1197	24	1200	39	3698342	694919

A8	P18 098 18 2462 34	2.0080	1.6185	0.1841	1.5481	0.7200	1188	35	1089	31	1116	22	1083	33	3698342	694919
A8	P18 098 18 2462 42	1.8440	1.5998	0.1691	1.5376	0.6283	1188	35	1007	29	1059	21	998	30	3698342	694919
A8	P18 098 18 2462 83	1.8930	2.2451	0.1716	2.2436	0.8819	1188	43	1024	44	1075	30	1012	44	3698342	694919
A8	P18 098 18 2462 51	2.2640	2.0760	0.2038	1.5456	0.3915	1191	61	1195	34	1193	30	1194	36	3698342	694919
A8	P18 098 18 2462 49	2.1880	1.8967	0.1989	1.6843	0.6660	1198	45	1168	36	1171	27	1167	38	3698342	694919
A8	P18 098 18 2462 63	2.2810	1.8413	0.2054	1.7040	0.7072	1201	41	1203	38	1202	26	1204	40	3698342	694919
A8	P18 098 18 2462 15	2.1190	1.6753	0.1906	1.5740	0.6516	1202	39	1126	33	1155	23	1120	34	3698342	694919
A8	P18 098 18 2462 69	2.3540	1.7417	0.2114	1.5847	0.3280	1202	52	1236	36	1226	25	1237	38	3698342	694919
A8	P18 098 18 2462 17	2.1180	1.5817	0.1913	1.5682	0.6914	1203	33	1128	32	1153	22	1124	34	3698342	694919
A8	P18 098 18 2462 16	2.1220	1.7672	0.1917	1.6171	0.5609	1205	45	1130	33	1160	25	1126	35	3698342	694919
A8	P18 098 18 2462 94	2.2330	2.1720	0.1958	1.5577	0.0710	1215	76	1152	33	1185	30	1147	35	3698342	694919
A8	P18 098 18 2462 6	2.0960	1.9561	0.1846	1.5710	0.4839	1216	59	1091	32	1138	24	1083	33	3698342	694919
A8	P18 098 18 2462 64	2.3060	1.7997	0.2079	1.6835	0.4895	1216	46	1217	37	1211	25	1218	40	3698342	694919
A8	P18 098 18 2462 44	2.3160	1.6408	0.2074	1.4706	0.5668	1223	37	1214	32	1216	23	1214	35	3698342	694919
A8	P18 098 18 2462 25	2.0540	1.8257	0.1784	1.9619	0.7922	1276	42	1057	39	1131	25	1047	40	3698342	694919
A8	P18 098 18 2462 67	2.3920	2.0485	0.2029	1.7003	0.5660	1323	55	1190	37	1238	30	1181	39	3698342	694919
A8	P18 098 18 2462 1	2.0200	1.8812	0.1697	1.8268	0.5093	1331	55	1009	34	1119	26	993	35	3698342	694919
A8	P18 098 18 2462 65	3.0340	1.5821	0.2484	1.5700	0.7233	1389	31	1429	40	1414	24	1434	44	3698342	694919
A8	P18 098 18 2462 95	3.3040	1.9673	0.2492	1.6653	0.6888	1534	43	1436	44	1477	30	1425	46	3698342	694919
A8	P18 098 18 2462 58	3.5500	1.9718	0.2636	1.8209	0.7909	1576	39	1506	49	1532	32	1501	54	3698342	694919
A8	P18 098 18 2462 24	4.2400	1.5330	0.3095	1.5024	0.6325	1621	32	1737	46	1680	25	1753	53	3698342	694919
A8	P18 098 18 2462 36	3.6850	1.7639	0.2681	1.5852	0.4028	1633	43	1530	43	1568	29	1520	48	3698342	694919
A8	P18 098 18 2462 12	4.1240	1.6974	0.2939	1.5822	0.7023	1642	35	1659	47	1655	28	1663	52	3698342	694919
A8	P18 098 18 2462 66	4.1820	1.5543	0.2992	1.6043	0.7669	1648	30	1685	47	1668	26	1692	54	3698342	694919
A8	P18 098 18 2462 84	4.2600	1.6432	0.3008	1.5791	0.7061	1655	35	1693	47	1683	27	1699	54	3698342	694919
A8	P18 098 18 2462 11	4.2330	1.5356	0.2991	1.5547	0.6848	1676	30	1685	46	1680	26	1689	52	3698342	694919
A8	P18 098 18 2462 3	4.2640	1.5244	0.2992	1.4873	0.5354	1676	34	1686	44	1684	26	1688	50	3698342	694919
A8	P18 098 18 2462 82	4.2490	1.5298	0.2980	1.4933	0.6020	1676	34	1680	44	1683	27	1681	50	3698342	694919
A8	P18 098 18 2462 26	3.4220	1.7534	0.2415	1.6977	0.7579	1678	35	1393	42	1506	28	1367	45	3698342	694919
A8	P18 098 18 2462 86	4.2600	1.7606	0.2976	1.5289	0.4443	1681	41	1679	45	1682	29	1678	51	3698342	694919
A8	P18 098 18 2462 47	4.0940	1.5877	0.2892	1.4523	0.5564	1684	30	1637	42	1651	26	1632	47	3698342	694919
A8	P18 098 18 2462 29	4.4900	1.5590	0.3156	1.4892	0.5997	1687	32	1767	46	1727	26	1779	53	3698342	694919

A8	P18 098 18 2462 92	4.0660	1.5986	0.2839	1.4794	0.5839	1687	31	1610	42	1645	26	1602	47	3698342	694919
A8	P18 098 18 2462 79	4.5590	1.6451	0.3174	1.7328	0.7295	1689	34	1774	52	1737	29	1788	62	3698342	694919
A8	P18 098 18 2462 97	4.2050	1.6647	0.2925	1.5726	0.6118	1689	36	1652	46	1671	27	1649	52	3698342	694919
A8	P18 098 18 2462 74	4.2600	1.6432	0.2960	1.5541	0.7147	1693	34	1670	46	1681	28	1668	52	3698342	694919
A8	P18 098 18 2462 80	4.3930	1.7073	0.3035	1.5651	0.6971	1693	35	1707	47	1707	28	1710	53	3698342	694919
A8	P18 098 18 2462 14	4.2690	1.6397	0.2956	1.5731	0.6817	1701	34	1668	46	1683	28	1665	52	3698342	694919
A8	P18 098 18 2462 53	4.2800	2.5701	0.2870	1.7247	0.7254	1763	63	1626	50	1682	41	1608	55	3698342	694919
A2	P18 098 18 2463 83	0.0202	4.2079	0.0028	1.9531	0.0771	190	160	18	1	20	2	18	1	3698319	694777
A2	P18 098 18 2463 43	0.0300	4.5000	0.0033	2.5449	0.5747	620	130	22	1	30	3	21	1	3698319	694777
A2	P18 098 18 2463 73	0.0425	8.7059	0.0038	2.6178	0.2128	780	360	25	1	42	7	24	1	3698319	694777
A2	P18 098 18 2463 34	0.0185	11.8919	0.0036	2.0718	0.0232	-500	320	23	1	18	4	24	1	3698319	694777
A2	P18 098 18 2463 67	0.0296	4.7297	0.0038	1.7329	0.4469	380	170	24	1	30	3	24	1	3698319	694777
A2	P18 098 18 2463 41	0.0247	3.4413	0.0037	1.7459	0.3108	10	120	24	1	25	2	24	1	3698319	694777
A2	P18 098 18 2463 96	0.0245	3.0612	0.0038	1.7251	0.2999	50	110	24	1	25	2	24	1	3698319	694777
A2	P18 098 18 2463 82	0.0491	4.3788	0.0040	2.2613	0.3500	1270	160	26	1	49	4	24	1	3698319	694777
A2	P18 098 18 2463 46	0.0368	2.3098	0.0039	1.5468	0.2141	824	86	25	1	37	2	24	1	3698319	694777
A2	P18 098 18 2463 2	0.0283	4.2403	0.0038	1.5806	0.9370	275	100	24	1	28	2	24	1	3698319	694777
A2	P18 098 18 2463 48	0.0240	2.9167	0.0038	1.7182	0.2711	-30	100	24	1	24	1	24	1	3698319	694777
A2	P18 098 18 2463 12	0.0584	4.9658	0.0041	2.4390	0.6140	1470	130	26	1	57	5	25	1	3698319	694777
A2	P18 098 18 2463 37	0.0326	3.3742	0.0039	1.9280	0.3386	550	130	25	1	33	2	25	1	3698319	694777
A2	P18 098 18 2463 6	0.0261	3.2567	0.0039	1.6766	0.0163	120	120	25	1	26	2	25	1	3698319	694777
A2	P18 098 18 2463 72	0.0253	3.5573	0.0039	1.6774	0.0730	20	130	25	1	25	2	25	1	3698319	694777
A2	P18 098 18 2463 25	0.0242	3.0992	0.0039	1.9330	0.2908	-50	110	25	1	24	2	25	1	3698319	694777
A2	P18 098 18 2463 28	0.0307	8.3062	0.0040	2.2785	0.3244	170	220	25	1	31	5	25	1	3698319	694777
A2	P18 098 18 2463 89	0.0264	4.1667	0.0039	1.7771	-0.0060	70	160	25	1	26	2	25	1	3698319	694777
A2	P18 098 18 2463 71	0.0255	2.9412	0.0039	1.9036	0.2345	20	110	25	1	26	2	25	1	3698319	694777
A2	P18 098 18 2463 50	0.0367	5.3134	0.0050	3.2000	0.2624	160	150	32	2	36	4	32	2	3698319	694777
A2	P18 098 18 2463 11	0.0752	3.1915	0.0114	1.5748	0.0875	70	120	73	2	74	5	73	2	3698319	694777
A2	P18 098 18 2463 74	0.0770	1.8182	0.0115	1.5271	0.4283	112	55	73	2	75	3	73	2	3698319	694777
A2	P18 098 18 2463 97	0.0922	2.7115	0.0118	1.6553	0.7933	415	100	76	3	89	5	75	2	3698319	694777
A2	P18 098 18 2463 95	0.4660	3.8627	0.0149	2.0442	0.6330	2910	100	95	4	381	25	75	3	3698319	694777
A2	P18 098 18 2463 49	0.0866	4.2725	0.0121	2.3651	0.0670	210	180	77	4	84	7	77	4	3698319	694777

A2	P18 098 18 2463 88	0.0827	2.4184	0.0123	1.7872	0.2267	103	81	79	3	81	4	79	3	3698319	694777
A2	P18 098 18 2463 84	0.1196	2.5920	0.0135	1.6296	0.1525	700	110	86	3	114	6	85	3	3698319	694777
A2	P18 098 18 2463 94	0.6720	2.3065	0.0224	1.8535	0.3987	2937	63	143	5	520	19	113	4	3698319	694777
A2	P18 098 18 2463 90	0.1645	2.6748	0.0230	1.8905	0.4436	271	100	147	6	154	8	146	5	3698319	694777
A2	P18 098 18 2463 65	0.1598	2.3154	0.0232	1.6415	0.2773	153	79	148	5	150	6	147	5	3698319	694777
A2	P18 098 18 2463 23	0.2330	4.7210	0.0240	2.0451	0.9274	830	140	153	6	210	18	149	6	3698319	694777
A2	P18 098 18 2463 30	0.1980	3.0303	0.0238	1.6625	0.4765	552	97	151	5	183	10	149	5	3698319	694777
A2	P18 098 18 2463 32	0.1590	1.9497	0.0234	1.5998	0.4795	133	58	149	5	150	5	149	5	3698319	694777
A2	P18 098 18 2463 24	0.1840	5.9783	0.0236	1.6737	0.5676	230	120	150	5	160	11	149	5	3698319	694777
A2	P18 098 18 2463 63	0.1690	3.8462	0.0236	1.6737	0.2176	190	140	150	5	158	11	150	5	3698319	694777
A2	P18 098 18 2463 13	0.1530	3.5948	0.0235	1.9362	-0.0598	80	160	150	6	144	10	150	6	3698319	694777
A2	P18 098 18 2463 75	0.1636	1.6809	0.0236	1.4594	0.8024	171	47	151	4	154	5	150	4	3698319	694777
A2	P18 098 18 2463 45	0.1864	2.3605	0.0241	1.9063	0.5881	411	75	154	6	173	7	152	6	3698319	694777
A2	P18 098 18 2463 69	0.1820	20.8791	0.0240	2.7083	0.8666	-50	470	153	8	152	50	153	9	3698319	694777
A2	P18 098 18 2463 68	0.1668	2.4580	0.0242	1.9016	0.1520	158	95	154	6	157	7	154	6	3698319	694777
A2	P18 098 18 2463 38	0.1683	2.7035	0.0243	1.7916	0.5001	151	95	155	6	157	8	154	6	3698319	694777
A2	P18 098 18 2463 91	0.1840	3.2609	0.0246	1.6904	0.2444	300	120	156	5	171	10	155	5	3698319	694777
A2	P18 098 18 2463 61	0.1756	2.1071	0.0246	1.6044	0.2489	229	76	157	5	164	6	156	5	3698319	694777
A2	P18 098 18 2463 42	0.1808	2.4889	0.0248	1.6532	0.3183	246	85	158	5	168	8	158	5	3698319	694777
A2	P18 098 18 2463 98	0.1792	2.3438	0.0252	1.5681	0.4380	242	80	160	5	168	8	160	5	3698319	694777
A2	P18 098 18 2463 76	0.1748	2.2025	0.0253	1.6193	0.4181	165	71	161	5	163	7	161	5	3698319	694777
A2	P18 098 18 2463 92	0.2048	2.3682	0.0258	1.5310	0.3430	466	84	164	5	189	8	163	5	3698319	694777
A2	P18 098 18 2463 19	0.1770	3.6723	0.0256	1.9539	0.5213	170	130	163	6	164	11	163	6	3698319	694777
A2	P18 098 18 2463 59	0.1771	1.8351	0.0257	1.4763	0.3302	146	54	164	5	165	6	164	5	3698319	694777
A2	P18 098 18 2463 7	0.1803	2.5790	0.0259	1.6017	0.3076	190	93	165	5	168	8	165	5	3698319	694777
A2	P18 098 18 2463 58	0.8070	4.7088	0.0392	1.6565	0.6927	2140	140	248	8	591	43	218	8	3698319	694777
A2	P18 098 18 2463 80	0.2582	1.6266	0.0363	1.5152	0.2733	232	44	230	7	233	7	230	7	3698319	694777
A2	P18 098 18 2463 39	2.1820	1.9019	0.1985	1.6373	0.4014	1157	59	1166	35	1172	27	1167	37	3698319	694777
A2	P18 098 18 2463 93	2.3640	2.1151	0.2119	1.6281	0.4916	1164	64	1238	36	1222	31	1242	39	3698319	694777
A2	P18 098 18 2463 35	2.1930	1.9380	0.1981	1.7668	0.5641	1169	54	1164	38	1174	27	1165	40	3698319	694777
A2	P18 098 18 2463 54	2.2160	1.7148	0.1974	1.6211	0.9835	1194	41	1160	34	1183	24	1159	36	3698319	694777
A2	P18 098 18 2463 1	2.2610	1.6364	0.2042	1.5671	0.6939	1202	34	1197	34	1198	23	1197	36	3698319	694777

A2	P18 098 18 2463 14	2.2290	1.8394	0.1987	1.5601	0.5254	1207	51	1167	33	1188	25	1165	35	3698319	694777
A2	P18 098 18 2463 56	2.2270	1.6839	0.1975	1.6456	0.8147	1208	33	1161	35	1187	24	1159	37	3698319	694777
A2	P18 098 18 2463 57	2.2840	1.7513	0.2016	1.4881	0.3135	1219	51	1183	32	1207	26	1181	34	3698319	694777
A2	P18 098 18 2463 20	2.3260	2.3646	0.2049	1.6105	0.3111	1237	76	1201	35	1218	31	1198	38	3698319	694777
A2	P18 098 18 2463 53	3.0310	1.6496	0.2342	1.5371	0.6855	1469	34	1358	38	1412	26	1346	40	3698319	694777
A2	P18 098 18 2463 10	2.2110	1.8318	0.1719	1.5998	0.5324	1472	58	1021	30	1183	27	996	31	3698319	694777
A2	P18 098 18 2463 47	3.3900	1.6224	0.2496	1.5825	0.7082	1562	34	1435	41	1498	26	1424	44	3698319	694777
A2	P18 098 18 2463 9	4.0250	1.7391	0.2889	1.7307	0.7840	1647	37	1634	50	1638	27	1633	56	3698319	694777
A2	P18 098 18 2463 18	4.1300	1.9370	0.2918	1.7135	0.7385	1655	41	1648	50	1659	32	1649	56	3698319	694777
A2	P18 098 18 2463 86	4.1200	2.0631	0.2860	2.2727	0.8903	1665	42	1634	63	1643	42	1614	73	3698319	694777
A2	P18 098 18 2463 21	4.1180	1.6999	0.2885	1.6291	0.7144	1671	35	1632	47	1654	28	1628	53	3698319	694777
A2	P18 098 18 2463 5	3.7420	1.6034	0.2640	1.4962	0.6371	1672	32	1509	40	1579	25	1493	44	3698319	694777
A2	P18 098 18 2463 79	4.3040	1.6264	0.3009	1.5287	0.6468	1673	35	1694	46	1691	27	1698	52	3698319	694777
A2	P18 098 18 2463 51	4.6300	1.5119	0.3216	1.4614	0.7475	1677	28	1796	46	1755	26	1815	53	3698319	694777
A2	P18 098 18 2463 64	4.4760	1.6756	0.3104	1.5625	0.7314	1678	33	1741	48	1725	28	1750	55	3698319	694777
A2	P18 098 18 2463 36	4.2970	1.6290	0.2973	1.5977	0.7695	1682	30	1679	49	1689	28	1677	53	3698319	694777
A2	P18 098 18 2463 77	4.2550	1.6451	0.2955	1.5736	0.7362	1683	32	1667	46	1681	27	1666	52	3698319	694777
A2	P18 098 18 2463 33	3.5510	1.6897	0.2462	1.5435	0.6228	1685	36	1418	39	1537	27	1392	42	3698319	694777
A2	P18 098 18 2463 40	4.3700	1.8307	0.3019	1.8218	0.5434	1685	46	1698	54	1702	30	1702	62	3698319	694777
A2	P18 098 18 2463 99	4.2970	1.7454	0.2987	1.6237	0.3048	1686	36	1683	48	1688	28	1684	54	3698319	694777
A2	P18 098 18 2463 17	3.9950	1.7522	0.2774	1.6402	0.7526	1687	34	1580	47	1628	28	1565	51	3698319	694777
A2	P18 098 18 2463 78	4.7200	2.0127	0.3271	1.8343	0.8285	1688	34	1820	59	1763	33	1844	68	3698319	694777
A2	P18 098 18 2463 87	4.1180	1.6999	0.2856	1.5931	0.7768	1688	31	1618	45	1654	27	1611	51	3698319	694777
A2	P18 098 18 2463 70	4.8360	1.6543	0.3326	1.6536	0.6597	1689	37	1848	52	1786	29	1874	63	3698319	694777
A2	P18 098 18 2463 100	4.2890	1.7487	0.2983	1.5756	0.5174	1690	45	1682	47	1688	28	1681	53	3698319	694777
A2	P18 098 18 2463 55	4.0380	1.4859	0.2780	1.4928	0.7303	1693	29	1580	42	1641	25	1568	46	3698319	694777
A2	P18 098 18 2463 29	4.1200	1.6990	0.2848	1.6152	0.6751	1694	34	1614	46	1655	27	1605	51	3698319	694777
A2	P18 098 18 2463 62	4.3100	1.6241	0.2954	1.5403	0.8331	1695	28	1667	46	1694	27	1664	51	3698319	694777
A2	P18 098 18 2463 16	4.2370	1.6521	0.2945	1.5620	0.4557	1696	42	1662	46	1681	28	1659	52	3698319	694777
A2	P18 098 18 2463 4	4.3440	1.6114	0.3030	1.5512	0.6196	1697	35	1705	46	1701	28	1707	53	3698319	694777
A2	P18 098 18 2463 22	4.1010	1.7069	0.2819	1.6140	0.6673	1699	37	1599	46	1654	28	1588	51	3698319	694777
A2	P18 098 18 2463 27	4.2300	1.6548	0.2897	1.5706	0.6266	1702	40	1638	46	1677	29	1631	51	3698319	694777

A2	P18 098 18 2463 15	4.2250	1.6568	0.2908	1.6678	0.7626	1704	32	1647	49	1674	28	1638	54	3698319	694777
A2	P18 098 18 2463 26	4.4900	2.0045	0.3054	1.9646	0.7490	1717	47	1716	59	1730	35	1717	67	3698319	694777
A2	P18 098 18 2463 52	3.9100	1.9182	0.2649	1.8120	0.5727	1720	37	1513	49	1614	34	1494	53	3698319	694777
A2	P18 098 18 2463 31	4.0620	1.7233	0.2762	1.7560	0.7848	1724	34	1570	49	1644	28	1555	54	3698319	694777
A2	P18 098 18 2463 81	4.1710	1.5584	0.2872	1.6539	0.6328	1725	33	1630	46	1669	28	1615	53	3698319	694777
A2	P18 098 18 2463 60	4.3090	1.6245	0.2910	1.5979	0.7727	1730	31	1645	46	1694	27	1636	52	3698319	694777
A2	P18 098 18 2463 44	4.3040	1.7426	0.2874	1.5832	0.7265	1741	34	1627	45	1689	27	1614	51	3698319	694777
A2	P18 098 18 2463 8	4.3700	1.6018	0.2971	1.4978	0.6837	1741	29	1676	44	1704	26	1668	50	3698319	694777
A2	P18 098 18 2463 66	4.0840	1.5916	0.2745	1.5847	0.7075	1746	31	1562	44	1648	26	1543	48	3698319	694777
A2	P18 098 18 2463 3	4.6200	1.8398	0.3038	1.6458	0.3285	1799	50	1708	49	1753	32	1695	56	3698319	694777
A2	P18 098 18 2463 85	4.5100	1.9956	0.2899	1.8972	0.4614	1843	58	1644	54	1726	32	1611	61	3698319	694777
TCCG	P18 098 18 2464 3	0.0172	3.1977	0.0026	1.6296	0.1631	60	120	17	1	17	1	17	1	3695069	693068
TCCG	P18 098 18 2464 14	0.0221	6.1086	0.0036	2.6761	0.0334	-40	250	23	1	22	3	23	1	3695069	693068
TCCG	P18 098 18 2464 36	0.0398	4.2714	0.0038	2.0000	0.3333	1020	170	24	1	40	3	23	1	3695069	693068
TCCG	P18 098 18 2464 16	0.0271	6.8266	0.0037	2.0492	0.3443	300	240	24	1	27	4	23	1	3695069	693068
TCCG	P18 098 18 2464 20	0.0349	7.7364	0.0038	2.5333	0.0502	340	300	24	1	34	5	23	1	3695069	693068
TCCG	P18 098 18 2464 44	0.0255	4.3137	0.0038	1.8519	0.0462	110	170	24	1	26	2	24	1	3695069	693068
TCCG	P18 098 18 2464 30	0.0255	4.1176	0.0038	1.9789	0.2607	130	150	24	1	26	2	24	1	3695069	693068
TCCG	P18 098 18 2464 5	0.0319	8.4639	0.0039	2.3316	0.3877	370	300	25	1	32	5	24	1	3695069	693068
TCCG	P18 098 18 2464 35	0.0273	4.7619	0.0039	1.8182	0.1816	210	190	25	1	27	3	25	1	3695069	693068
TCCG	P18 098 18 2464 59	0.0272	4.0441	0.0039	1.6879	0.0637	170	150	25	1	27	2	25	1	3695069	693068
TCCG	P18 098 18 2464 47	0.0275	4.9091	0.0039	1.6852	0.1080	120	180	25	1	28	3	25	1	3695069	693068
TCCG	P18 098 18 2464 22	0.0360	6.1111	0.0040	2.0202	0.3087	480	250	26	1	36	4	25	1	3695069	693068
TCCG	P18 098 18 2464 31	0.0300	5.1667	0.0039	1.6620	0.1147	280	190	25	1	30	3	25	1	3695069	693068
TCCG	P18 098 18 2464 10	0.0274	3.4672	0.0040	1.7592	0.2044	150	140	26	1	27	2	25	1	3695069	693068
TCCG	P18 098 18 2464 12	0.0361	2.3546	0.0041	2.0782	0.5450	743	74	26	1	36	2	26	1	3695069	693068
TCCG	P18 098 18 2464 27	0.0273	10.6227	0.0040	2.8465	0.1368	-20	380	26	2	27	6	26	2	3695069	693068
TCCG	P18 098 18 2464 24	0.2027	1.8747	0.0153	2.8086	0.6112	1582	83	98	5	187	6	91	5	3695069	693068
TCCG	P18 098 18 2464 55	0.2085	1.5827	0.0183	2.7352	-0.2734	1300	110	117	6	192	6	111	6	3695069	693068
TCCG	P18 098 18 2464 1	0.1921	1.6658	0.0226	1.7493	0.3412	653	60	144	5	178	6	142	5	3695069	693068
TCCG	P18 098 18 2464 51	0.1673	2.1219	0.0225	1.8453	0.3674	343	80	143	5	157	6	142	5	3695069	693068
TCCG	P18 098 18 2464 21	0.1731	2.1953	0.0231	1.8406	0.4570	366	75	147	5	162	7	146	5	3695069	693068

TCCG	P18 098 18 2464 4	0.1953	2.5602	0.0236	1.5228	0.4584	520	100	151	5	181	8	149	5	3695069	693068
TCCG	P18 098 18 2464 28	0.1671	1.7654	0.0238	1.7045	0.1518	260	57	151	5	157	5	151	5	3695069	693068
TCCG	P18 098 18 2464 32	0.1600	1.7188	0.0237	1.4557	0.3732	150	50	151	4	151	5	151	4	3695069	693068
TCCG	P18 098 18 2464 37	0.1595	1.7555	0.0237	1.5388	0.5828	142	47	151	5	150	5	151	5	3695069	693068
TCCG	P18 098 18 2464 40	0.1970	4.5685	0.0241	2.6971	0.3054	550	160	153	8	182	15	151	8	3695069	693068
TCCG	P18 098 18 2464 18	0.1560	4.4872	0.0238	1.9924	0.0564	50	170	152	6	147	12	152	6	3695069	693068
TCCG	P18 098 18 2464 13	0.1651	2.9376	0.0239	1.7768	0.2602	171	100	152	5	155	8	152	5	3695069	693068
TCCG	P18 098 18 2464 6	0.1777	1.7164	0.0243	1.5857	0.3831	327	55	155	5	166	5	154	5	3695069	693068
TCCG	P18 098 18 2464 49	0.3410	5.8651	0.0257	1.8295	0.5781	1370	190	164	6	292	29	154	6	3695069	693068
TCCG	P18 098 18 2464 57	0.1707	1.8453	0.0246	1.5682	0.9416	193	47	156	5	160	5	156	5	3695069	693068
TCCG	P18 098 18 2464 48	0.1756	1.8793	0.0246	1.5834	0.3766	262	58	157	5	164	6	156	5	3695069	693068
TCCG	P18 098 18 2464 43	2.2700	1.6740	0.2069	1.4500	0.6841	1201	39	1212	32	1203	25	1212	34	3695069	693068
TCCG	P18 098 18 2464 46	2.2250	1.6629	0.2007	1.4948	0.5936	1211	40	1178	32	1188	22	1176	34	3695069	693068
TCCG	P18 098 18 2464 11	2.2290	1.9291	0.1998	1.6517	0.5750	1223	50	1173	36	1184	27	1170	38	3695069	693068
TCCG	P18 098 18 2464 17	2.3510	1.9353	0.2057	1.6286	0.3830	1250	56	1205	36	1224	27	1202	38	3695069	693068
TCCG	P18 098 18 2464 26	2.0800	4.0865	0.1780	3.6517	0.8821	1290	80	1055	69	1129	61	1043	74	3695069	693068
TCCG	P18 098 18 2464 34	3.9600	1.8939	0.2961	1.8575	0.9061	1571	31	1668	53	1618	33	1684	62	3695069	693068
TCCG	P18 098 18 2464 7	3.4120	1.7585	0.2530	1.7391	0.8382	1571	32	1452	45	1503	27	1442	49	3695069	693068
TCCG	P18 098 18 2464 52	3.5770	1.5376	0.2600	1.5385	0.6736	1630	33	1489	41	1545	27	1475	45	3695069	693068
TCCG	P18 098 18 2464 25	4.1890	1.7904	0.3048	1.8045	0.7357	1633	40	1716	54	1668	29	1725	62	3695069	693068
TCCG	P18 098 18 2464 50	3.8800	1.6753	0.2790	1.5771	0.8865	1644	26	1584	45	1606	27	1579	49	3695069	693068
TCCG	P18 098 18 2464 15	4.3010	1.6275	0.3086	1.5878	0.7433	1652	30	1732	48	1690	27	1744	55	3695069	693068
TCCG	P18 098 18 2464 56	3.8040	1.5773	0.2720	1.5625	0.7330	1656	30	1550	43	1592	25	1539	47	3695069	693068
TCCG	P18 098 18 2464 8	4.4700	1.7897	0.3187	1.7258	0.8172	1659	32	1780	53	1721	31	1800	63	3695069	693068
TCCG	P18 098 18 2464 42	4.3990	1.5913	0.3147	1.5094	0.7530	1660	29	1762	47	1709	27	1778	54	3695069	693068
TCCG	P18 098 18 2464 41	3.8430	1.5613	0.2744	1.4942	0.5373	1662	31	1562	41	1600	25	1552	46	3695069	693068
TCCG	P18 098 18 2464 23	4.1700	1.9185	0.2944	1.6984	0.8728	1666	31	1661	50	1662	30	1662	56	3695069	693068
TCCG	P18 098 18 2464 19	3.8380	1.5633	0.2694	1.5405	0.6747	1675	32	1536	42	1598	25	1522	46	3695069	693068
TCCG	P18 098 18 2464 53	4.2790	1.6359	0.2989	1.5557	0.8739	1684	27	1684	46	1686	26	1685	52	3695069	693068
TCCG	P18 098 18 2464 9	4.3660	1.7178	0.3016	1.6578	0.6924	1693	42	1703	52	1702	28	1698	56	3695069	693068
TCCG	P18 098 18 2464 54	4.3520	1.4936	0.3031	1.4847	0.7257	1700	29	1705	44	1701	25	1707	51	3695069	693068
TCCG	P18 098 18 2464 33	4.0490	1.6053	0.2810	1.6726	0.6340	1726	39	1594	47	1643	28	1580	52	3695069	693068

TCCG	P18 098 18 2464 2	4.2120	1.6619	0.2876	1.5994	0.6229	1727	37	1628	46	1673	27	1617	51	3695069	693068
TCCG	P18 098 18 2464 58	4.6070	1.7365	0.3156	1.5526	0.6079	1728	37	1767	48	1747	28	1773	55	3695069	693068
TCCG	P18 098 18 2464 45	3.7560	1.7306	0.2561	1.6595	0.7998	1749	33	1468	44	1581	28	1441	47	3695069	693068
TCCG	P18 098 18 2464 60	4.5570	1.6458	0.3070	1.5309	0.5543	1760	35	1724	46	1738	27	1720	53	3695069	693068
TCCG	P18 098 18 2464 39	4.4000	2.3864	0.2800	2.3214	0.6411	1857	63	1589	68	1696	39	1554	71	3695069	693068
TCCG	P18 098 18 2464 38	4.3700	2.4027	0.2750	2.3636	0.6256	1889	68	1558	66	1692	41	1522	71	3695069	693068
TCGS	P18 098 18 2465 59	0.0684	3.7281	0.0040	1.7383	0.4851	1970	110	26	1	67	5	23	1	3696165	692975
TCGS	P18 098 18 2465 74	0.0253	2.3734	0.0038	1.5996	0.1525	124	86	24	1	25	1	24	1	3696165	692975
TCGS	P18 098 18 2465 61	0.0243	2.8807	0.0038	1.7329	0.1835	50	110	24	1	24	1	24	1	3696165	692975
TCGS	P18 098 18 2465 1	0.0281	4.4484	0.0038	1.8353	0.0517	270	160	25	1	28	3	24	1	3696165	692975
TCGS	P18 098 18 2465 15	0.0332	2.5602	0.0039	1.6667	0.4954	625	86	25	1	33	2	25	1	3696165	692975
TCGS	P18 098 18 2465 33	0.0329	13.8298	0.0039	2.5575	-0.0319	-460	500	25	1	32	9	25	1	3696165	692975
TCGS	P18 098 18 2465 63	0.0261	4.5977	0.0039	1.8079	-0.0204	50	170	25	1	26	2	25	1	3696165	692975
TCGS	P18 098 18 2465 35	0.0275	2.9091	0.0039	1.7857	0.3511	220	100	25	1	28	2	25	1	3696165	692975
TCGS	P18 098 18 2465 79	0.0357	5.7423	0.0040	2.2444	0.1378	600	250	26	1	35	4	25	1	3696165	692975
TCGS	P18 098 18 2465 5	0.0263	7.7947	0.0040	1.8987	0.1561	-170	270	26	1	26	4	25	1	3696165	692975
TCGS	P18 098 18 2465 71	0.1060	5.6604	0.0047	2.3555	0.7898	2440	160	30	1	101	11	26	1	3696165	692975
TCGS	P18 098 18 2465 8	0.0286	3.3217	0.0040	1.6197	0.2838	240	130	26	1	29	2	26	1	3696165	692975
TCGS	P18 098 18 2465 42	0.2940	5.6122	0.0061	2.7094	0.8670	3130	240	39	2	251	26	26	2	3696165	692975
TCGS	P18 098 18 2465 66	0.0352	4.2614	0.0041	1.8248	0.3034	530	140	26	1	35	3	26	1	3696165	692975
TCGS	P18 098 18 2465 51	0.0370	10.1351	0.0041	3.1477	0.2566	380	420	27	2	37	7	26	2	3696165	692975
TCGS	P18 098 18 2465 19	0.0361	4.1551	0.0043	2.0979	0.2599	480	160	28	1	36	3	27	1	3696165	692975
TCGS	P18 098 18 2465 6	0.0827	2.1765	0.0120	1.5794	0.1632	172	78	77	2	81	3	77	2	3696165	692975
TCGS	P18 098 18 2465 49	2.2400	14.0625	0.0245	12.4490	0.9699	3660	210	152	37	780	150	77	21	3696165	692975
TCGS	P18 098 18 2465 68	0.1576	2.1574	0.0219	1.7548	0.4852	282	74	140	5	149	6	139	5	3696165	692975
TCGS	P18 098 18 2465 62	0.5190	2.0231	0.0255	1.6883	0.2997	2322	57	162	5	423	14	142	5	3696165	692975
TCGS	P18 098 18 2465 65	0.1543	3.5645	0.0228	2.6316	0.6347	140	110	145	7	146	9	145	8	3696165	692975
TCGS	P18 098 18 2465 76	0.1970	3.5533	0.0237	1.6695	0.4825	550	120	151	5	182	11	149	5	3696165	692975
TCGS	P18 098 18 2465 57	0.1644	2.4331	0.0235	1.4662	0.1165	195	90	150	4	154	7	150	4	3696165	692975
TCGS	P18 098 18 2465 70	0.1650	6.9697	0.0239	1.9062	0.0652	-40	260	152	6	149	21	152	6	3696165	692975
TCGS	P18 098 18 2465 55	0.1634	2.3868	0.0239	2.0938	0.3697	176	94	152	7	154	7	152	6	3696165	692975
TCGS	P18 098 18 2465 13	0.1671	2.0048	0.0240	1.5847	0.4344	197	62	153	5	157	6	152	5	3696165	692975

TCGS	P18 098 18 2465 12	0.3580	3.3520	0.0258	1.7241	0.5731	1620	120	164	6	307	18	154	5	3696165	692975
TCGS	P18 098 18 2465 14	0.1606	2.6152	0.0241	1.6798	0.3528	100	94	154	5	151	7	154	5	3696165	692975
TCGS	P18 098 18 2465 60	0.1662	2.9783	0.0242	1.6322	-0.0081	150	120	154	5	155	9	154	5	3696165	692975
TCGS	P18 098 18 2465 22	0.2070	3.1401	0.0247	1.6188	0.1842	550	110	157	5	190	10	155	5	3696165	692975
TCGS	P18 098 18 2465 56	0.1656	1.9928	0.0247	1.5783	0.2384	110	70	157	5	155	6	158	5	3696165	692975
TCGS	P18 098 18 2465 17	0.1821	2.3064	0.0263	1.5048	0.3346	183	79	167	5	169	7	167	5	3696165	692975
TCGS	P18 098 18 2465 28	0.2140	3.0374	0.0268	1.6592	0.1711	440	120	171	6	197	11	169	6	3696165	692975
TCGS	P18 098 18 2465 64	0.2401	1.6660	0.0341	1.6153	0.6053	249	48	216	7	218	7	216	7	3696165	692975
TCGS	P18 098 18 2465 7	0.2790	1.6667	0.0375	1.4674	0.6899	361	42	237	7	250	7	236	7	3696165	692975
TCGS	P18 098 18 2465 43	1.0780	1.9481	0.1194	1.9263	0.4466	759	63	726	27	739	21	725	27	3696165	692975
TCGS	P18 098 18 2465 27	2.0090	1.6177	0.1837	1.6059	0.8842	1173	35	1086	32	1116	22	1082	34	3696165	692975
TCGS	P18 098 18 2465 32	2.2440	1.7380	0.2046	1.8328	0.7422	1180	42	1198	40	1193	24	1201	43	3696165	692975
TCGS	P18 098 18 2465 50	2.2320	1.8145	0.2015	1.5881	0.6041	1198	44	1182	34	1191	26	1182	36	3696165	692975
TCGS	P18 098 18 2465 3	2.8230	1.5232	0.2285	1.4880	0.6593	1408	32	1326	36	1360	23	1320	38	3696165	692975
TCGS	P18 098 18 2465 4	3.0250	1.5702	0.2454	1.4670	0.4810	1412	34	1414	37	1413	23	1414	41	3696165	692975
TCGS	P18 098 18 2465 72	3.0710	1.7909	0.2424	1.5264	0.8489	1443	37	1398	38	1417	24	1395	42	3696165	692975
TCGS	P18 098 18 2465 11	3.2710	1.5286	0.2531	1.5409	0.6170	1500	35	1453	40	1471	25	1449	44	3696165	692975
TCGS	P18 098 18 2465 38	3.6210	1.6570	0.2781	1.6900	0.8043	1508	33	1587	45	1554	26	1589	53	3696165	692975
TCGS	P18 098 18 2465 10	4.1200	2.0631	0.3106	2.0927	0.8137	1544	45	1738	61	1648	33	1768	74	3696165	692975
TCGS	P18 098 18 2465 26	3.6100	1.8006	0.2657	1.8818	0.3588	1582	44	1515	54	1553	29	1510	56	3696165	692975
TCGS	P18 098 18 2465 16	3.8910	1.6705	0.2780	1.6187	0.7592	1643	34	1583	44	1609	27	1574	50	3696165	692975
TCGS	P18 098 18 2465 67	4.1560	1.6843	0.2967	1.6009	0.7476	1651	32	1673	47	1663	28	1677	53	3696165	692975
TCGS	P18 098 18 2465 20	4.2440	1.6494	0.3011	1.5111	0.5001	1662	37	1695	45	1680	27	1701	51	3696165	692975
TCGS	P18 098 18 2465 58	4.3970	1.7057	0.3116	1.7651	0.8855	1667	30	1750	55	1712	30	1759	62	3696165	692975
TCGS	P18 098 18 2465 25	4.3150	1.6222	0.3036	1.6469	0.6850	1669	36	1706	50	1692	27	1713	56	3696165	692975
TCGS	P18 098 18 2465 52	4.3900	2.1640	0.3051	1.8027	0.7977	1671	47	1714	56	1708	34	1721	62	3696165	692975
TCGS	P18 098 18 2465 36	4.1880	1.6714	0.2975	1.6807	0.6986	1673	42	1676	50	1675	29	1678	56	3696165	692975
TCGS	P18 098 18 2465 39	4.2030	1.6655	0.2945	1.5789	0.6313	1675	35	1662	46	1673	26	1661	52	3696165	692975
TCGS	P18 098 18 2465 9	4.1940	1.6691	0.2952	1.6430	0.6660	1675	36	1665	48	1668	28	1665	54	3696165	692975
TCGS	P18 098 18 2465 75	4.2820	1.6348	0.3019	1.5568	0.6609	1676	35	1702	45	1688	27	1704	53	3696165	692975
TCGS	P18 098 18 2465 78	4.3830	1.4830	0.3061	1.4538	0.6402	1678	29	1720	44	1709	25	1726	50	3696165	692975
TCGS	P18 098 18 2465 69	4.1960	1.6683	0.2949	1.5259	0.5360	1679	38	1665	45	1672	28	1664	51	3696165	692975

TCGS	P18 098 18 2465 37	4.7600	1.9958	0.3340	2.0958	0.8427	1683	40	1851	68	1773	34	1884	80	3696165	692975
TCGS	P18 098 18 2465 77	4.3410	1.6125	0.3042	1.6437	0.7595	1683	33	1709	50	1697	28	1715	56	3696165	692975
TCGS	P18 098 18 2465 34	4.5900	1.7429	0.3212	1.7123	0.7110	1684	37	1792	53	1741	30	1812	63	3696165	692975
TCGS	P18 098 18 2465 47	4.2440	1.6494	0.2958	1.5889	0.5892	1685	39	1669	46	1678	28	1667	53	3696165	692975
TCGS	P18 098 18 2465 73	4.2460	1.5309	0.2960	1.5541	0.6555	1692	33	1670	46	1680	26	1668	52	3696165	692975
TCGS	P18 098 18 2465 54	4.0000	1.8750	0.2759	1.6673	0.6649	1695	39	1568	46	1628	32	1556	51	3696165	692975
TCGS	P18 098 18 2465 46	4.3660	1.6033	0.3029	1.6342	0.8801	1702	33	1703	49	1704	26	1705	56	3696165	692975
TCGS	P18 098 18 2465 48	4.4090	1.5877	0.3060	1.5686	0.7223	1705	33	1719	47	1712	26	1722	54	3696165	692975
TCGS	P18 098 18 2465 53	4.3800	1.9406	0.3051	1.8027	0.5948	1707	50	1714	53	1706	31	1717	62	3696165	692975
TCGS	P18 098 18 2465 18	4.4030	1.5898	0.3037	1.5311	0.8075	1710	30	1711	47	1711	26	1710	52	3696165	692975
TCGS	P18 098 18 2465 40	4.4680	1.7905	0.3094	1.7776	0.7374	1712	35	1734	53	1722	29	1740	62	3696165	692975
TCGS	P18 098 18 2465 41	4.5700	1.7505	0.3140	1.9108	0.7846	1725	43	1756	58	1738	30	1764	68	3696165	692975
TCGS	P18 098 18 2465 29	4.6000	5.4348	0.3130	4.7923	0.9826	1728	75	1740	130	1697	47	1756	169	3696165	692975
TCGS	P18 098 18 2465 45	4.3300	2.5404	0.2920	2.2260	0.7848	1733	54	1643	67	1681	44	1639	72	3696165	692975
TCGS	P18 098 18 2465 24	3.9380	1.7776	0.2679	1.8104	0.6002	1736	44	1528	49	1620	29	1506	54	3696165	692975
TCGS	P18 098 18 2465 30	4.2020	1.6659	0.2855	1.9264	0.6398	1756	53	1615	55	1670	28	1603	61	3696165	692975
TCGS	P18 098 18 2465 23	4.0210	1.8652	0.2645	1.6257	0.4689	1790	46	1512	44	1634	29	1481	47	3696165	692975
TCGS	P18 098 18 2465 21	4.6900	2.3454	0.2945	1.8676	0.2129	1858	72	1662	56	1768	43	1635	61	3696165	692975
TCGS	P18 098 18 2465 2	28.8000	6.0764	0.2780	5.9353	0.9776	4798	49	1520	160	3180	160	250	57	3696165	692975
TCGS	P18 098 18 2465 44	24.0000	8.3333	0.2110	8.0569	0.9856	4844	65	1220	190	2620	240	141	50	3696165	692975

APPENDIX B – Concordia diagrams

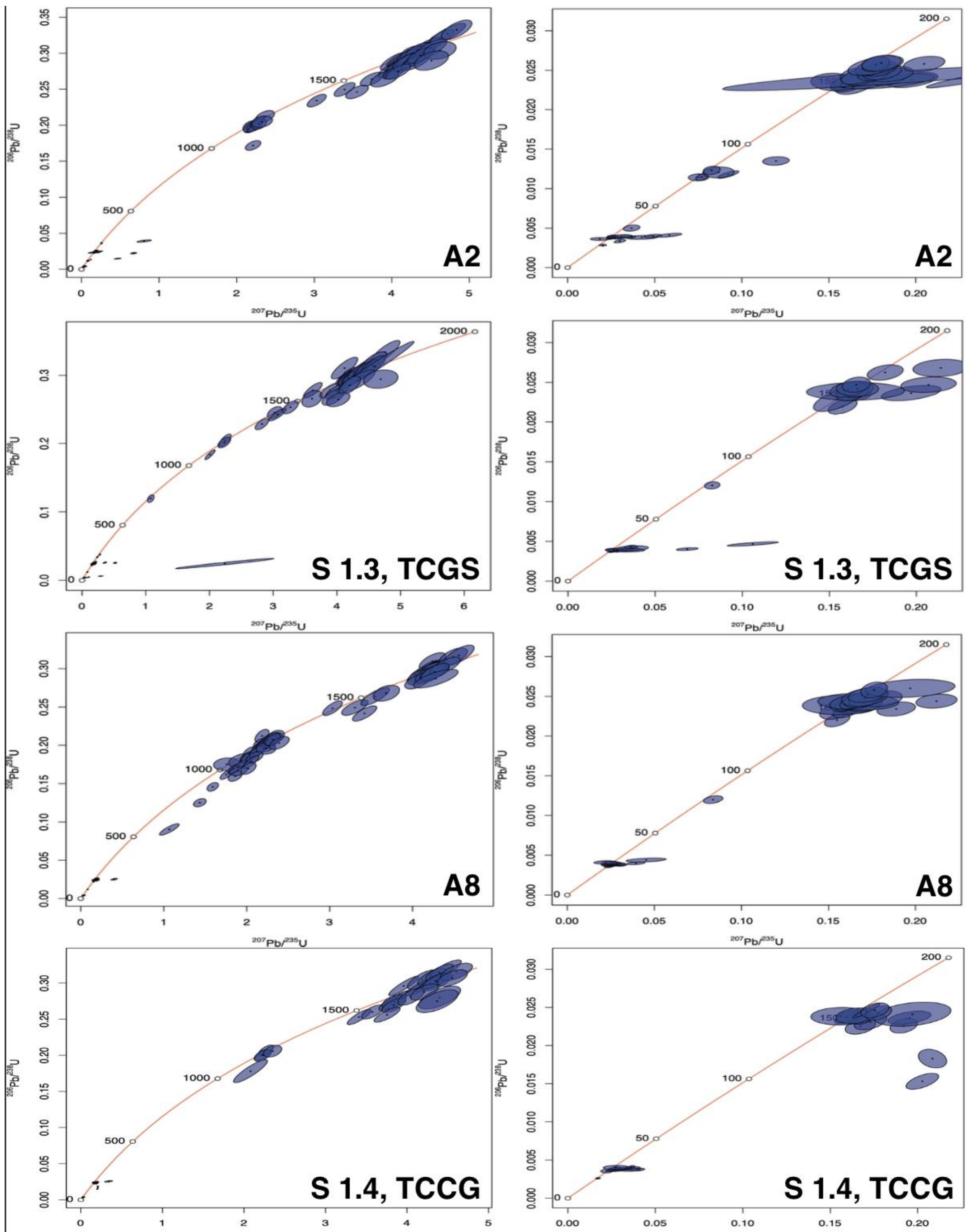

Figure B-1: Concordia diagrams of the four Soledad Rojo formation detrital zircon samples. The graphs in the left column show the age distribution from 0-2000 Ma, with the graphs in the right column showing the same data from 0-200 Ma to highlight the Mesozoic-Cenozoic age points. Adapted from (Chemostrat Ltd Lab, 2018).